DIRECT SHEAR STRESS MEASUREMENT DEVICE FOR USE IN ATMOSPHERIC BOUNDARY LAYERS

by

David Frei

A thesis submitted to the faculty of
The University of Utah
in partial fulfillment of the requirements for the degree of

Master of Science

Department of Mechanical Engineering

The University of Utah

August 2012

The University of Utah Graduate School

STATEMENT OF THESIS APPROVAL

The thesis of **David Frei**

has been approved by the following supervisory committee members:

Meredith Metzger	, Chair	6/14/2012 Date Approved
Eric Pardyjak	, Member	 Date Approved
Robert Stoll	, Member	6/14/2012 Date Approved

and by Timothy Ameel , Chair of

the Department of Mechanical Engineering

and by Charles A. Wight, Dean of The Graduate School.

ABSTRACT

Surface shear stress is an important quantity that characterizes the nature of a turbulent boundary layer. The problem of directly measuring the amount of shear stress acting on a surface has been previously studied. This thesis focuses on the design and fabrication of a 127 mm diameter floating disk plate. The small design affords many advantages including ease of implementation, reduced cost, portability, a higher expected frequency response, and the ability to deploy large arrays of these units to achieve spatial distribution and capture heterogenous effects. The shear stress sensor consists of a circular disk, with three springs attached to a housing each at 120^o apart. The disk is floating on a pool of liquid that provides damping. A vertical cavity surface emitting laser (VCSEL) is placed at the center of the disk and shines onto the surface of a 2-D position sensitive detector (PSD) that measures the (x, y) position of the disk centroid. With the use of several models, that were developed to obtain key parameters, the known disk centroid position is converted to force using the system transfer function. A physical prototype was built using the obtained parameters, and the fabrication and assembly are discussed, along with the static calibration results. These results correlate very well with the mathematical design to within 1.5% of the average value.

CONTENTS

LIST OF TABLES

LIST OF FIGURES

NOMENCLATURE

A	surface area of the disk in contact with the liquid m^2
θ	angle of the displacement vector measured from the horizontal deg
t	time s
ω_n	natural frequency in rad s^{-1}
r_0	magnitude of displacement vector m
k_{eff}	effective spring constant along displacement vector N/m
k	individual spring constant N/m
τ_w	wall shear stress N/m^2
μ	absolute viscosity of liquid Nsm^{-2}
ν	kinematic viscosity of liquid m^2/s
u	velocity profile function whithin liquid level
y	vertical distance within liquid level m
h	height of liquid level m
ω	frequency of forcing in rad s^{-1}
α	Womersley number in terms of y, $\alpha = \sqrt{\omega/2\,\nu}\,y$
β	Womersley number in terms of h, $\beta = \sqrt{\omega/2\,\nu}\,h$
U	magnitude of velocity of disk m/s
ϕ	phase shift of disk velocity in rad
c	damping coefficient of the disk kg/s
m	total mass of the disk kg
f_0	amplitude of forcing function N
ζ	damping factor of the disk

ACKNOWLEDGEMENTS

A special thanks to Prof. Metzger for being my advisor for this project and providing me with the confidence necessary to complete this daunting task. Also, thanks to my wife Sharon and my children for their patience and support as I worked on this project.

CHAPTER 1

INTRODUCTION

1.1 Background

Surface shear stress is an important quantity that characterizes the nature of a turbulent boundary layer. This quantity is especially important in large-eddy simulations (LES) where an instantaneous measurement of the wall shear stress is needed to specify the boundary condition near a surface. For high Reynolds number boundary layers, a near-wall model is required (Piomelli & Balaras, 2002). Marusic *et al.* (2001) performed wind tunnel tests of several tests of near-wall models using a series of hot wires, which were mounted above hot-film wall shear stress probes. The main limitation of the study was the uncertanty in extrapolating the results to higher Reynolds number flow, such as that found in the atmosphere. The present thesis describes the characteristics of a compact and relatively inexpensive shear stress sensor designed specifically for atmospheric flows.

There are two main methods for obtaining the value of shear stress on a surface as categorized by Haritonidis (1989). The first is by using an indirect approach, while the second is by direct measurement. The indirect methods use devices that are placed in close proximity to the surface, and infer the shear stress through a velocity measurement. A correlation typically based on the law of the wall, allows one to estimate the actual shear stress present on the surface.

The law of the wall as described by Kundu and Cohen (2008) assumes the velocity near the wall is given by the functional relationship,

$$U = f(\rho, \tau_w, \nu, y), \tag{1.1}$$

where U is the velocity, ρ is the fluid density, τ_w is the wall shear stress, ν is the kinematic viscosity and y is the normal distance from the wall. For a Newtonian fluid, the wall shear stress may be expressed as

$$\tau_w = \mu \left. \frac{du}{dy} \right|_{y=0}, \tag{1.2}$$

where μ is the dynamic viscosity. A characteristic velocity scale may be derived from τ_w and ρ as

$$u^\star = \sqrt{\frac{\tau_w}{\rho}}, \tag{1.3}$$

where $u^\star$ denotes the friction velocity and has units of m/s. Friction velocity can be used in (1.1) to replace ρ and τ_w, giving $\frac{U}{u^\star} = f(\frac{yu^\star}{\nu})$, or in conventional notation,

$$U^+ = f(y^+) \quad . \tag{1.4}$$

Expanding (1.4) in a Taylor series about $y^+ = 0$ yields

$$U^+ = U^+(y^+ = 0) \; + \; \left. \frac{dU^+}{dy^+} \right|_{y^+=0} \Delta y^+ \; + \; O(\Delta y^+)^2 \quad . \tag{1.5}$$

Since $U^+(y^+ = 0) = 0$ due to the no-slip condition at the wall, $dU^+/dy^+|_{y^+=0} = 1$ by definition, and $\Delta y^+ = y^+$ near the wall, (1.5) becomes

$$U^+ = y^+ \quad . \tag{1.6}$$

The above equation is a statement of the law of the wall and is generally accepted as valid in the viscous sublayer for $y^+ < 5$ (Hinze, 1975). The law of the wall may be rewritten as

$$\tau_w = \mu \frac{U}{y} \quad , \tag{1.7}$$

which may be used to estimate the wall shear stress given an accurate measurement of the mean velocity, U, at a distance y slightly above the wall in the viscous sublayer.

Other indirect methods utilize obstacles and heat transfer to infer the wall shear stress. Nitsche *et al.* (1984) performed a survey of several indirect methods. The

study was performed as it applied to the measurement of skin friction around an airfoil.

Some of the most widely used indirect techniques are those which place intrusions in the path of the flow, such as the use of sublayer fences and preston tubes. Sublayer fences rely on wall similarity in the viscous region of the boundary layer. In contrast, the preston tube is much larger in size and therefore captures the entire inner region of the boundary layer. Both methods use pressure differences to estimate wall parameters.

Heat transfer methods, such as fixed hot wires and surface hot film, measure turbulent fluctuations within the boundary layer. Nitsche *et al.* (1984) describes the difficulty in using the surface hot film technique due to the unsteady temperature conditions during flight tests. Fixed hot wire probes are often used, because of their small size and ability to measure velocities much closer to the wall than other methods. Even though the devices used to measure the velocity profile are small, they still cause disturbances in the flow.

More recently, Fernholz *et al.* (1996) and Ruede *et al.* (2002) explored the use of some newer heat transfer techniques, which include the use of micro-machined devices. These devices rely on wall similarity.

Another indirect technique used to estimate the wall shear stress is the measurement of the velocity profile. The measurement of velocity profiles are commonly used to determine the skin friction as developed and used in conjunction with the clauser chart (Clauser, 1954). Different methods may be used to obtain the velocity profile, such as those previously mentioned.

Although indirect methods are suited for some applications, they require an analytical or empirical correlation and often involve sensors that disturb the flow. Direct methods are more advantageous as no correlation is needed to obtain the value of the shear stress at the wall. Direct methods involve removing an actual section of the wall and inserting a flush-mounted sensor that displaces slightly in response to the shear stress on the active surface of the sensor. The principle of operation is

shown in Figure 1.1. These types of devices are typically referred to as drag plates or drag moment balances.

The drag momemt balance comes in two basic types, nulling and non-nulling. The nulling types of balances return to their equilibrium positions after being displaced. The non-nulling types free-float while in operation. An example of a non-nulling parellel beam drag moment balance along with a nulling type of spring restoration force balance is illustated in Figure 1.2. Typically, the drag moment balance consists of a floating head/plate connected to a transducer that produces an output signal proportional to either the applied force or the displacement of the head, depending on the type of transducer used. One of the most popular types of transducer systems is the linear variable differential transformer (LVDT). The LVDT consists of an iron core armature housed within a transformer. This allows for easy nulling of the drag moment balance. Feedback may also be incorporated into the design to allow the device to self null. A parellel linkage drag moment balance of this type was developed by Morsy (1974). Also, the LVDT has been used in non-nulling systems such as the one by Pradeep and Sullery (2003).

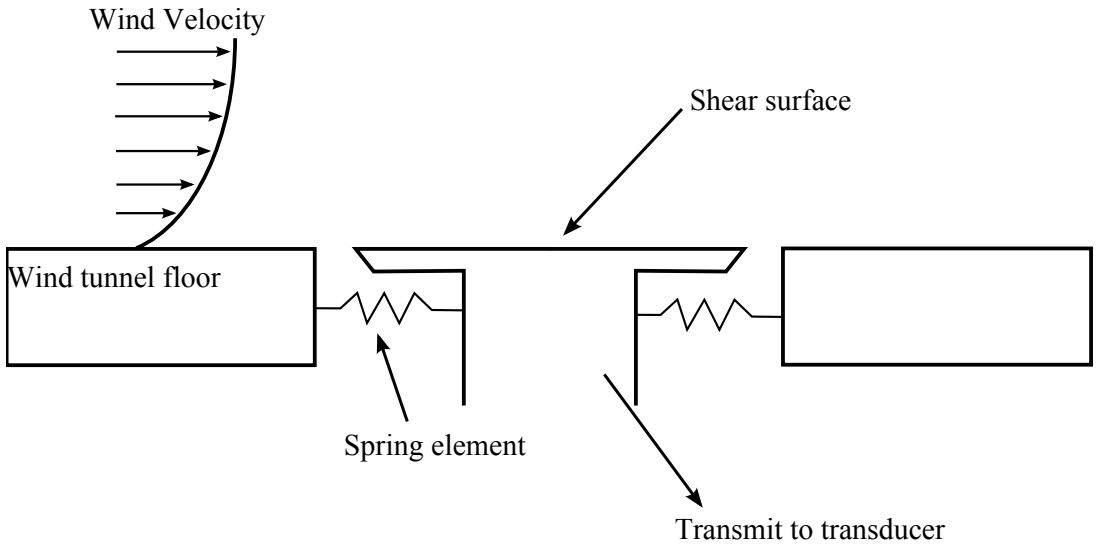

Figure 1.1. Diagram of the principle of operation for most types of direct measurement devices.

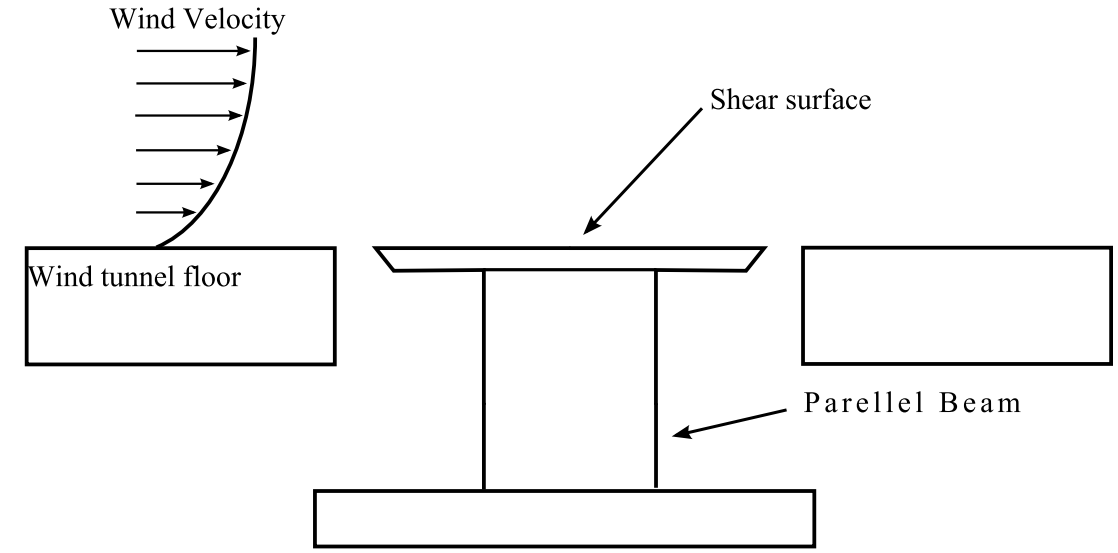

Non-nulling parellel beam type

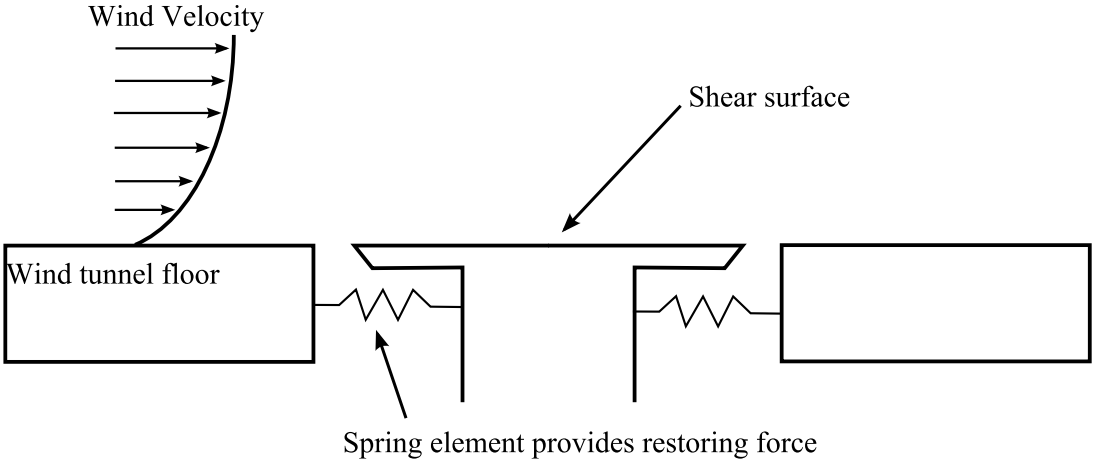

Nulling spring restoration force type

Figure 1.2. Example comparison of a non-nulling and a nulling type of drag moment balance. A parellel beam system along with a spring restoration force system are depicted here.

Many nulling types of direct measurement devices are based on a design by Paros (1970) in conjunction with the Kistler Corporation. The developed sensor consists of a permanent magnet floating head, with a series of capacitance plates in conjuntion with an outer coil, which allows the system to return to the null position. This is accomplished through the use of a servo feedback system, which returns an electrical signal sensed by the capacitance plates. Some researchers also combine different techniques in their individual design approaches. Winter (1977) and Magill (1999) give a more complete listing of different direct measurement techniques.

An example of a direct shear stress measurement device is the one developed by Bradley (1968), where a study was made to evaluate the effects of surface roughness on a tarmac surface. This was accomplished by using a metal spike grid to artificially simulate different surface roughness conditions. The drag plate was suspended by four piano wires and strain gauges were used to measure the head displacement. This same type of drag plate device was used by Haugen *et al.* (1971) in a study of Reynolds stress and heat flux. This study was performed in a wheat field in Kansas, where the wheat stubble was approximately 18 cm high. Precautions were taken to preserve the surroundings during installation and the disk itself was covered with the same wheat stubble as the field.

One simple method of direct skin friction measurement is that of placing a floating head on beam support elements, which act as a restoring force. This type of system is non-nulling. The use of strain guages attached to the beam elements provide the displacement measurement. To increase the sensitivity of this type of drag balance, very long and thin beams are required. This creates an unstable and delicate system. Smith (2001) used silicon based strain guages instead of foil based, because of their increased sensitivity for his studies in scramjet skin friction measurements. Heuer and Marusic (2005) used a parellel beam setup, which supported a floating head. The measurement was taken by reflecting a laser light off a spherical mirror, which was placed at the center of the head. The light position was then measured using

a 2-D duo-lateral position sensitive detecter. This balance was used to measure the skin friction in the atmospheric boundary layer.

Several disadvantages of direct measurement techniques are worth noting. Haritonidis (1989) outlines 12 disadvantages of direct measurement devices. Some of these include: a comprimise between size and sensitivity, the effects of gaps surrounding the plate, the effects of misalignment of the sensing element with the wall, poor frequency response due to size, and the general delicate nature of the devices. Allen (1977) performed work on quantifying the error of direct measurement due to misalignment of the sensor head with the surface. The results indicate that a slight protrusion of the sensor plate above the surface produced similar error as a sensor plate slightly below the surface. These results have been crucial in the design of accurate direct measurement devices.

The main motivation for the current study is to improve on the previous design of Sadr and Klewicki (2000) based on a floating-element device that provided direct measurement of the surface shear stress in atmospheric flow over a salt playa. The problem with the device of Sadr and Klewicki, shown in Figure 1.3, is the size. The diamaeter of the floating plate measured 2.4 m, and the support housing comprised of welded aluminum weighed about 150 kg. This posed severe challenges in terms of deployment during a field campaign as well as transportation and storage when not in use. The reason behind the large design was twofold. First, the expected the expected shear stress in the atmospheric surface layer is very small, $\tau_w \cong 3\text{x}10^{-3} Pa$ (Klewicki *et al.*, 1995). Secondly, Sadr and Klewicki chose to use a floating disk connected to force transducers. This forced them to use a large surface area to resolve the small shear stresses.

This project focuses on reducing the size of the floating disk plate design by Sadr and Klewicki, while still maintaining accurate results. This is achieved by using optical components to measure the displacement of the floating disk, rather than force transducers to measure the applied wind shear stress acting on the top surface of the plate.The smaller design affords many advantages including ease of

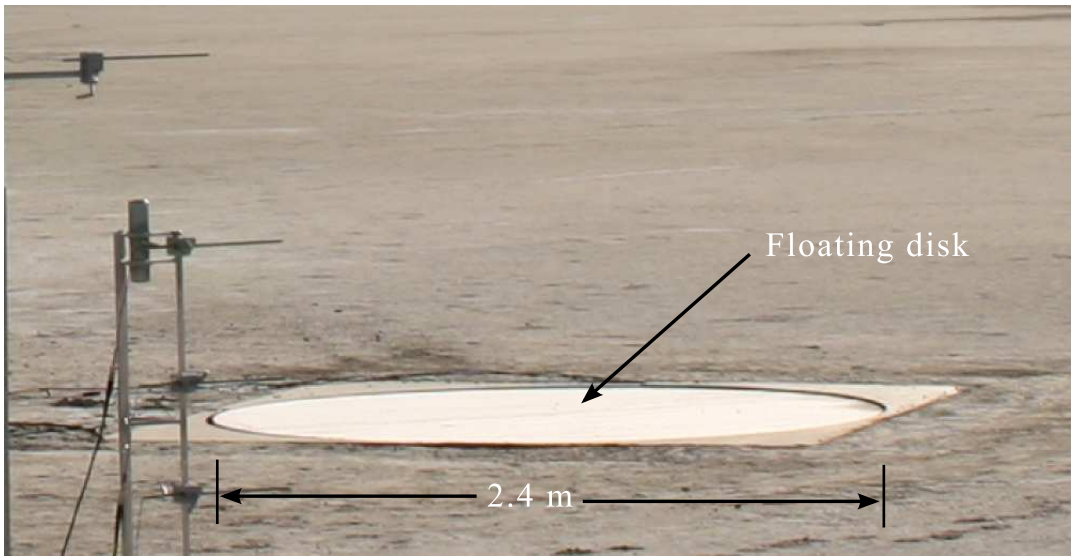

Figure 1.3. Floating plate as installed in Utah's western desert.

implementation, reduced cost, portability, a higher expected frequency response, and the ability to deploy large arrays of these units to achieve spatial distribution and capture heterogenous effects.

1.2 Target Design

The purpose of this design is to accurately measure surface shear stress in the atmospheric boundary layer over the salt playa of Utah's western desert. This measurement includes both magnitude and direction. The most important specification is the full-scale range of the device. Based on the analysis of Metzger (2002), the typical range of shear stresses observed over the salt playa of Utah's western desert is $0.006-0.063$ Pa. Two other important design specifications include the frequency response of the device and the spatial resolution. The response needs to be as large as possible to detect small temporal fluctuations in the shear stress as well as small enough in size to avoid spatially averaging over a significant range of scales of turbulent eddies. Hot-wired sonic anemometry data of Metzger (2006) suggest that a frequency response of 55 Hz will be adequate to resolve the entire inertial

subrange of the near-surface streamwise velocity in the atmospheric boundary layer. These data also suggest that a floating disk with a diameter of 1-1.5 cm would be able to capture individual coherent motions, such as "pockets" and low-speed streaks as visualized by Klewicki *et al.* (1995). However, the length scale associated with a frequency of 55 Hz (assuming a mean wind speed of 5 m/s) is about 9 cm. This length represents the largest eddy expected in the inertial subrange. Therefore, based on this information, the target design specifications for the present wall shear stress sensor are listed in Table 1.1.

1.3 Design Methodology

To avoid potential pitfalls of indirect approaches, most notably using correlations that may not be applicable in atmospheric flows where thermal stability effects could have a strong influence on the surface shear stress, the present design utilizes a direct approach. The principle of operation of the present device is illustrated in Figure 1.4. The device consists of a circular disk of diameter D that floats on a liquid layer of height h, which constrains the motion in the vertical direction and provides viscous damping. Extension springs, with a spring constant equal to k, are attached between the disk and the device housing, and provide the restoring force. Additional important design parameters are the gap spacing, G, between the periphery of the disk and the edge of the housing, as well as the vertical protrusion height, Z, between the top of the disk and the top of the housing. As the air flows over the disk, the applied shear stress causes a displacement. By measuring this displacement, the force in the springs can be determined; from this, the shear stress is calculated.

Table 1.1. Target design specifications

Parameter	Value	Unit
τ_w (expected shear stress range)	0.006−0.063	Pa
f (frequency response)	55	Hz
D (optimal disk diameter)	1−1.5	cm

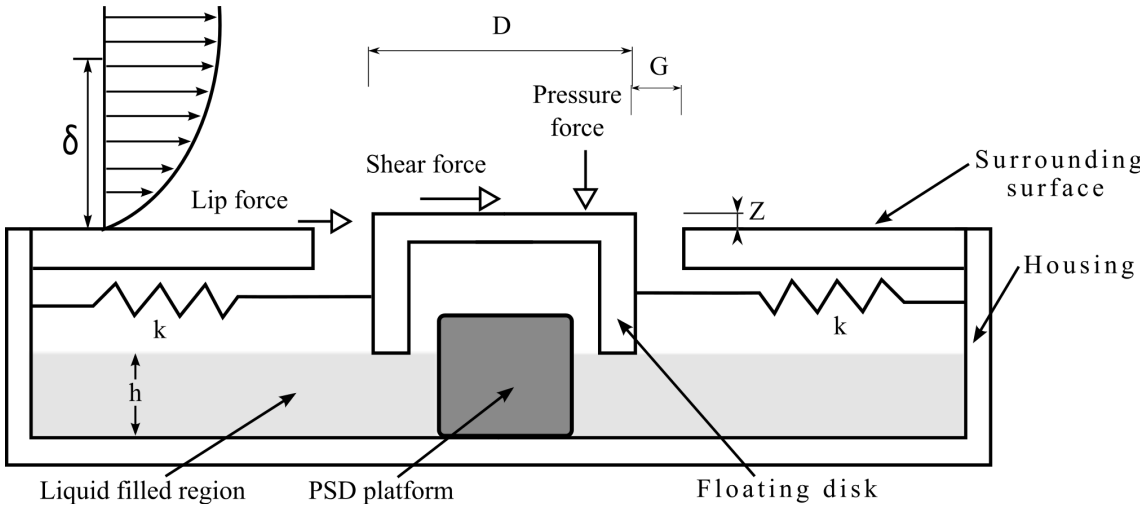

Figure 1.4. Diagram of basic principle of operation of the present design. Not to scale.

The difficulty in this principle lies in obtaining an accurate measure of the displacement of the springs. Several methods could be used to accomplish this task. These include force transducers, load cells, strain guages, among others. One option is a linear variable differential transformer (LVDT). Another option is a position sensitive detector (PSD). The latter was chosen for the present design. The reason behind this decision was threefold. First, the PSD is less expensive than other options. Second, the PSD can be used with a spherical mirror to achieve an optical advantage that decreases the uncertainty. Third, this approach has been used previosly by Heuer and Marusic (2005). For this application, a 2-D PSD is needed. This is due to the fact that the floating disk is allowed to move in plane, so an x and y displacement component are required to fully define the position of the disk centroid.

The PSD outputs a voltage signal proportional to the position of a light beam relative to the center of the active area of the detector. When the centroid of the light beam coincides with the center of the active area, zero voltage is produced. As the light beam moves off-center, x and y voltage signals are generated that can be converted into an actual position using a conversion factor supplied by the

manufacturer. Figure 1.5 shows several types of 2-D PSDs, which come in different sizes and mount layups to suit individual needs. In the present design, the light beam that impinges on the PSD is generated using a vertical cavity surface emitting laser (VCSEL), with an output wavelength of 850 nm and a divergence angle of 6 degrees.

The total displacement of the floating disk at full-scale is determined by the allowable gap size between the floating element and the housing. Allen (1977) investigated the effect of gap size G and protrusion height Z on the output of a generic drag moment balance. The forces acting on the drag balance include the shear force on the top surface, the lip force acting on the side walls and the pressure force acting on the top surface, as illustrated in Figure 1.4. The shear force created by the fluid flow over the surface is the force of interest. The ability of the drag moment balance to accurately measure the shear force may be adversely affected by misalignment. If the top surface of the drag moment balance is not completely flush with the surroundings, then a lip force caused by the fluid impinging on the sidewalls will be induced. This force acts in the horizontal plane producing either an additive or subtractive component to the total tangential force acting on the disk. Finally, pressure differences on the floating head produce a net pressure force that acts normal to the plane of shear stress.

Allen shows that the total error produced by a negative protrusion (Z<0) is about the same as that for a positive protrusion (Z>0). Larger gap to diameter ratios,

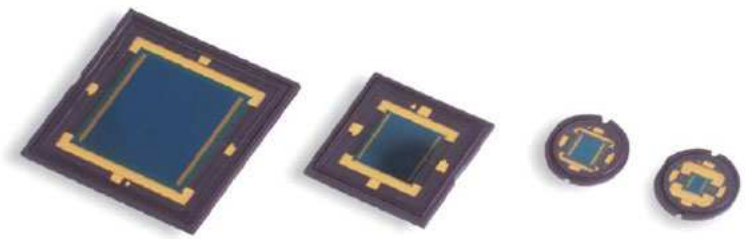

Figure 1.5. Examples of 2-D position sensitive detectors (PSD) with two types of casings, square and round. Various sizes of active areas are displayed, ranging from $4-20$ mm^2.

G/D, cause the drag balance to be less sensitive to Z. This applies to both the total tangential force and lip force. Overall, the work performed by Allen (1977) indicates that an increased gap size reduces the sensitivity to misalignment error.

Based on these findings, a gap size was chosen to match the size of sensing area of the PSD. The PSD that was chosen for this application was a 2-D duo-lateral sensor with a 4 mm x 4 mm active area. This was the smallest 2-D PSD available. Therefore, the maximum deflection of the floating disk at full scale is ± 1.5 mm. Note, only the central 75% of the active area of the PSD is linear; so, beam displacement is restricted to less than the full 4 mm. To allow displacements within ± 1.5 mm, the gap size must be chosen as $G = 1.5$ mm. Based on the results by Allen (1977), and assuming $|Z/\delta| \leq 0.001$, which should be easily achieved in the atmosphere, the best range for G/D giving negligible error in the measured tangential force is $0.004 \leq G/D \leq 0.008$. For the case $G/D = 0.008$, the requirement of G =1.5 mm yields a disk diameter of D = 18.75 cm (7.4 in). To reduce manufacturing costs, which was a consideration in the project, and to slightly improve spatial resolution and frequency response, a decision was made to restrict the diameter of the floating disk to D = 12.7 cm (5 in). This results in G/D = 0.011 for the present design. Referring again to the work by Allen (1977), one finds that for $|Z/\delta| \leq 0.001$ and G/D = 0.01, a $2-4\%$ error can be expected in the measured tangential force.

1.4 Uncertainty

The reason to maximize the active area of the PSD is based heavily on the error associated with the displacement measurement. Accuracy is one of the main concerns with this design. The uncertainty of the shear stress measurement is directly proportional to the uncertainty of the PSD. The force in the springs is given by

$$F = \tau\, A = k_{eff}\, x \tag{1.8}$$

where F is the force acting on the disk, τ is the shear stress, A is the area of the disk, k_{eff} is the effective spring constant and x is the displacement of the disk. Solving

(1.8) for shear stress τ the following is obtained

$$\tau = \frac{k_{eff}\, x}{A}\,. \tag{1.9}$$

To find the uncertainty associated with the shear stress, the equation for uncertainty is applied and results in

$$\sigma_\tau = \frac{d\tau}{dx}\sigma_x = \frac{k_{eff}\,\sigma_x}{A} \tag{1.10}$$

where σ_τ is the uncertainty in the function for shear stress, and σ_x is the uncertainty in the position measurement x. To determine the uncertainty relationship between the shear stress and the position, (1.10) is divided by (1.9) which gives

$$\frac{\sigma_\tau}{\tau} = \frac{\sigma_x}{x} \tag{1.11}$$

solving (1.11) for τ yeilds the final form

$$\tau = x\,\frac{\sigma_\tau}{\sigma_x}\,, \tag{1.12}$$

which indicates that the uncertainty in the shear stress is directly proportional to the uncertainty in the position measurement. The chosen 2-D duolateral PSD for this project has a position nonlinearity of $\pm\,0.3\%$.

1.5 Outline of Thesis

The purpose of this project is to improve on the floating disk system originally designed by Sadr and Klewicki (2000), for measuring surface shear stress over the salt playa of Utah's western desert. The major improvement is the reduced size associated with the present design, in addition to an increase in spatial resolution and frequency response. The outline of this thesis is as follows. First, an optical advantage model is discussed, which uses geometric principles and ray tracing to determine the path of a light beam as it reflects from a spherical mirror. The implementation of a series of lenses is also discussed, along with physical limitations.

Next, the development of an overall vibration model for the disk is discussed. This model includes calculation of an effective spring constant for the system. The

model also includes the effect of a viscous damping by the liquid layer beneath the disk. Results of system behavior are then presented for a range of design parameters. Finally, construction of a physical prototype of the shear stress sensor is explained, along with some of the challenges that were overcome during fabrication and assembly.

CHAPTER 2

OPTICAL ADVANTAGE LENS MODEL

2.1 Two-Dimensional Model

The use of a spherical mirror on the bottom of the floating disk will allow for an optical advantage, such that small displacements of the disk result in large movements of the reflected beam on the PSD. From a design standpoint, small displacements are desired because limiting the range of motion of the disk reduces the gap size, G, needed. This allows for a smaller disk diameter, D, to be used (according to the criterion $0.002 \leq G/D \leq 0.008$ as discussed in section 1.3), which in turn increases the overall spatial resolution of the device. A properly designed optical system will have an appropriate gain factor that takes advantage of the full range of the PSD. The full range of the PSD, is specified by the manufacturer in terms of the active area of the chip. Dimensions vary according to type of PSD and model. The current design uses a 2-D PSD with an active area of 4 mm^2, which means that the light beam incident on the face of the PSD is constrained to move $\pm$ 2 mm from the equilbrium position. To evaluate the feasability of using an optical advantage in the present drag balance and to better understand the design constraints involved in the optical advantage system, a 2-D ray tracing model was developed. A schematic of the geometry is shown in Figure 2.1. The present model assumes the disk can only move in the x-direction and that the light beam has an infinitessimally small diameter.

The goal of this model is to determine the maximum achievable gain, g, as a function of the following input parameters: y_c, θ, r, L_c, L_d and L_s, where y_c is the vertical coordinate of the mirror centroid, θ is the angle of the light source with the horizontal, r is the radius of the mirror, L_c is the x-location of the mirror centroid

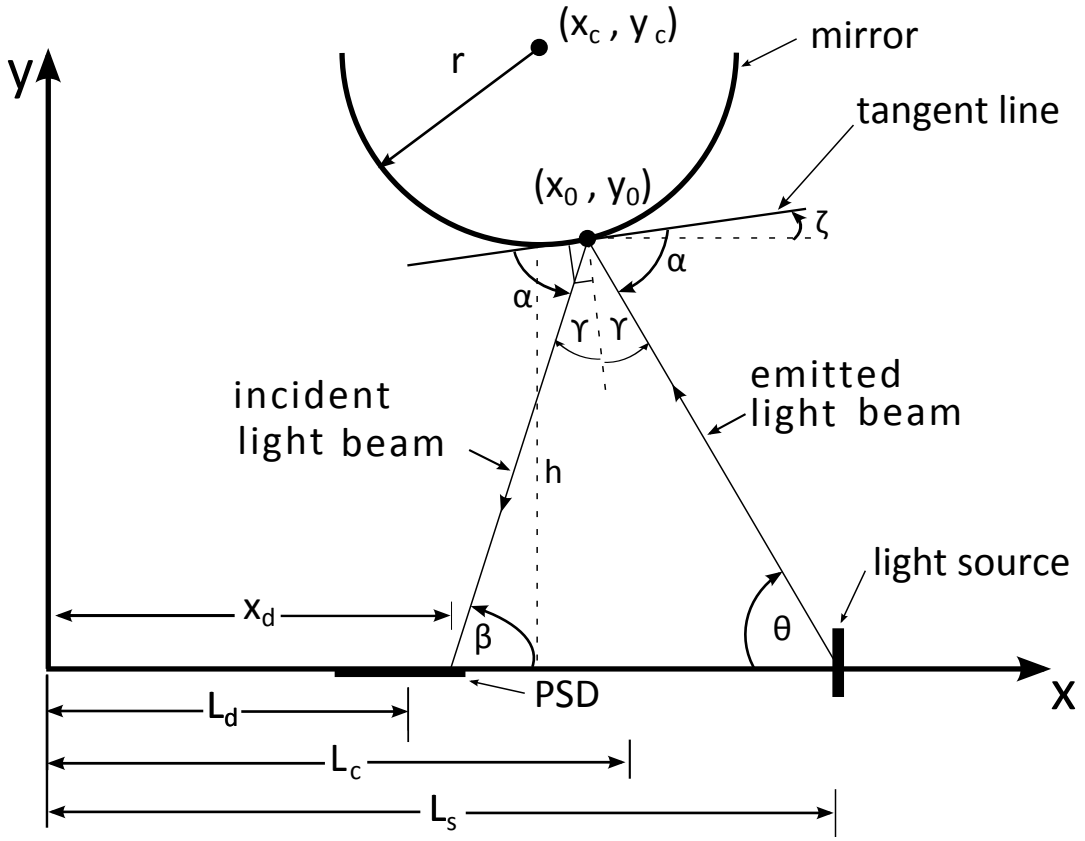

Figure 2.1. Diagram of the 2-D optical advantage model showing a ray of light emitted from the light source at $x = L_s$ that reflects off of the surface of a spherical mirror of radius r and impinges on the PSD, whose center lies at $x = L_d$.

while in equilibrium, L_d is the x-location of the center of the detector and L_s is the x-location of the light source.The optical gain, g, is defined as the ratio of the displacement of the light beam on the PSD over the actual displacement of the disk centroid,

$$g = \frac{|x_d - L_d|}{|x_c - L_c|} \ , \tag{2.1}$$

where x_d is the position of the incident light beam on the PSD, L_d is the position of the light beam on the PSD while the disk is in equilibrium, x_c is the position of the centroid of the disk, and L_c is the position of the centroid of the disk while in equilibrium. In practice, the disk centroid is constrained to move only a specified amount from its equilibrium position, as determined by the prescribed gap size. The

complete derivation of g based on geometric principles and ray tracing can be found in Appendix A; only the basic steps are outlined in this section.

The first step in the derivation is to determine the position of the light beam on the PSD in terms of the functional relationship $x_d = f(x_c, y_c, \theta, r, L_s, L_d, L_c)$. One can start by writing the equation of the line representing the incident light beam,

$$x_d = x_0 - y_0 / \tan\beta \ , \tag{2.2}$$

where (x_0, y_0) are the coordinates of the point at which the emitted light beam reflects off of the spherical mirror, and β is the angle between the incident light on the PSD and the x-axis. To find x_d, the point (x_0, y_0) is needed along with the angle β. The equations for x_0 and y_0 are respectively

$$x_0 = \frac{-(2\tan\theta(y_c - L_s\tan\theta) - 2x_c)}{2(1+\tan^2\theta)}$$

$$\pm \frac{\sqrt{(2\tan\theta(y_c - L_s\tan\theta) - 2x_c)^2 - 4(1+\tan^2\theta)(x_c^2 + (y_c - L_s\tan\theta)^2 - r^2)}}{2(1+\tan^2\theta)}, \tag{2.3}$$

and

$$y_0 = \frac{-(\frac{2(x_c - L_s)}{\tan\theta} - 2y_c) \pm \sqrt{(\frac{2(x_c - L_s)}{\tan\theta} - 2y_c)^2 - 4(1+\frac{1}{\tan^2\theta})(y_c^2 + (x_c - L_s)^2 - r^2)}}{2(1+\frac{1}{\tan^2\theta})}. \tag{2.4}$$

The expressions in (2.3) and (2.4) give x_0 and y_0 as a function of x_c with input parameters: L_s, θ, y_c, and r. To complete the analysis, an expression for β as a function of x_c is required. To find β, the law of reflection is used, which states that the angle, γ, between the incident ray and the normal to the reflective surface equals the angle that the reflected ray makes to the same normal. This law can be applied to flat or curved surfaces. The angle γ is measured from the tangent line at (x_0, y_0) on the surface of the mirror. From Appendix A, the equation for β is found to be

$$\beta = \theta + 2\arctan\left(\frac{2(x_0 - x_c)}{\sqrt{2(r^2 - (x_0 - x_c)^2)}}\right). \tag{2.5}$$

Using equations (2.1), (2.2), (2.3), (2.4), and (2.5), one can directly evaluate the optical gain as a function of disk displacement x_c for the following design parameters: L_d, L_s, L_c, θ, r and y_c.

If the origin of the coordinate system is moved to the centroid of the circular mirror, the number of design parameters can be reduced. In the new coordinate system $L_c = 0, L_s = d$, and $L_d = -d$, where d is the horizontal distance from the mirror centroid to the light source while in equilibrium. Aditionally, specifying h, which is the vertical distance between the light source and the spherical mirror while in equilibrium, sets the emitted angle

$$\theta = \arctan\left(\frac{h}{d}\right) . \tag{2.6}$$

The optical gain now becomes

$$g = \frac{|\tilde{x}_d|}{|x_c|} , \tag{2.7}$$

where $\tilde{x}_d = |x_d| - d$ and denotes the displacement of the light beam relative to the center of the PSD. Using this simplification the relevant design parameters are: h_c, r and θ, where $h_c = y_c$ the vertical height of the mirror center.

2.2 Results from Model

Results for the gain based on (2.7) are presented and discussed in this section. The basic approach was to allow only one design parameter to vary, while holding the other two constant, then horizontally increasing the distance of the mirror over the very small range ± 0.00635 mm, using only the maximum value. Figure 2.2 shows g versus h for the case of $r = 3$ mm and $\theta = 30°$. The values for r and θ are representative of one possible solution; they are used to obtain the basic trends of the optical gain. The trend indicates that the optical gain increases linearly as the distance between the PSD and mirror increases, with a proprtionality factor of 2.54.

Figure 2.3 shows g versus the radius of the spherical mirror for the case of $h_c = 6$ mm and $\theta = 30°$. The trend here indicates that as r decreases, the optical gain

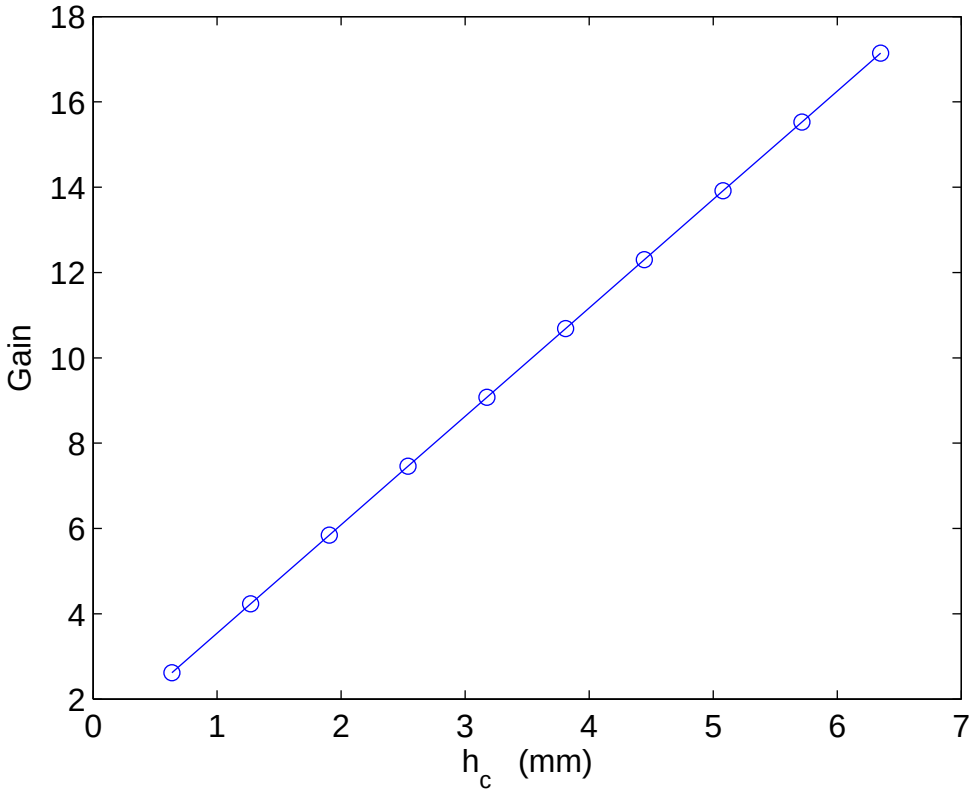

Figure 2.2. Optical gain versus the height from the light source to the center of the spherical mirror with mirror radius and incident light ray angle held constant, at $r = 3$ mm and $\theta = 30°$, respectively.

increases dramatically. For example, at $r = 2$ mm, $g = 26.34$; while, at $r = 1$ mm, $g = 52.4$.

Figure 2.4 shows g versus the angle of the light emitted from the source for the case of $r = 3$ mm and $h_c = 6$ mm. The trend indicates that as θ decreases (i.e. the emitted light approaches horizontal), the optical gain increases in a nonlinear fashion similar to that observed for r. For example, at $\theta = 40°$, $g = 10.74$; while, at $\theta = 10°$, $g = 137.54$.

When all of the three trends are combined, taking the values of the parameters that produce the highest calculated gain from each trend, a very high theoretical optical advantage can be achieved. An example of this can be found in Table 2.1, where an

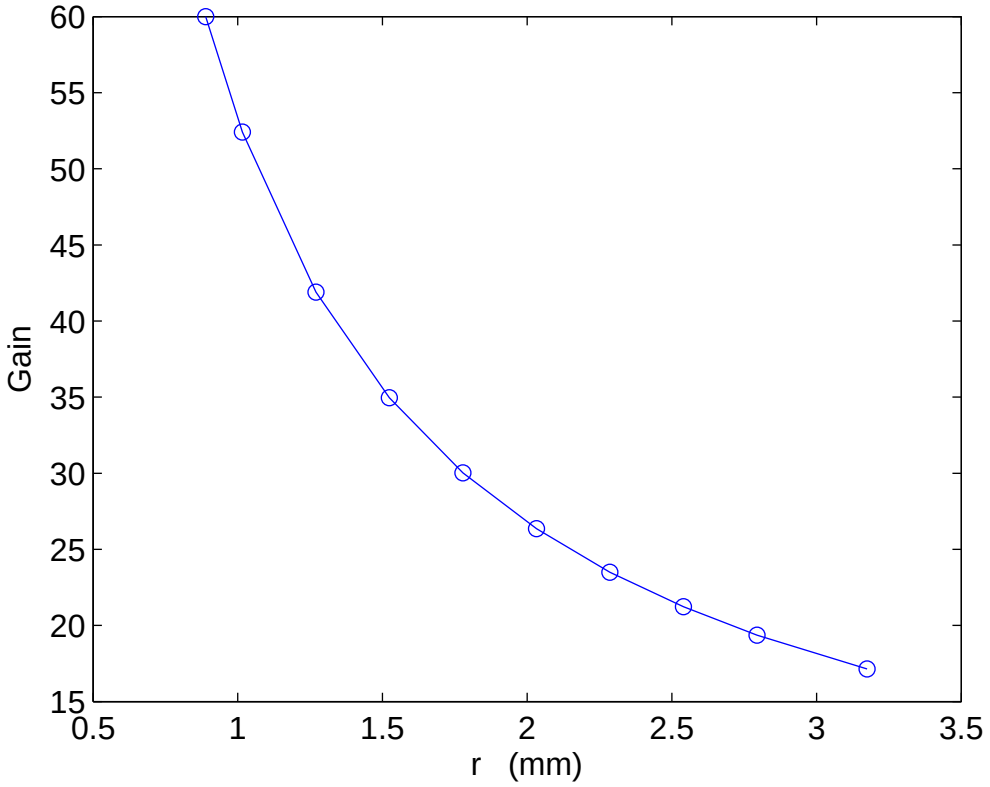

Figure 2.3. Optical gain versus radius of the mirror for the case with $h_c = 6$ mm and $\theta = 30°$.

optical gain of 250 was found using the specified parameters. This theoretical gain value could keep increasing, based on the trends.

2.3 Lens System

Once values for r, h_c, θ were selected based on the output of the model described in section 2.2, a benchtop set-up of the optical advantage system was built and tested. There were three main parts used for the initial experiment. First, the light source was a vertical cavity in pill laser (VCSEL) from OPTEK technology part # OPV322. Second, the spherical mirror was a 0.072 inch high precision ball bearing from Baltec part # 0479001307 S626 HH. Third, the PSD was from On-trak photonics part #2L4SP. The physical system did not produce the expected outcome. This was

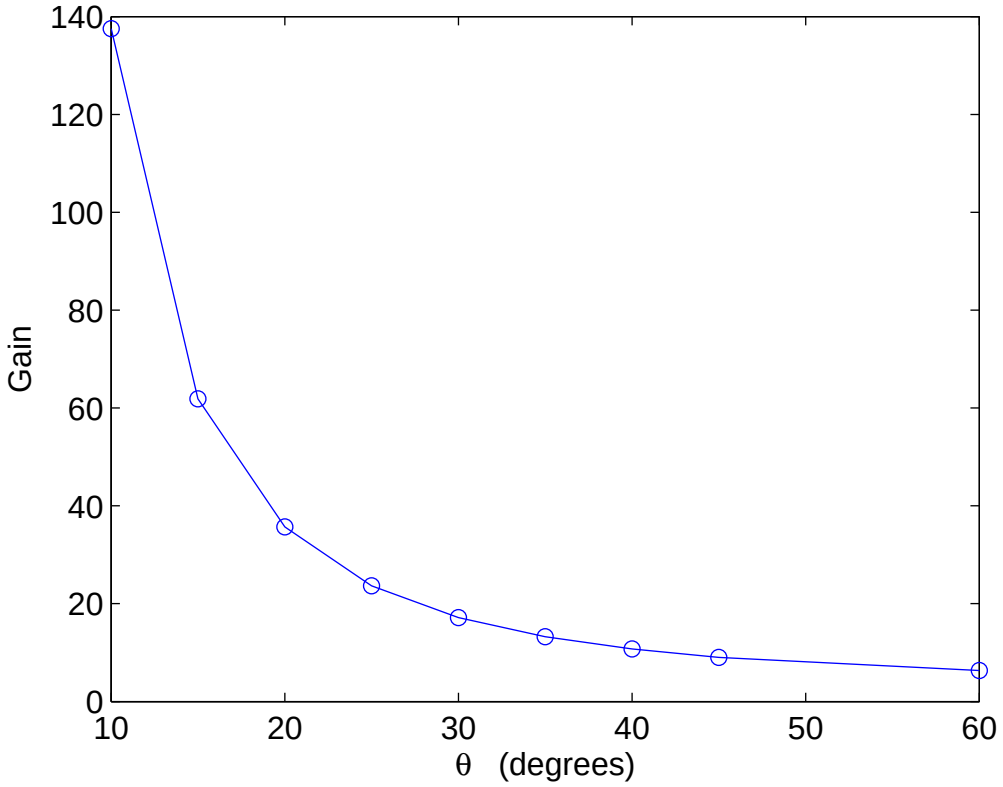

Figure 2.4. Optical gain versus angle of the incident light ray for the case with $r = 3$ mm and $h_c = 6$ mm.

attributed to the divergence angle of the vertical cavity surface emitting laser, which is specified as 6° by the manufacturer. Divergence by the laser light caused the final spot size of the incident light beam to be greater than the entire area of the PSD, which yielded no sensitivity to displacement. An optical scheme using lenses was considered to correct for the divergence of the emitted light beam, and reduce the diameter of the incident light beam on the PSD.

2.3.1 Optical Design Theory

A common practice in optics is to treat the light as different rays traveling through space, and then track these rays as it passes through a series of lenses. This method is called ray tracing (Hecht, 1987). The reason that light can be approximated by a

Table 2.1. Maximum theoretical optical gain

Parameter	Value	Unit
r (radius of mirror)	1	mm
h_c (center height)	7	mm
θ (angle of light source)	10	degrees
G_{max} (maximum optical gain)	250	-

ray is because it is traveling so fast (speed of light) that all transient effects occur within a very short distance. The wave nature of light is then neglected, and it is treated as a single line traveling through space (Modest, 2003).

To start the discussion on optical design, three types of lenses will be explained briefly, including aspherical, spherical, and gradient index (GRIN), each of these was considered as a possible means of correcting the beam divergence problem in the present design.

The first type of lens is called an aspherical lens, the shape of which is created by taking a point source of light and calculating the surface needed to perfectly mirror that point source within another medium. The benefit of using an aspherical lens is that it produces a high quality output beam, with very little stray light. However, since an aspherical lens has a unique curvature depending on the application, it is more difficult to manufacture, and hence expensive.

The second type of lens is called a spherical lens. These lenses are much easier to manufacture and thus less costly than the asherical type. The spherical lens considered for this project was a plano-convex lens, which means that one side is flat or planar while the other is convex. These lenses are used to either focus an incoming beam or to collimate a diverging beam.

The third type of lens to be considered is the gradient index (GRIN) lens. This lens has a unique property in that the lens material has a gradually changing index of refraction. When a ray passes through this lens, it continues to bend as it progresses through the medium. When chosen correctly, this type of lens can be used to collimate

or focus a diverging beam. It can also focus collimated light.

For this project, it is important to understand the characteristics of a spherical mirror, since it is being used for the optical advantage. The spherical mirror acts as a diverging lens. As the light reflects off the surface, it diverges, even if the incident beam is collimated. This can prove challenging when designing an optical scheme, since the reflected beam diameter needs to be small enough to achieve position sensitivity.

2.3.2 Governing Equations

Snells law is used to calculate the angle of a light ray within a medium, given the indices of refraction of the two media,

$$n_i \sin\theta_i = n_t \sin\theta_t \ , \tag{2.8}$$

where n_i is the index of refraction of the incoming ray, n_t is the index of refraction for the transmitted ray, θ_i is the angle of incidence for the incoming ray measured from the normal to the surface, and θ_t is the angle of the transmitted ray measured from the normal to that surface.

The thin lens equation, or sometimes referred to as the lens makers equation, relates the focal length of the lens to its radii, and is given by the following

$$\frac{1}{f} = (n_l - 1)\left(\frac{1}{R_1} - \frac{1}{R_2}\right) \ , \tag{2.9}$$

where f is the focal length, n_l is the index of refraction of the lens material, R_1 is the radius of the first side of the lens and R_2 is the radius of the second side of the lens.

The thick lens equation, which relates the focal length to the radii and thickness of the lens, is described by

$$\frac{1}{f} = (n_l - 1)\left[\frac{1}{R_1} - \frac{1}{R_2} + \frac{(n_l - 1)d}{n_l\, R_1\, R_2}\right] \ , \tag{2.10}$$

where all variables are the same as previously mentioned, with the exception of d, which is the thickness of the lens measured between the two lens vertices. Note, for

a thick lens all focal lenghts are measured from two principle planes. The location of these two principle planes are given as

$$h_1 = -\frac{f(n_l - 1)d}{R_2\, n_l} \tag{2.11}$$

and

$$h_2 = -\frac{f(n_l - 1)d}{R_1\, n_l} \tag{2.12}$$

where h_1 is the distance to the first principal plane measured from the vertex of radius 1, and h_2 is the distance to the second principle plane measured from the vertex of radius 2. Note, all focal lengths for a thick lens are measured from these principal planes. Figure 2.5 shows the basic parameters needed for the thick lens equation.

The spherical mirror equation, which gives the relation between radius and focal length, is given by

$$f = \frac{R}{2}\ , \tag{2.13}$$

where f is the focal length of the mirror, and R is the radius of the sphere.

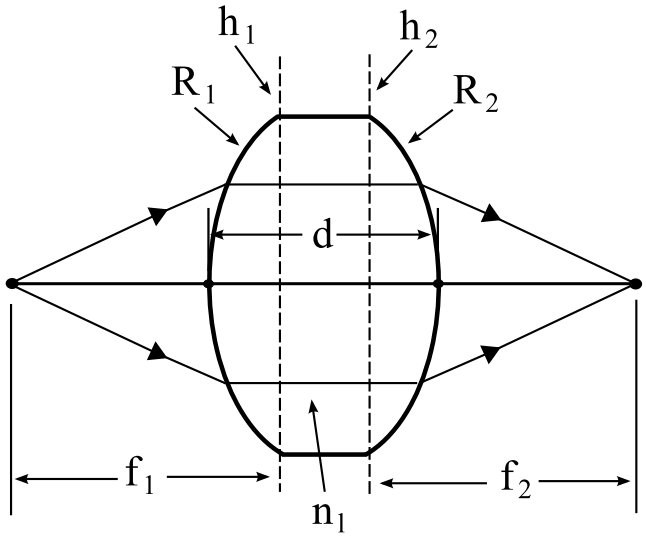

Figure 2.5. Diagram illustrating the basic parameters of a thick lens.

The equation for the numerical aperture of a diverging beam is given by

$$NA = n_0 \sin \theta_{half} \ , \tag{2.14}$$

where NA is the numerical aperture, n_0 is the index of refraction in the surrounding medium, and θ_{half} is the conical beam divergence angle measured from the centerline of the VCSEL to the farthest diverging ray. Figure 2.6 shows a diagram of the laser with the angle θ_{half}.

It is now appropriate to explain the sign convention that is used to determine the sign of the different radii of the lenses. Based on the incoming ray, the first surface encountered is called radius 1; while, the second is radius 2. Also, if the center of the radius is to the right of the vertex, then the radius has a positive sign. If the center is to the left of the vertex, then the sign is negative. For a planar surface the radius is positive infinity. It is also important to note that if the lens thickness d in equation (2.10) goes to zero, the equation reduces to (2.9), which is the thin lens equation.

2.3.3 Current Design

The most important criterion in the design of the optical system is that the configuration should be as simple as possible to reduce the number of lenses required. Also, it is ideal to avoid using lenses on the reflected beam, as this greatly reduces the number of parts that need to be fabricated. Another constraint is the overall size of the drag balance device. Since the floating disk sits about 7 mm from the plane

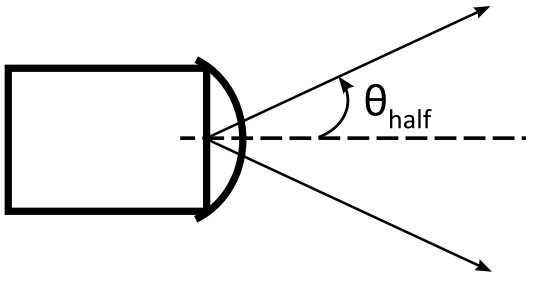

Figure 2.6. Illustration of the laser with the conical angle θ_{half} shown.

comprising the PSD, the entire optical path is about 140 mm. Therefore, the focal lengths of the lenses need to be small enough to fit whithin the allowable space.

With these considerations in mind, the final design concept is illustrated in Figure 2.7. Specifically, a plano-convex lens is used to collimate the diverging light beam emitted from the laser, followed by another plano-convex lens that focuses the collimated beam onto the surface of the spherical mirror. A collimated light beam of small diameter reflects off the mirror and impinges on the PSD.

An alternative design can be employed if an aspherical lens is used for either the focusing or collimating lens instead of plano-convex. Assuming identical focal lengths the quality of beam output will be enhanced. This is due to the decreased stray light that an asphere produces because of its unique shape. The GRIN lens was considered as a possible candidate to collimate the emitted light beam. However, due to size and focal length constraints it was ruled out.

To determine the lens parameters, it is convenient to start at the spherical mirror,

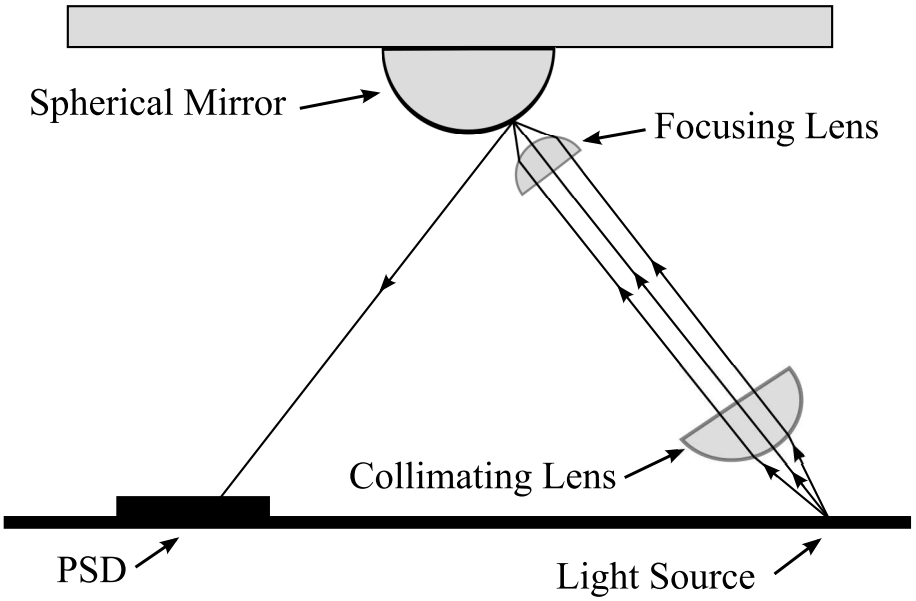

Figure 2.7. Schematic of the basic concept for the lens system, both the collimating and focusing lenses are plano-convex. The focusing lens could be exchanged with an aspherical lens of the same focal length. Not to scale.

and then work backwards through the system. Using (2.13),the focal length of the spherical mirror, assuming a radius of 1 mm, was calculated to be 0.5 mm. The radius of the convex side of the focusing lens was calculated to be 0.25 mm, based on the thin lens equation (2.9) using $f = 0.5$ mm, corresponding to the focal length of the spherical mirror along with $R_1 = \infty$. Since the same focal length was used for both the mirror and the focusing lens, the focused light will reflect from the mirror and diverge at the same rate, which causes a collimated beam to emerge from the mirror.

To collimate the light after it leaves the source, a plano-convex lens is used. The lens needs to have a numerical aperture that is at least as big as that of the laser. This allows all of the light to be captured by the lens. The numerical aperture of the diverging laser is calculated from equation (2.14), using a divergence angle $\theta_{half} = 6$ degrees, as specified by the manufacturer of the VCSEL. This yields $NA = 0.105$. The focal length of the collimating lens is chosen to ensure that the diameter of the collimated beam is small enough to enter the focusing lens; this value must be less than 0.5 mm. The required focal length cannot be any larger than 2.4 mm, which was calculated using trigonometry. The radius of the lens is be calculated by applying the thin lens equation (2.9). Using a focal length of 2.0 mm, with $R_2 = \infty$ and an index of refraction of $n_1 = 1.5$, then (2.9) yields $R_1 = 1$ mm.

From the above analysis, Figure 2.8 shows the final optical system including dimensions. The collimating lens is placed 2 mm away from the laser; while the focusing lens is placed 0.5 mm away from the spherical mirror. Despite the fact that these are very close distances, a fixture may be machined to hold the lenses in place, with fine focusing adjustment for each lens, if needed.

2.4 Physical Experiment

A physical system was constructed based on the design in the previous section. The lenses that were obtained had slightly different focal lengths than those in the design due to limitations in availability by the manufacturer. However, differences were minimal. A mounted asphere was purchased with a focal length of 1.45 mm,

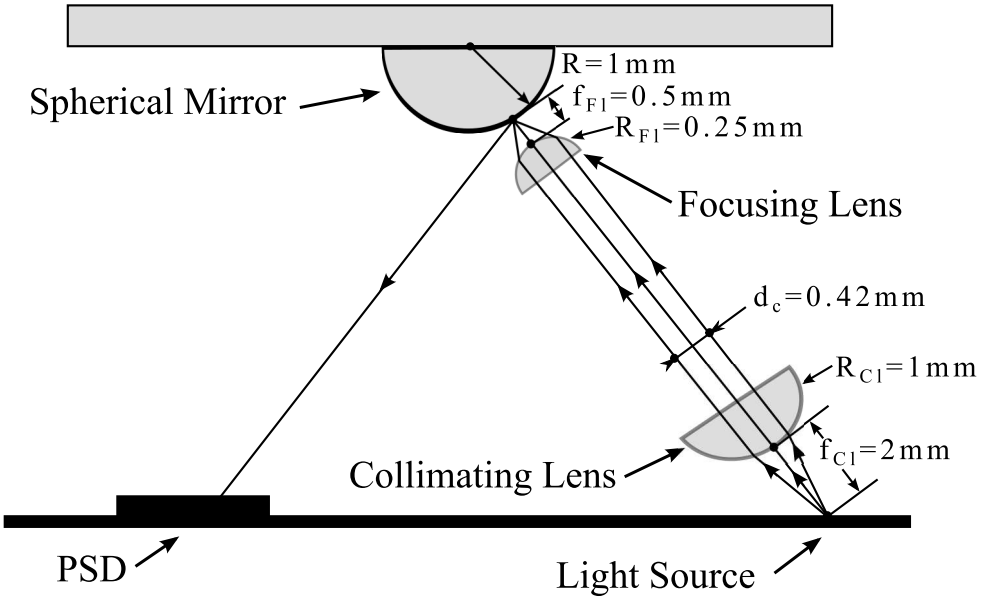

Figure 2.8. Schematic of the lens system, with all the final dimensions listed. Not to scale.

which was used as the collimating lens. Another aspherical lens, with a focal length of 0.45 mm, was used as the focusing lens. Finally, a precision ball bearing with a diameter of 1.9 mm and a surface roughness of 1 μ'' (micro-inch) was used as the spherical mirror.

In the experimental set up, all lenses were held in place in a 2-D plane, along with the laser and spherical mirror, similar to the arrangement in Figure 2.7. The spherical mirror was mounted on a 2-D slider with a fine adjustment. The light path was observed through a video camera, capable of detecting in the infrared spectrum.

Several problems were encountered during testing. First of all, the diameter of the emitted light beam was too large for the collimating lens. Therefore, not all of the emitted light was captured and focused. The reason for this error comes from the assumption that the light is a point source. This was not the case for the VCSEL, because it had a built in dome shape lens that gave the emitted light beam an initial diameter before divergence. This could be corrected by purchasing a different lens or using an aperture stop to restrict the diameter of the emitted

light beam. Secondly, the light reflected from the spherical mirror underwent diffuse reflection due to microscopic surface roughness of the ball bearing. It was impossible to purchase an off-the-shelf spherical mirror having a small enough focal length for the present application. To pursue the optical advantage concept further, it is necessary to identify a means of custom fabricating a spherical a spherical mirror of diameter 1.9 mm with a surface finish of 40-20 scratch-dig. Mirror surface finish is measured in terms of scratch and dig. A scratch is a marking or tear in the mirror surface, while a dig is a rough spot or pit. The numbers correspond to maximum allowable dimensions for scratches and digs. A list of typical mirror scratch-dig values can be found in Table 2.2. An attempt was made to use a fiber optic strand to guide the emitted light up to the spherical mirror. Despite having a very small gap between the end of the fiber and the surface of the mirror, the reflected light still diffused and was not able to be detected by the PSD.

The main difficulties in the experiment stem from (i) the divergence of the emitted light as it exits the laser and (ii) the surface roughness of the spherical mirror. Also, it was challenging to assess the behavior of the light since the laser emitted infrared light, that could not be seen by eye. Furthermore, the lenses, with such small focal lengths, are very delicate and prone to damage if handled improperly. Finally, mounting and securing the components proved especially challenging given the fact that all components had to fit within a small footprint. With all of these factors taken into account and with budget and time constraints, it was decided to abandon the optical advantage system and simply mount the VCSEL directly in the center of the disk.

Table 2.2. Typical values of scratch-dig for spherical mirrors

Scratch-Dig	Application
60-40	Used for low-power laser and imaging applications
40-20	Ideal for laser and imaging applications with collimated beams
20-10	Excellent for laser systems with focused beams
10-5	For most demanding laser systems where low scatter is critical

CHAPTER 3

MATHEMATICAL MODEL OF A 2-D FLOATING DISK MASS SPRING DAMPER SYSTEM

3.1 Introduction

This chapter presents a two-dimensional mathematical model for a disk that is floating on a pool of liquid with springs attached. A schematic of the system in its equilibrium position is shown in Figure 3.1. The disk has a mass m and radius R. Three springs are attached to the center of the disk and radiate outward to the housing at 120° from each other. The springs are pre-stretched, so they always exert a tension force on the disk. The position vectors of each of the springs in their equilibrium position are given by

$$\begin{aligned}
\vec{L}_{01} &= L_{01}\cos 120^\circ\,\hat{i} + L_{01}\sin 120^\circ\,\hat{j}\ , \\
\vec{L}_{02} &= L_{02}\,\hat{i}\ , \\
\vec{L}_{03} &= L_{03}\cos 240^\circ\,\hat{i} + L_{03}\sin 240^\circ\,\hat{j}\ .
\end{aligned} \tag{3.1}$$

In each case, the tail of the vector is located at the origin with the tip located at the respective housing juncture labeled 1,2,3 in Figure 3.1. In (3.1), L_{01}, L_{02}, L_{03} denote the length of the pre-stretched springs. Ideally, to ensure symmetry $L_{01} = L_{02} = L_{03}$. The liquid pool beneath the disk constrains the motion of the disk to the horizontal plane. As the disk moves under the applied wind-driven shear stress, the springs are

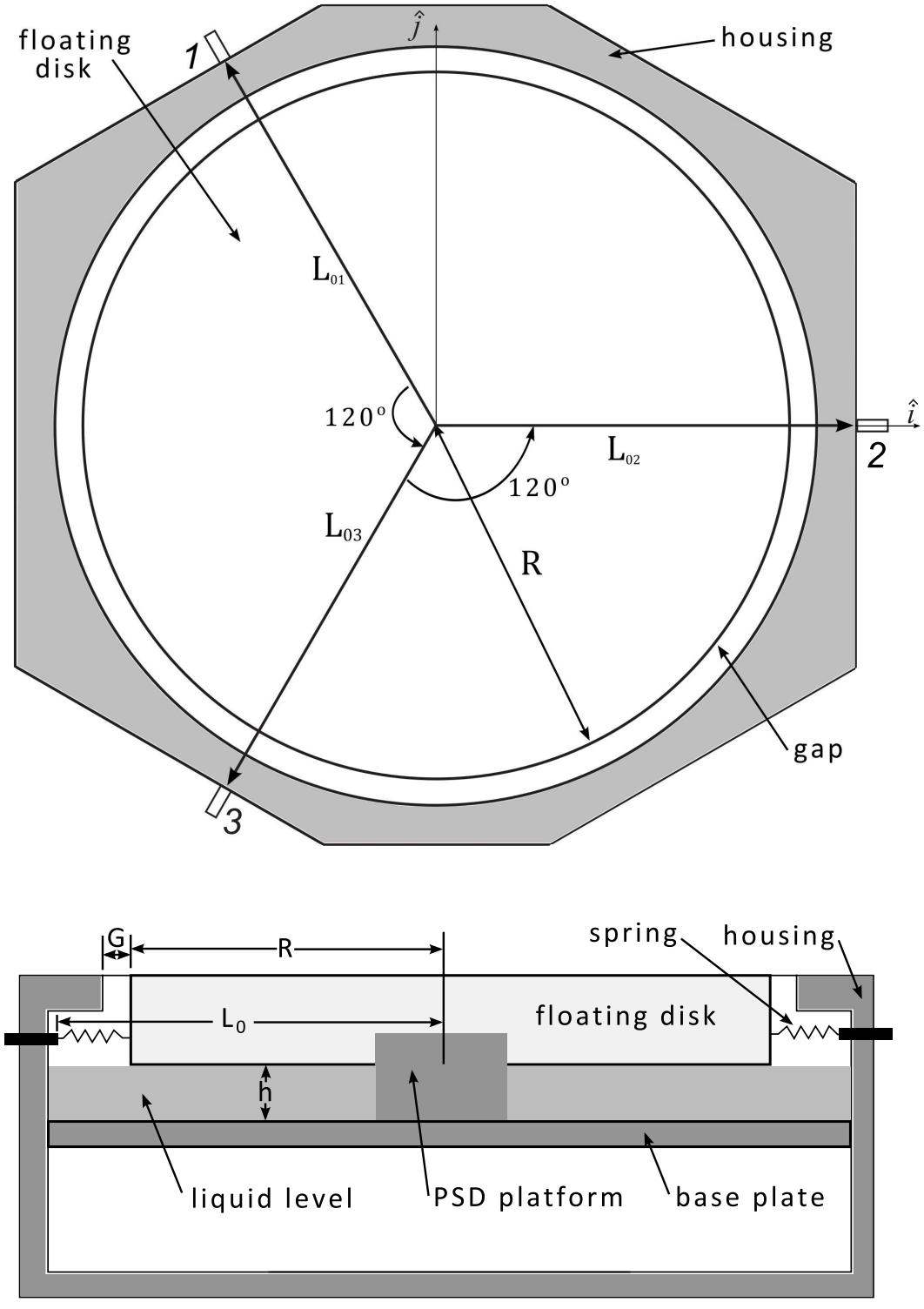

Figure 3.1. Planform view of the drag plate in the equilibrium position. Three springs are attached to the centroid of the floating disk, and connect to the housing at swivel junctures labeled 1,2,3.

displaced from equilibrium. Disk motion is further resisted by the viscous force present between the disk and the liquid.

The overall mathematical model is divided into three parts. The first part involves the determination of an effective spring constant resolved along the direction of motion. The second part involves the determination of the viscous damping force, which can be related to a damping coefficient. The third part is the simulation of the entire equation of motion, using Simulink.

3.2 Models

3.2.1 Effective Spring Constant

Each of the three individual springs in the system has a spring constant k, and combine in such a way to yield an effective spring constant, k_{eff}, defined such that

$$\vec{F}_s = k_{eff}\,\vec{r}_0 \ , \tag{3.2}$$

where $\vec{F}_s$ denotes the net restoring force and $\vec{r}_0$ denotes the displacement of the disk centroid relative to undisturbed equilibrium position, as shown in Figure 3.2. Since the springs are pretensioned, $\vec{F}_s$ and $\vec{r}_0$ always acts in the direction away from the center of the disk and toward the origin. In the coordinate system given in Figure 3.2,

$$\vec{r}_0 = -r_0 \cos(\theta)\hat{i} - r_0 \sin(\theta)\hat{j} \ . \tag{3.3}$$

The displacement vectors $\vec{r}_1, \vec{r}_2, \vec{r}_3$ are defined such that the tail of the vectors remain colocated with the centroid of the disk as it moves, while the tips remain located at the housing junctures,

$$\begin{aligned}
\vec{r}_1 &= (L_{01}\,\cos 120^\circ - r_0\,\cos\theta)\,\hat{i} + (L_{01}\,\sin 120^\circ - r_0\,\sin\theta)\,\hat{j} \ , \\
\vec{r}_2 &= (L_{02} - r_0\,\cos\theta)\,\hat{i} - r_0\,\sin\theta\,\hat{j} \ , \\
\vec{r}_3 &= (L_{03}\,\cos 240^\circ - r_0\,\cos\theta)\,\hat{i} + (L_{03}\,\sin 240^\circ - r_0\,\sin\theta)\,\hat{j} \ .
\end{aligned} \tag{3.4}$$

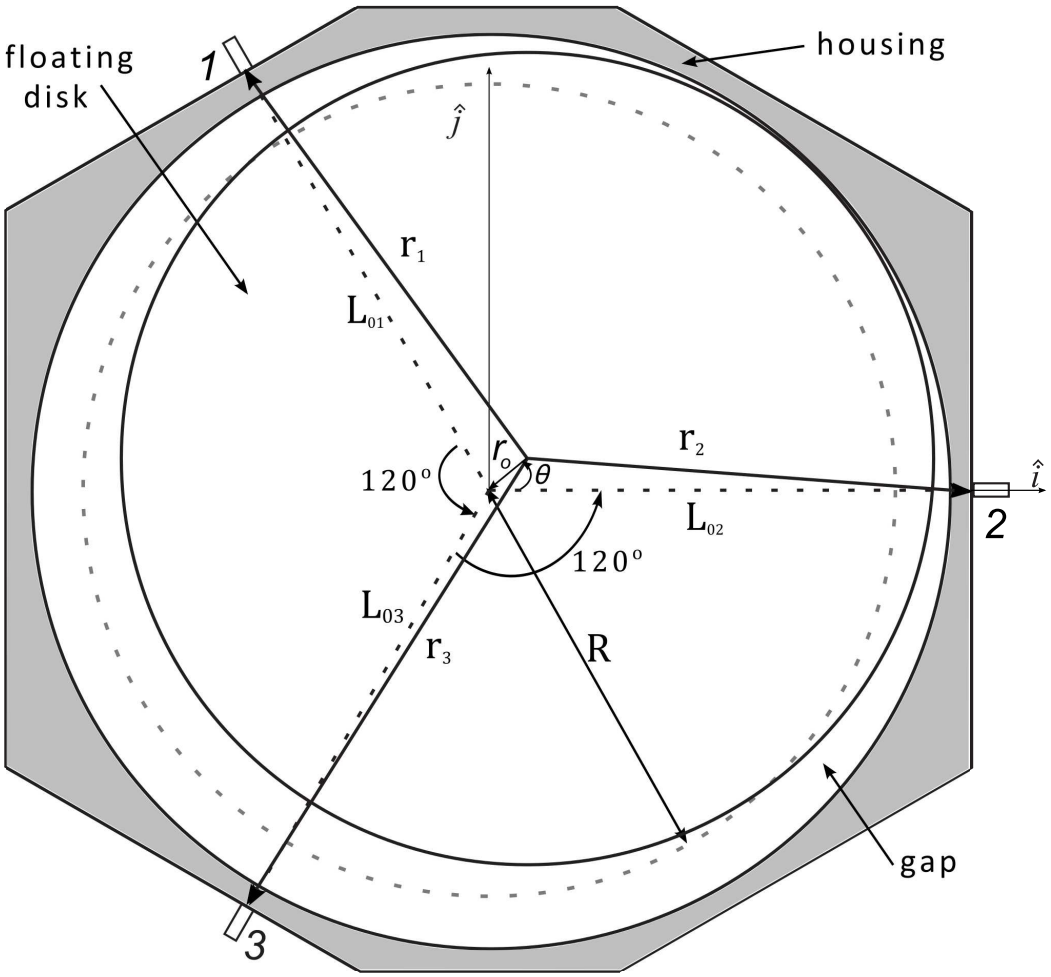

Figure 3.2. Planform view of the drag plate in an arbitrary displaced position with the equilibrium configuration shown in dashed lines.

To determine k_{eff}, the net restoring force is written as a vector sum of the individual restoring forces associated with each spring,

$$\vec{F}_s = k\,\Delta_1\,\hat{r}_1 + k\,\Delta_2\,\hat{r}_2 + k\,\Delta_3\,\hat{r}_3 \ , \tag{3.5}$$

where $\Delta_1, \Delta_2, \Delta_3$ represent the change in length of each spring during the displacement, $\Delta_i = |\vec{r}_i| - l_0$, for $i = 1, 2, 3$, where l_0 $(= L_{0i} - L_{0is})$ denotes the unstretched length of each spring and L_{0is} denotes the amount of pretension in the i^{th} spring and $\hat{r}_1, \hat{r}_2, \hat{r}_3$ represent the unit vectors along the direction of the displacement vectors

$\vec{r}_1, \vec{r}_2, \vec{r}_3$, respectively, and the magnitudes are given by

$$\begin{aligned}
|\vec{r}_1| &= [(L_{01}\cos 120^\circ - r_0\cos\theta)^2 + (L_{01}\sin 120^\circ - r_0\sin\theta)^2]^{1/2} \ , \\
|\vec{r}_2| &= [(L_{02} - r_0\cos\theta)^2 + (-r_0\sin\theta)^2]^{1/2} \ , \\
|\vec{r}_3| &= [(L_{03}\cos 240^\circ - r_0\cos\theta)^2 + (L_{03}\sin 240^\circ - r_0\sin\theta)^2]^{1/2} \ .
\end{aligned} \tag{3.6}$$

The amount of pretension in the springs must be sufficient to ensure $\Delta_i > 0$ for $i = 1, 2, 3$ over the full range of expected displacements $r_0 < r_{0,max}$ and all angles $0^\circ \leq \theta < 360^\circ$. This guarantees that the restoring force will always act in the correct direction to bring the system back to equilibrium. Equating (3.2) and (3.5) gives

$$k_{eff}\,\vec{r}_0 = k(\Delta_1\,\hat{r}_1 + \Delta_2\,\hat{r}_2 + \Delta_3\,\hat{r}_3) \ . \tag{3.7}$$

Considering only the magnitudes of the two sides, the effective spring constant may be written as

$$\frac{k_{eff}}{k} = \frac{|\Delta_1\,\hat{r}_1 + \Delta_2\,\hat{r}_2 + \Delta_3\,\hat{r}_3|}{r_0} \ . \tag{3.8}$$

Substituting in for $\Delta_1, \Delta_2, \Delta_3$ and the unit vectors $\hat{r}_1, \hat{r}_2, \hat{r}_3$,

$$\frac{k_{eff}}{k} = \frac{|(1 - \frac{l_0}{r_1})\vec{r}_1 + (1 - \frac{l_0}{r_2})\vec{r}_2 + (1 - \frac{l_0}{r_3})\vec{r}_3|}{r_0} \ . \tag{3.9}$$

Now, substituting in for $\vec{r}_1, \vec{r}_2, \vec{r}_3$

$$\begin{aligned}
\frac{k_{eff}}{k} = r_0^{-1}[&((1 - \frac{l_0}{r_1})(L_{01}\cos 120^\circ - r_0\cos\theta) + (1 - \frac{l_0}{r_2})(L_{02} - r_0\cos\theta) \\
&+ (1 - \frac{l_0}{r_3})(L_{03}\cos 240^\circ - r_0\cos\theta))^2 + ((1 - \frac{l_0}{r_1})(L_{01}\sin 120^\circ - r_0\sin\theta) \\
&+ (1 - \frac{l_0}{r_2})(-r_0\sin\theta) + (1 - \frac{l_0}{r_3})(L_{03}\sin 240^\circ - r_0\sin\theta))^2]^{1/2} \ .
\end{aligned} \tag{3.10}$$

The only two design parameters that need to be specified in order to plot k_{eff}/k as a function of r_0 and θ are (i) the unstretched length of the springs, l_0, and (ii) the amount of pre-stretch, L_{0s}. Figure 3.3 shows the variation of k_{eff}/k as a function of position θ and r_0, using the values of $l_0 = 72.6$ mm and $L_{0s} = 18.4$ mm.

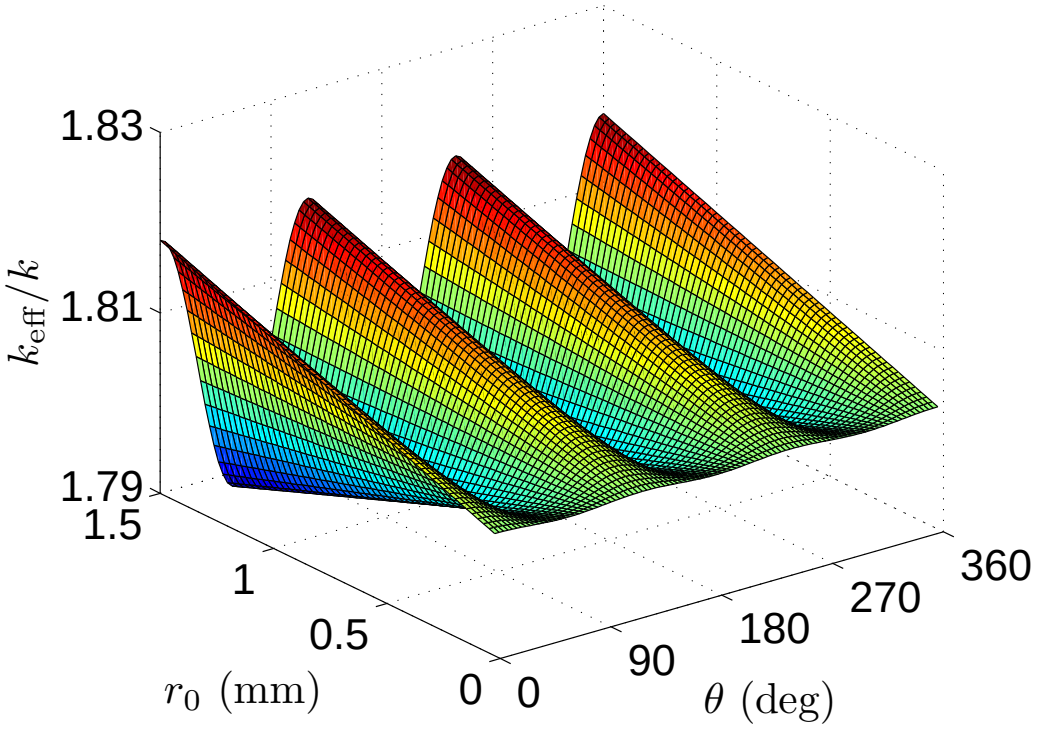

Figure 3.3. Effective spring constant ratio of the system as a function of position θ and r_0 using input parameters $l_0 = 72.6$ mm and $L_{0s} = 18.4$ mm.

Results indicate that the effective spring constant weakly depends on the direction and magnitude of the displacement. The average value over the full range, $0 \leq r_0 \leq 1.5$ mm and $0° \leq \theta < 360°$, is $k_{eff}/k = 1.803 \pm 0.0147$. The error in assuming one single value for k_{eff}/k independant of r_0 and θ remains less than 1% over the full operating range. Figures 3.4 and 3.5 show two different slices of k_{eff}/k for the cases $r_0 = 0.5$ mm and $\theta = 0°$, respectively. For the case $r_0 = 0.5$ mm, the average effective spring constant ratio is $k_{eff}/k = 1.803 \pm 0.0046$, which represents only a 0.28% error.

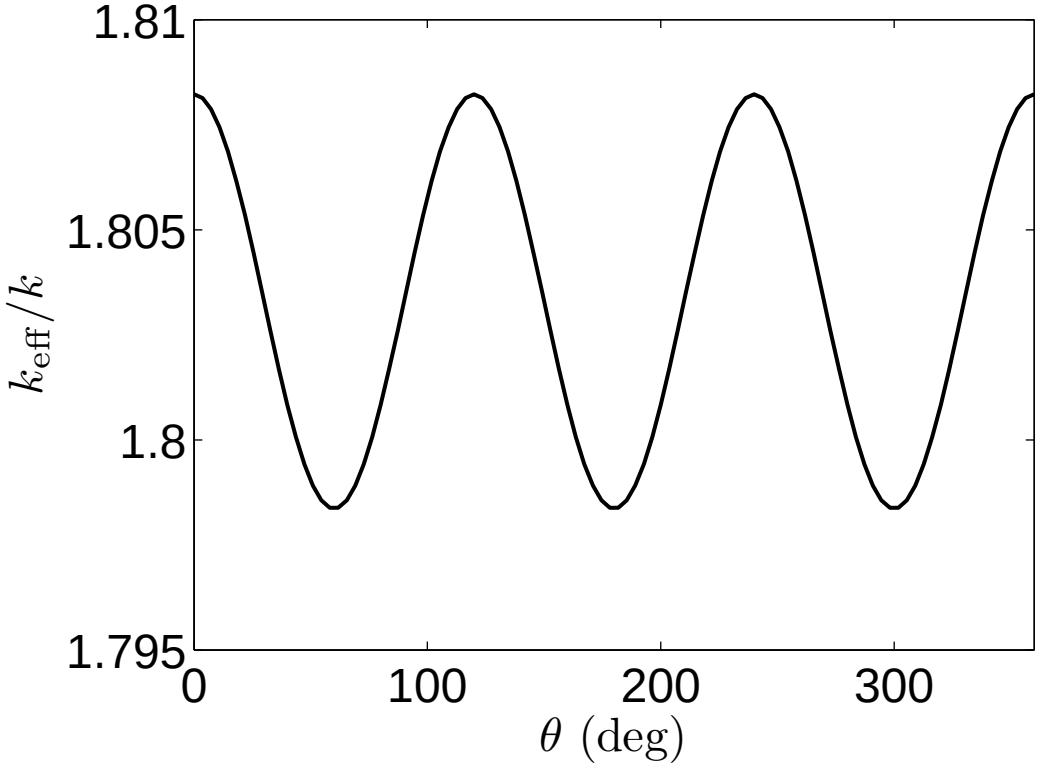

Figure 3.4. Effective spring constant ratio of the system as a function of the direction of the displacement θ for the case of $r_0 = 0.5$ mm using input parameters $l_0 = 72.6$ mm and $L_{0s} = 18.4$ mm.

3.2.2 Viscous Damping Force

The viscous damping force is modeled based on 2-D, unsteady Couette flow. This type of flow occurs between two infinite parallel plates separated by a finite gap, h. Figure 3.6 presents a schematic of the model. For clarity, the shear stress on the underside of the disk is reffered to as the "damping" shear stress, τ_d; wheras the shear stress on the top of the disk is reffered to as the "applied" shear stress, τ_a, due to the wind-driven boundary layer flow over the disk. The velocity of the liquid in the gap is denoted as $u = u(y, t)$. A similar type of model has been developed by Ingard & Akay (1987) for the case of flow between a rotating blade and a stationary guard. The present Couette flow model differs from the rotating blade in that the

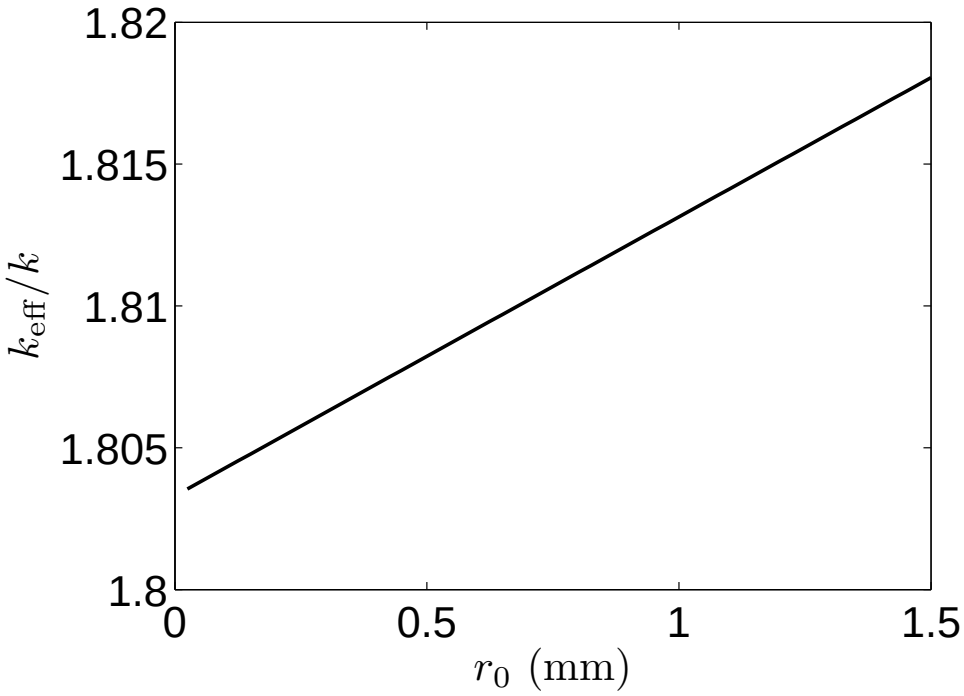

Figure 3.5. Effective spring constant ratio of the system as a function of the displacement magnitude r_0 for the case of $\theta = 0°$ using input parameters $l_0 = 72.6$ mm and $L_{0s} = 18.4$ mm.

lower plate remains stationary, while the upper oscillates sinusoidally. This makes the problem unsteady. The purpose for developing the unsteady Coutte flow model is to determine the damping shear force of the system, which can then be used in the overall equation of motion for the disk.

The damping shear stress, assuming the liquid behaves as a Newtonian fluid, is needed, which is then multiplied by the surface area of the disk that is in contact with the damping liquid. The damping shear stress is defined as

$$\tau_d = \mu \left. \frac{du}{dy} \right|_{y=h} , \tag{3.11}$$

μ denotes the absolute viscosity of the fluid. The velocity field $u(y,t)$ is determined by solving the Navier-Stokes equation for a fluid between two plates,

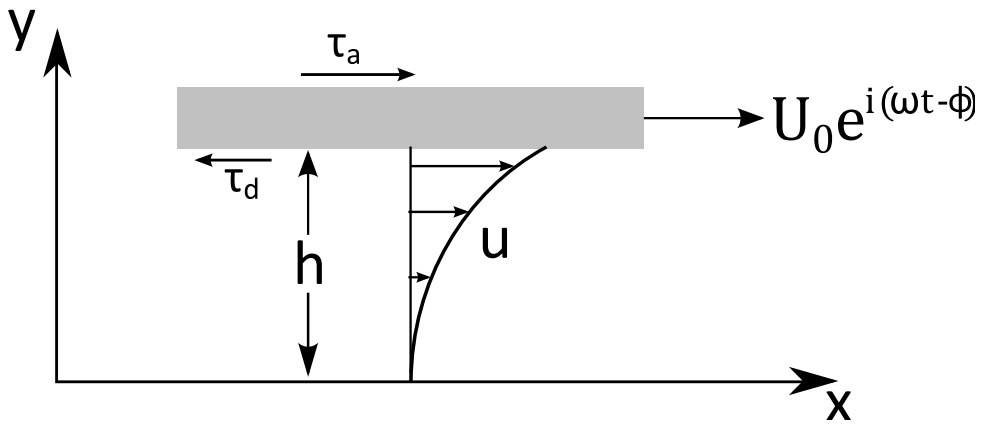

Figure 3.6. Diagram of the unsteady Couette flow problem, assuming the upper boundary moves sinusoidally, at a frequency ω. The applied and damping shear stresses are denoted as τ_a and τ_d, respectively.

$$\frac{\partial u}{\partial t} = \nu \frac{\partial^2 u}{\partial y^2} \,, \tag{3.12}$$

where ν is the kinematic viscosity of the fluid and t represents time.

One can solve (3.12) using a separation of variables technique (Drazin & Riley, 2006). A complete derivation may be found in Appendix B, where the resultant solution was taken from (B.22) and displayed here. The resultant solution to (3.12) is

$$\begin{aligned} u(t,y) = & \frac{U_0 \cos(\omega t - \phi)\left[\cos\beta\cos\beta\tilde{y}\sinh\beta\tilde{y}\sinh\beta + \sin\beta\tilde{y}\sin\beta\cosh\beta\tilde{y}\cosh\beta\right]}{\left[\cos^2\beta\sinh^2\beta + \sin^2\beta\cosh^2\beta\right]} \\ & - \frac{U_0 \sin(\omega t - \phi)\left[\cos\beta\sin\beta\tilde{y}\cosh\beta\tilde{y}\sinh\beta - \cos\beta\tilde{y}\sin\beta\sinh\beta\tilde{y}\cosh\beta\right]}{\left[\cos^2\beta\sinh^2\beta + \sin^2\beta\cosh^2\beta\right]} \,, \end{aligned} \tag{3.13}$$

where U_0 represents the amplitude of the velocity of the disk, ω is the frequency of oscillation, $\tilde{y} \equiv (y/h)$ denotes the nondimensional vertical coordinate, and the Womersley number is introduced as $\beta = \sqrt{\omega/2\nu}h$. The damping shear stress is found by taking the derivative of (3.13) with respect to $\tilde{y}$, then evaluating it at $\tilde{y} = 1$ and multiplying by the absolute viscosity μ. After some additional manipulation, the damping shear stress may be written as

$$\tau_d = \frac{\mu U_0 \sqrt{\omega/2\nu}\,(\cos(\omega t-\phi)(\sinh\beta\cosh\beta+\sin\beta\cos\beta))}{(\cos^2\beta\sinh^2\beta+\sin^2\beta\cosh^2\beta)} - \frac{\mu U_0\sqrt{\omega/2\nu}(\sin(\omega t-\phi)\,(\sinh\beta\cosh\beta-\cos\beta\sin\beta))}{(\cos^2\beta\sinh^2\beta+\sin^2\beta\cosh^2\beta)}\ . \quad (3.14)$$

The damping force, F_d, is then simply the damping shear stress times the surface area, A_s, in contact with the liquid, i.e.

$$F_d = \tau_d A_s\ . \quad (3.15)$$

Two observations can be made concerning (3.15). First of all, a phase shift, γ, in the form

$$\gamma = \arctan\left(\frac{\sinh(\beta)\cosh(\beta)-\cos(\beta)\sin(\beta)}{\sinh(\beta)\cosh(\beta)+\cos(\beta)\sin(\beta)}\right)\ , \quad (3.16)$$

exists between the damping force and the velocity of the disk (see Appendix B). Figure 3.7 shows the behavior of γ as a function of Womersley number, β. For $\beta > 1$, the phase shift plateaus at 45°, i.e., the damping force lags the velocity by 45°. For $\beta < 0.16$, the phase shift remains less than 1° and thus may be neglected. Secondly, the ratio of amplitudes between the damping force and velocity of the disk can be written as

$$c = \sqrt{2}\left(\frac{A_s\mu\beta}{h}\right)\frac{[\sinh^2(\beta)\cosh^2(\beta)+\sin^2(\beta)\cos^2(\beta)]^{1/2}}{[\sinh^2(\beta)\cos^2(\beta)+\sin^2(\beta)\cosh^2(\beta)]}\ . \quad (3.17)$$

Figure 3.8 shows the behavior of c as a function of Womersley number.

Therefore, assuming a disk velocity of

$$V = U_0\cos(\omega t-\phi)\ , \quad (3.18)$$

the damping force can be expressed as

$$F_d = cU_0\cos(\omega t-\phi+\gamma)\ . \quad (3.19)$$

The relation between V and F_d is illustrated in Figure 3.9 for generic values of c and γ. For small Womersley numbers ($\beta << 1$), $\gamma \approx 0$ and c =constant. In this case, the equations of motion describing the behavior of the drag balance have a

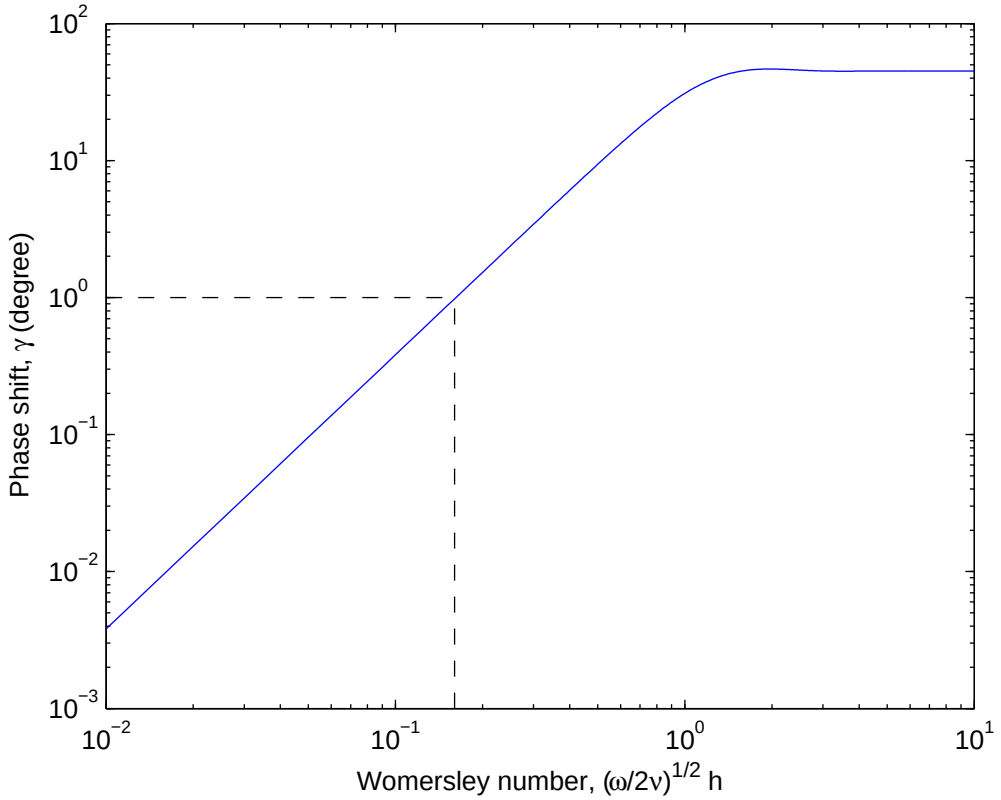

Figure 3.7. Phase shift between the damping shear stress and the disk velocity as a function of Womersley number based on (3.16). The dashed lines highlight the critical Womersley number, below which the phase shift may be assumed negligible.

constant damping coefficient (as discussed further in section 3.3). This is the desired operating regime since it simplifies the calibration of the device, and thus makes it a viable option as an instrument for directly measuring surface shear stress.

3.3 Equation of Motion (EOM)

The unsteady behavior of the present drag balance obeys Newton's second law, $F = ma$, applied to the system shown in Figure 3.10,

$$m\,\ddot{x} + F_d + F_s = F_a \quad , \tag{3.20}$$

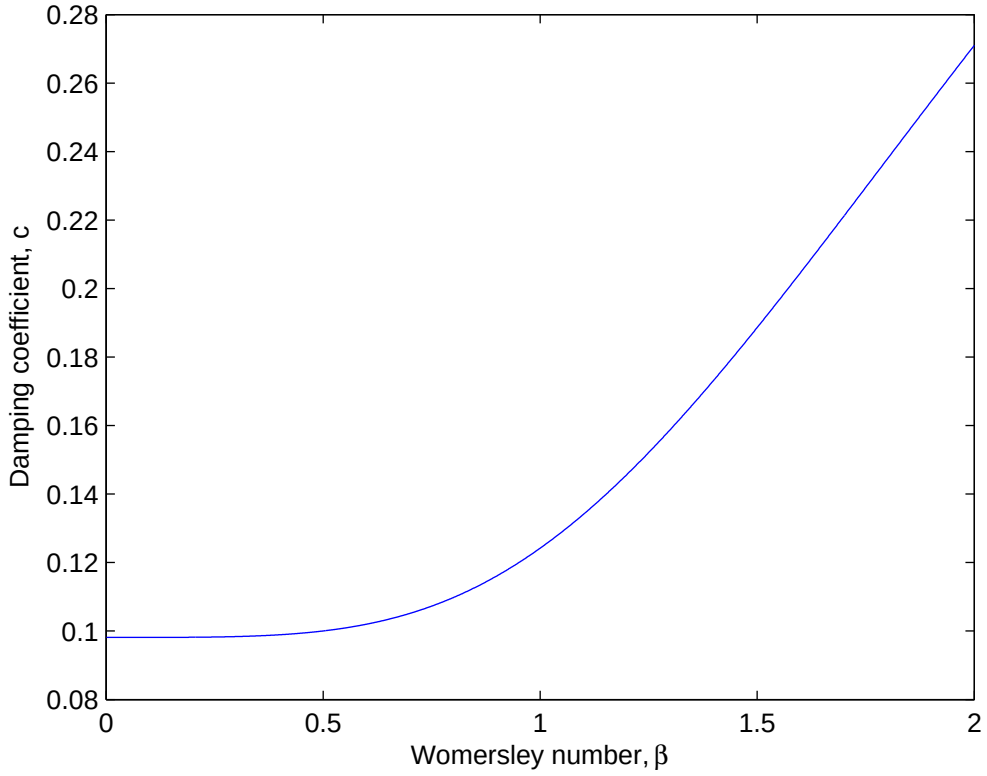

Figure 3.8. Damping coefficient c versus the Womersley number β based on (3.17). With input parameters: $A_s = 3.384 \times 10^{-3}$ m^2, $\mu = 0.058$ Ns/m^2 and $h = 2 \times 10^{-3}$ m.

where F_d, F_s, F_a represent the viscous damping force, restoring spring force, and applied force due to the wind shear, respectively. Here, $F_a = \tau_a \, A_d$, where τ_a denotes the shear stress due to the wind and A_d $(= \pi/4D^2)$ is the surface area of the disk. Based on sections 3.2.1 and 3.2.2, the EOM in (3.20) may be written as

$$m \, \ddot{x} + \tau_d \, A_s + k_{eff} \, x = F_a \ . \tag{3.21}$$

3.3.1 Applied Forcing Function Model

The applied force acting on the drag balance is a complicated function that depends on the nature of the turbulence in the atmospheric boundary layer at any given time. Since atmospheric flow is characterized by a high $R_\tau \approx 500,000$ based

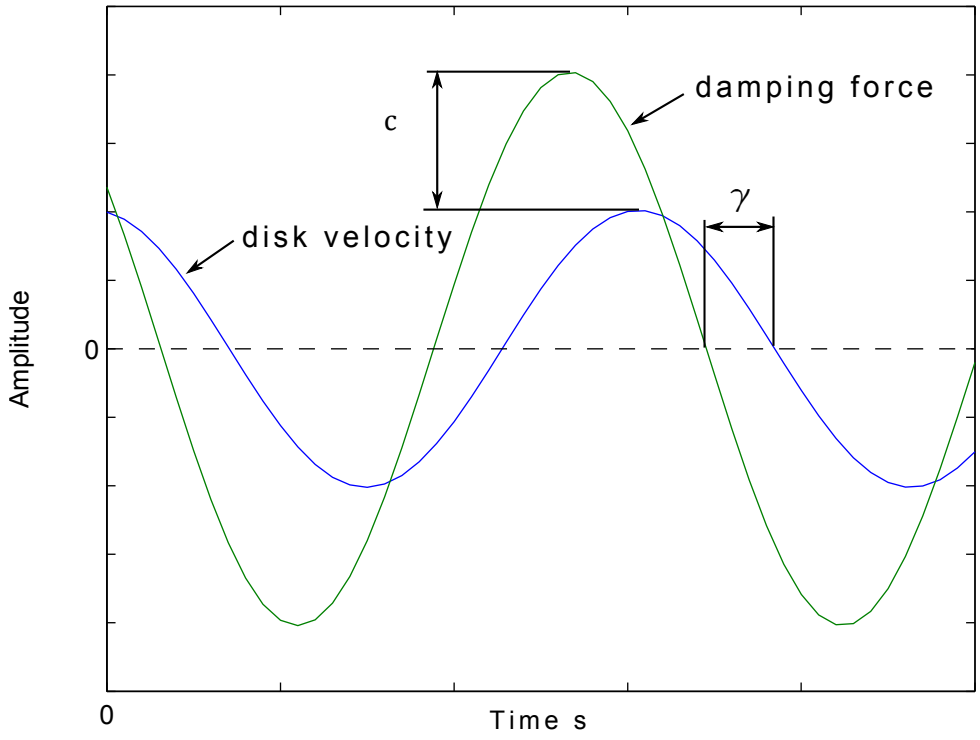

Figure 3.9. Damping force on the disk relative to the velocity of the disk, where γ and c represent the phase shift and amplitude ratio, respectively.

on friction velocity and boundary layer thickness, the turbulent flow over the floating disk will be comprised of a very large range of length and time scales. For this reason, it is convenient to express a time-record of the applied force in terms of a Fourier series as

$$F_a(t) = A_0 + \sum_{n=1}^{\infty} \left[A_n \cos(n\omega_0 t) + B_n \sin(n\omega_0 t) \right] , \quad 0 \le t \le T \ , \tag{3.22}$$

where the coefficients are determined as

$$A_0 = \frac{1}{T} \int_0^T F_a(t)\, dt \,, \quad A_n = \frac{2}{T} \int_0^T F_a(t) \cos(n\omega_0 t)\, dt \,,$$

$$B_n = \frac{2}{T} \int_0^T F_a(t) \sin(n\omega_0 t)\, dt \,. \qquad \text{for } n = 1, 2, \ldots \tag{3.23}$$

The representation in (3.22) assumes that $F_a(t)$ possesses a fundamental frequency $\omega_0 = 2\pi/T$. In the application of turbulence, an inherently non periodic process,

(3.22) still provides an accurate description as long as T remains much larger than the integral time scale of the flow and an appropriate preconditioner (such as hamming window) is used to remove end effects in the time-record.

3.3.2 Response to Harmonic Forcing

If the system in (3.20) indeed behaves linearly, then one can consider the response of the system to an individual Fourier mode and apply the principle of superposition to obtain the response to a summation of modes such as expressed generally in (3.22). The unsteady behavior of the present drag balance obeys Newton's second law, $F = ma$, applied to the system shown in Figure 3.10. For the case of a single Fourier mode, (3.20) can be rewritten as

$$m\,\ddot{x} + \tau_d\,A_s + k_{eff}\,x = f_0 \sin(\omega t) \ . \tag{3.24}$$

To solve (3.24), a solution is assumed of the form

$$x = X \sin(\omega t - \phi) \ , \tag{3.25}$$

where X is the amplitude of the position of the disk, and ϕ is the phase shift of the disk position. Substituting in for τ_d using (B.24) from Appendix B, and recognizing that $U_0 = \omega\,X$,

$$-\omega^2 X \sin(\omega t - \phi) + \frac{c}{m}\omega X \cos(\omega t - \phi + \gamma) + \omega_n^2 X \sin(\omega t - \phi) = \frac{f_0}{m} \sin(\omega t)\,. \tag{3.26}$$

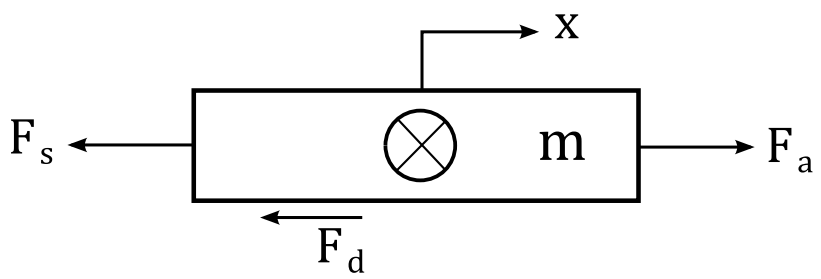

Figure 3.10. Free body diagram of the drag balance system.

After some algrebraic manipulations (see appendix C), and separating the sine and cosine terms gives,

$$[-\omega^2 X\cos(\phi) + 2\zeta\omega_n\omega X\cos(\gamma)\sin(\phi) - 2\zeta\omega_n\omega X\sin(\gamma)\cos(\phi) + \omega_n^2 X\cos(\phi) - f_0/m]\sin(\omega t) = 0 \ , \tag{3.27}$$

$$[\omega^2 X\sin(\phi) + 2\zeta\omega_n\omega X\cos(\gamma)\cos(\phi) + 2\zeta\omega_n\omega X\sin(\gamma)\sin(\phi) - \omega_n^2 X\sin(\phi)]\cos(\omega t) = 0 \ . \tag{3.28}$$

To find the phase shift, ϕ, (3.28) is simplified, which yields

$$\phi = \arctan\left(\frac{2\zeta(\omega/\omega_n)\cos(\gamma)}{(1-(\omega/\omega_n)^2) - 2\zeta(\omega/\omega_n)\sin(\gamma)}\right) \ , \tag{3.29}$$

where

$$\gamma = \arctan\left(\frac{\sinh(\beta)\cosh(\beta) - \sin(\beta)\cos(\beta)}{\sinh(\beta)\cosh(\beta) + \sin(\beta)\cos(\beta)}\right) \ , \tag{3.30}$$

$$\omega_n^2 = \frac{k_{eff}}{m} \ , \tag{3.31}$$

$$\beta = \sqrt{\frac{\omega}{2\,\nu}} \ , \tag{3.32}$$

$$\zeta = \frac{c}{2m\omega_n} = \zeta_0\sqrt{2}\beta\frac{[\sinh^2(\beta)\cosh^2(\beta) + \sin^2(\beta)\cos^2(\beta)]^{1/2}}{[\cos^2(\beta)\sinh^2(\beta) + \sin^2(\beta)\cosh^2(\beta)]} \ . \tag{3.33}$$

Note, $\gamma = \gamma(\beta)$ and $\zeta = \zeta(\beta)$. Additionally, $\zeta_0 = \mu A_s/2mh\omega_n$ represents a nondimensional number that characterizes the strength of the damping coefficient for the case of steady Couette flow, as shown in Appendices B and C.

The transfer function (TF) is now found by taking (3.27) and simplifying, using substitutions for $\tan(\phi)$ and $\cos(\phi)$, which gives

$$\frac{X}{f_0/k_{eff}} = \frac{1}{[(2\zeta(\omega/\omega_n)\cos(\gamma))^2 + (1-(\omega/\omega_n)^2 - 2\zeta(\omega/\omega_n)\sin(\gamma))^2]^{1/2}} \ . \tag{3.34}$$

3.3.3 Model-Based Design Choices

In the work of Sadr and Klewicki (2000), actual shear stresses measured on the salt playa of Utah's western desert spanned between $0.03 < \tau_a < 0.06$ Pa. Taking these values and multiplying by the disk area, $A_d = 12.68 \times 10^{-3}$ m^2, provides an estimate for the magnitude of the applied force, $f_0 = 7.9 \times 10^{-4}$ N, that represents typical operating conditions. With the expected applied force magnitude determined, the effective spring constant, k_{eff}, is found using the equation for the force in a spring $f_0 = k_{eff}\, x$, where x is taken as the gap size, G, based on the analysis from section 1.3. The effective spring constant, k_{eff}, is calculated to be 0.6042 N/m. The individual spring constant is determined from the ratio of k_{eff}/k, as given by (3.10) and calculated to be 0.3351 N/m.

The total mass for the system is measured, which includes the mass of the springs and the spring connector hub, as 0.0075 kg. The natural frequency, $\omega_n = \sqrt{k_{eff}/m}$, is determined using the effective spring constant and the total mass of the system. With the natural frequency determined, the desired damping coefficient for a linear system is calculated using a damping ratio of 0.707. The desired damping constant is calculated as 0.0889 kg/s. The difficulty arises in finding a damping fluid viscosity to match this desired equivalent value. For this purpose, Figure 3.8 is used to determine what approxiamate value of % glycerin yields the necessary damping coefficient, which is found to be around 85%. The corresponding values for viscosity are dynamic $\mu = 0.058\ Ns/m^2$, and kinematic $\nu = 4.77e^{-5}\ m^2/s$. These main parameters of the mathematical model are found in Table 3.1 for easy reference.

3.3.4 Simulation Results

With all of the parameters known, the constant damping coefficient case and the variable damping coefficient model are compared. This is done by plotting the constant damping coefficient case, then overlaying the variable damping model on the same graph. Both the transfer function and the phase shift are plotted in this manner. These plots are illustrated in Figures 3.11 and 3.12, where the variable

Table 3.1. Final design parameter values

Parameter	Value	Unit
G (gap size)	1.5	mm
A_d (disk area)	12.68e-3	m^2
f_0 (forcing amplitude)	7.917e-4	N
k_{eff} (effective spring constant)	0.6042	N/m
k (individual spring constant)	0.3351	N/m
ζ_0 (damping ratio)	0.707	-
m (total mass)	0.0075	kg
ω_n (natural frequency)	8.38	rad/s
h (liquid level height)	2	mm
A_s (area in contact with liquid)	3.384e-3	m^2
c (damping coefficient)	0.0889	kg/s
μ (dynamic viscosity)	0.058	Ns/m^2
ν (kinematic viscosity)	4.77e-5	m^2/s
V_g (volume fraction of glycerin to water)	85	%

damping coefficient model is shown with a solid line. For the transfer function, the two lines follow fairly closely in the low frequency range, where the value is close to unity. Both the transfer function and phase shift lines vary slightly from the constant damping cases; this is due to the nonlinearity of the viscous damping system.

An initial simulation was performed using Simulink to provide insight into the frequency and step response of the modeled system.

The simulation was used to generate severall plots, the first is found in Figure 3.13, which is the response of the system to a step input. The time to peak is slightly greater than 0.5 s, while the system settles out quickly in less than 1.5 s.

The frequency response plot from the simulation is found in Figure 3.14, which is the time varying response of the model to a sinusoidal forcing function. The transient behavior decays rapidly, within less than 2 s, then the driving force dominates.

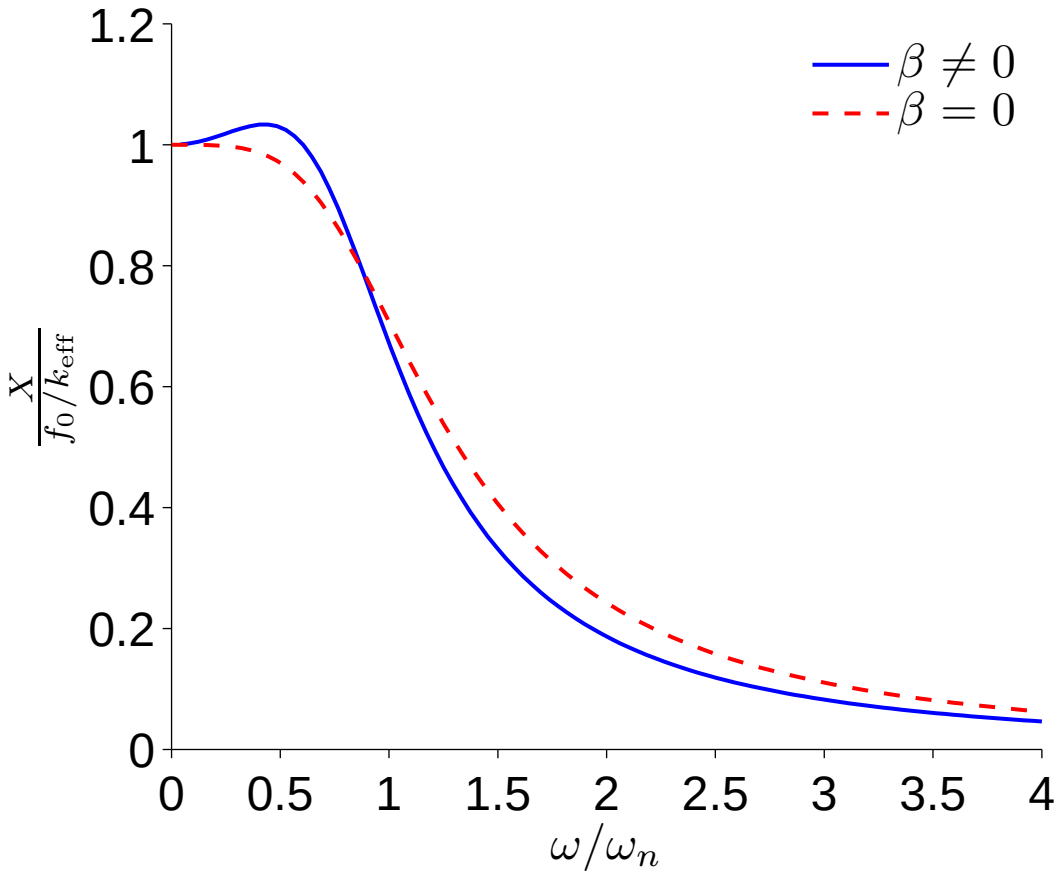

Figure 3.11. Transfer function for a range of frequency ratios, ω/ω_n, for the cases of β=0, and $\beta \neq$0, where the damping ratios $\zeta = 0.707$, and $\zeta_0 = 0.717$, respectively.

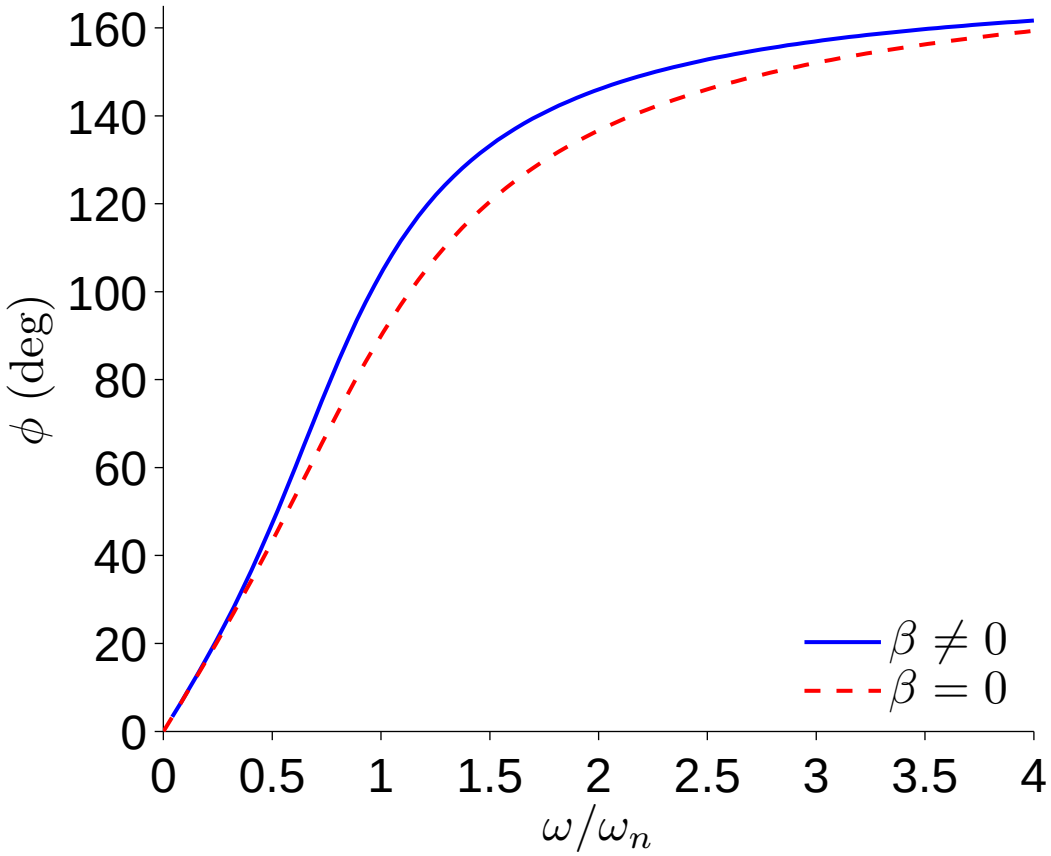

Figure 3.12. Phase shift for a range of frequency ratios, ω/ω_n, for the cases of β=0, and $\beta \neq$0, where the damping ratios are $\zeta = 0.707$, and $\zeta_0 = 0.717$, respectively.

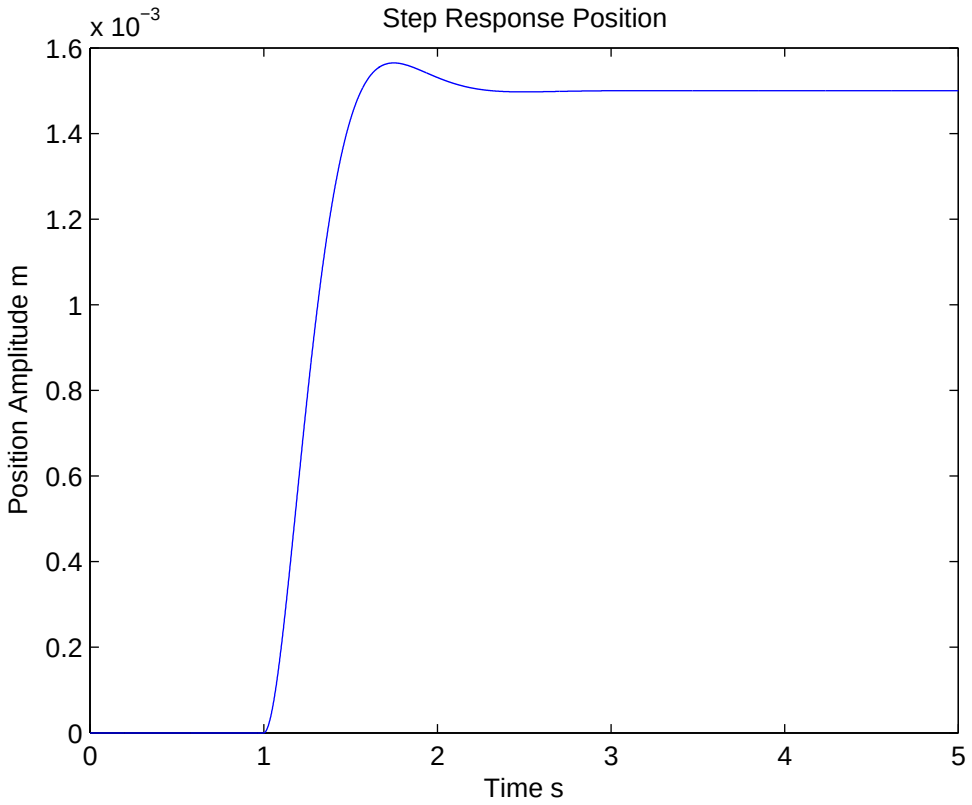

Figure 3.13. Plot showing the response to a step input. Position amplitude is on the vertical axis and is measured in m. The time in s is on the horizontal axis.

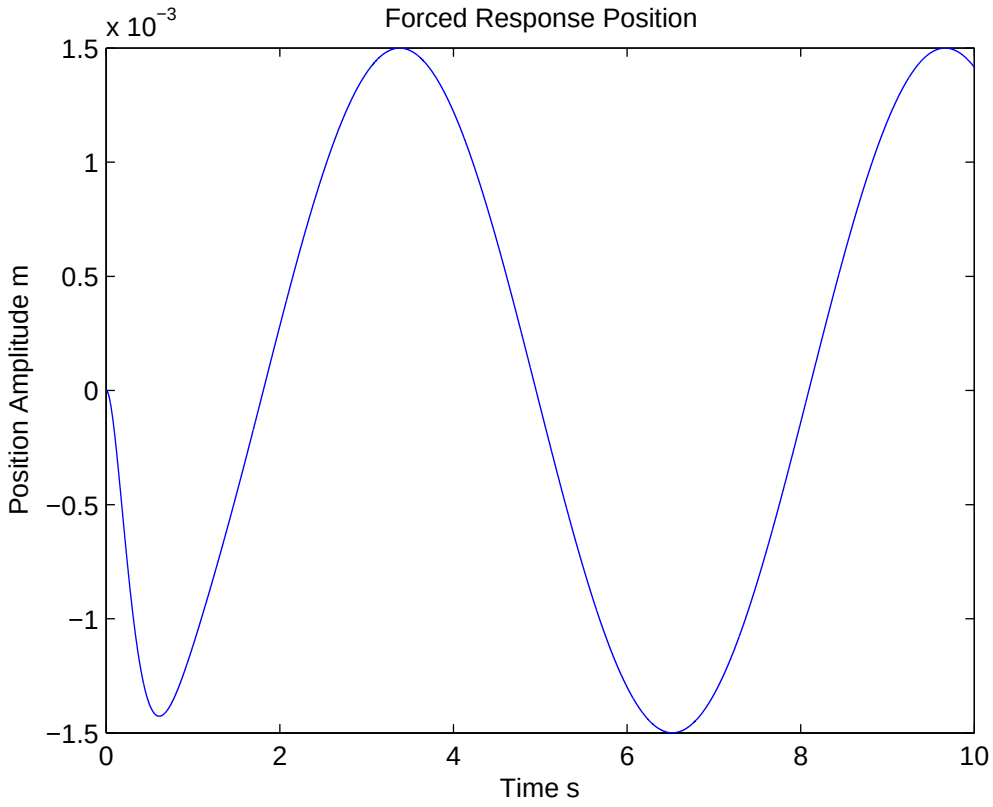

Figure 3.14. Plot showing the forced response of the system to a sinusoidal input. The position amplitude in m is on the vertical axis. The time in s is on the horizontal axis.

CHAPTER 4

PROTOTYPE

Based on the models developed in the previous chapter, a physical prototype of the system was constructed. This chapter outlines the iterative design process, including a description of each component of the system. Design decisions are justified and lessons learned are discussed.

4.1 Mechanical Design

4.1.1 Solid Model

Before the main construction of the physical prototype, the entire sensor unit was modeled using SolidWorks. Figures 4.1 and 4.2 show a top and rear view of the 3-D final drag plate design, with key components labeled. The final drag plate design consists of: a floating disk, micro springs attached to the center of the floating disk on one end and a swivel connected to an ultra-fine adjustment screw on the other, this provides fine adjustment capabilities for the spring, base plate that provides a level surface for the liquid, reservoir that allows convenient filling of the base plate, housing that contains all components, electrical connectors that allow plug-in access to the electronics, adjustable PSD platform that vertically adjusts, pinion and bevel gears that convert rotational movement of a shaft into vertical movement of the PSD platfrom.

4.1.2 Floating Disk Design

To achieve a high natural frequency, and thus a high frequency response, the mass of the disk must be as low as possible; see (3.31). Also, to float, the disk must be more buoyant than the damping liquid and non absorbing. To satisfy these criterion,

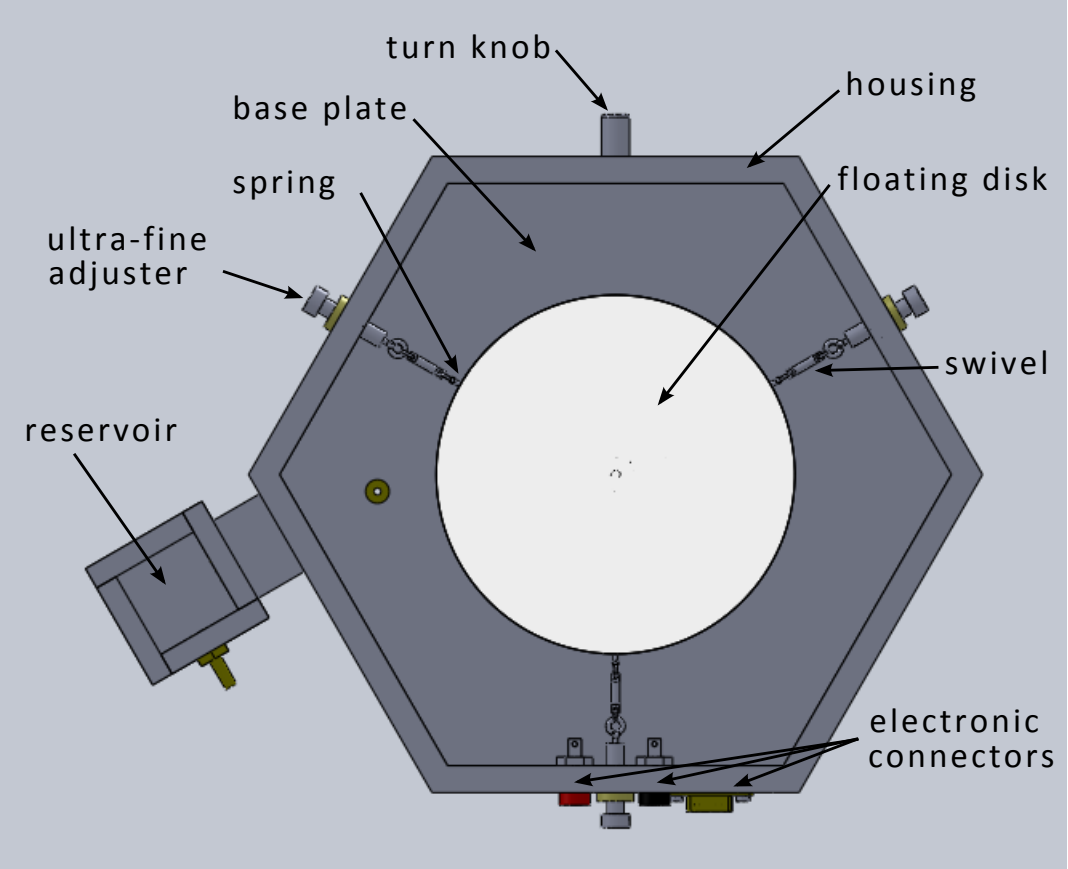

Figure 4.1. Final design of the drag plate as viewed from the top. Several key components are labeled for clarity. Drawn to scale.

expanded polystyrene (EPS) foam, with a density of one pound per cubic foot, was selected as the disk material. Despite the low density, EPS foam can be machined on a mill, if done with care. The final design of the disk is shown in Figure 4.3. There are three raceways that provide clearance for the three springs. An index tab and platform in the center of the disk ensures proper alignment of the VCSEL and spring assembly. The entire center area of the disk is raised to accommodate the electronics, including the PSD. The remaining outer ring of material provides the floating surface in contact with the liquid.

A lid comprised of the same EPS foam as the disk was designed to cover the rest of the housing as shown in Figure 4.4. The lid design features a center hole that is 3 mm

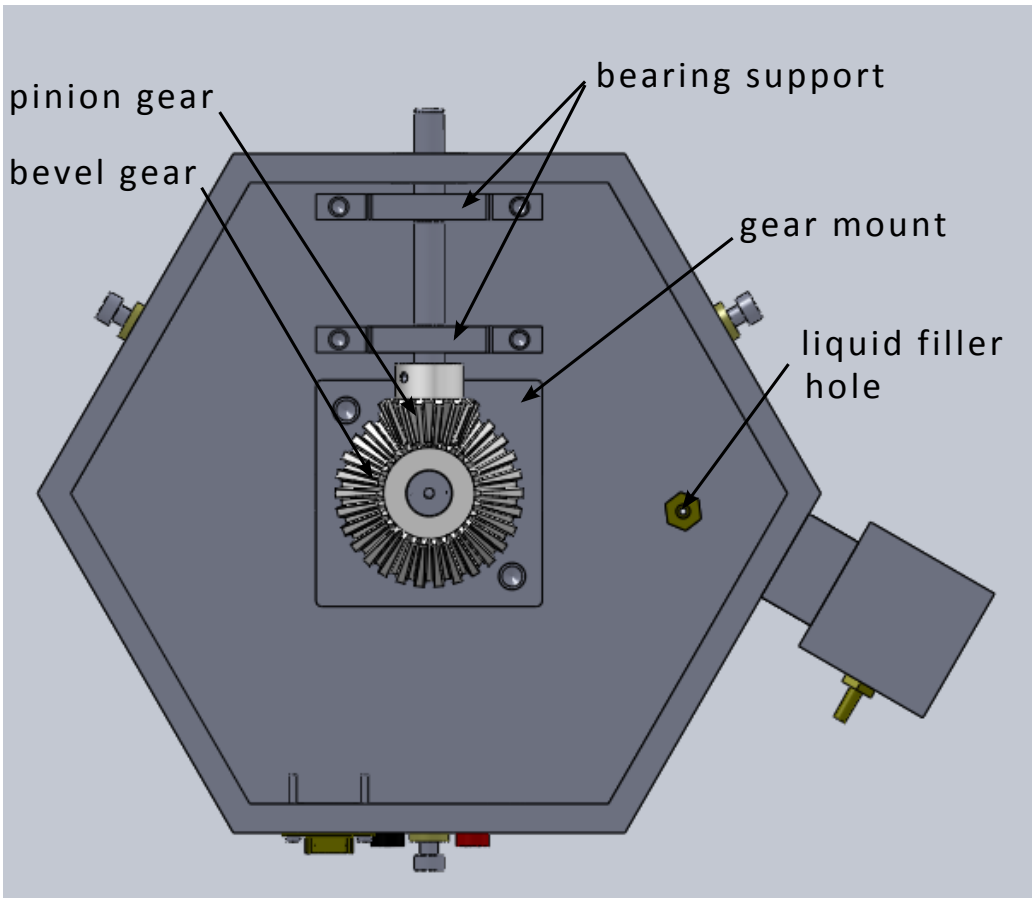

Figure 4.2. Final design of the drag plate as viewed from the rear. Several key components are labeled for clarity. Drawn to scale.

larger than the diameter of the disk to accommodate the required 1.5 mm gap. The lid fits snugly over the housing, providing an insulated and protected environment inside the device where the electronics and optics are contained. Both the lid and disk were machined by FoamLinx, a company in California that works with all types of foam.

4.1.3 Spring Design

From section 3.2.1, it was determined that springs having individual spring constants of $k = 0.3351$ N/m would yield the desired performance. Custom springs were designed to achieve this spring constant using the following spring design equation

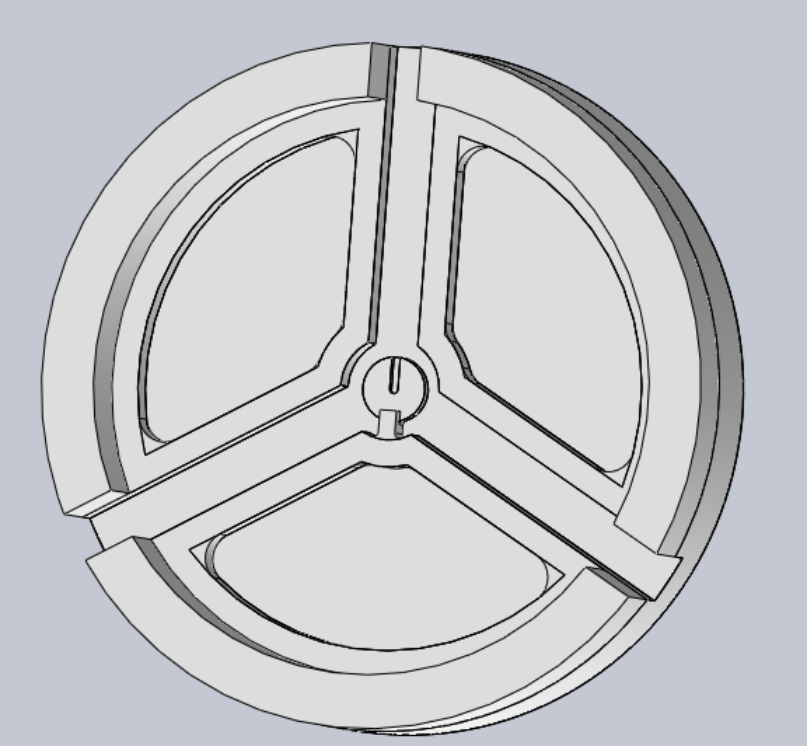

Figure 4.3. Final design of the floating disk as viewed from the underside. The diameter of the disk is 127 mm (5 in). Drawn to scale.

$$k = \frac{G\,d^4}{8\,n\,D^3} \quad , \tag{4.1}$$

where k is the spring constant, G is the modulus of rigidity of the wire, d is the wire diameter, n is the number of coils and D is the spring mean diameter, which is defined as the outer diameter of the spring minus the wire diameter. It is also important to note that tension springs have an initial tension force, which must be overcome before the spring can stretch. Once the initial tension force is overcome, the spring behaves linearly.

Using (4.1) and working in conjunction with Acxess Spring, a spring manufacturer in California, a micro spring with the following characteristics was selected: $G = 98 \times 10^9$ Pa, $d = 0.099$ mm, $n = 487$ coils, $D = 1.93$ mm. Because 487 coils were required, the overall length of the individual spring is approximately 2 inches. This

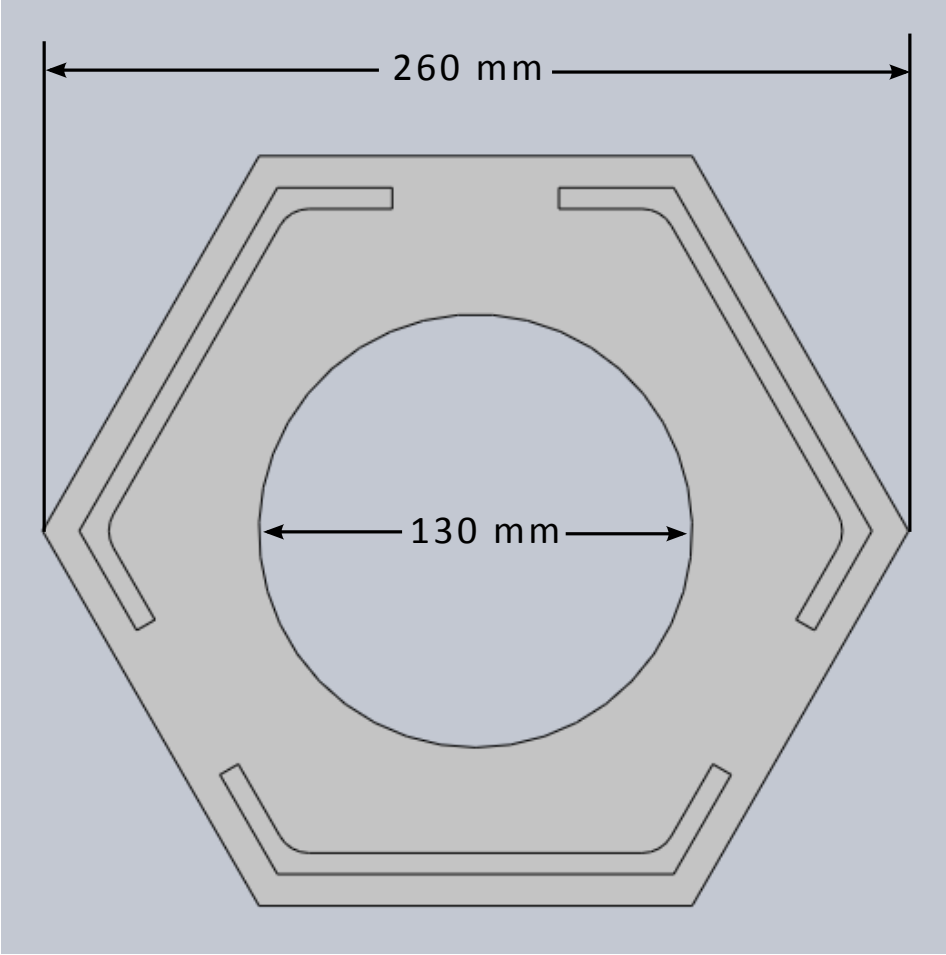

Figure 4.4. Final design of the foam lid as viewed from the underside. The diameter of the center cutout is 130 mm. Drawn to scale.

length was then used to determine the necessary dimensions of the housing unit.

An ultra-fine adjustment screw (thread pitch m6 x 0.25) with a swivel, is attached to the end of each spring to provide a means of manually setting the amount of pretension as well as centering the disk. Figure 4.5 shows the final design for the spring system including the swivels and ultra-fine adjustment screws. Note, the center hub with index slot allows the spring assembly to be centered accurately with the disk.

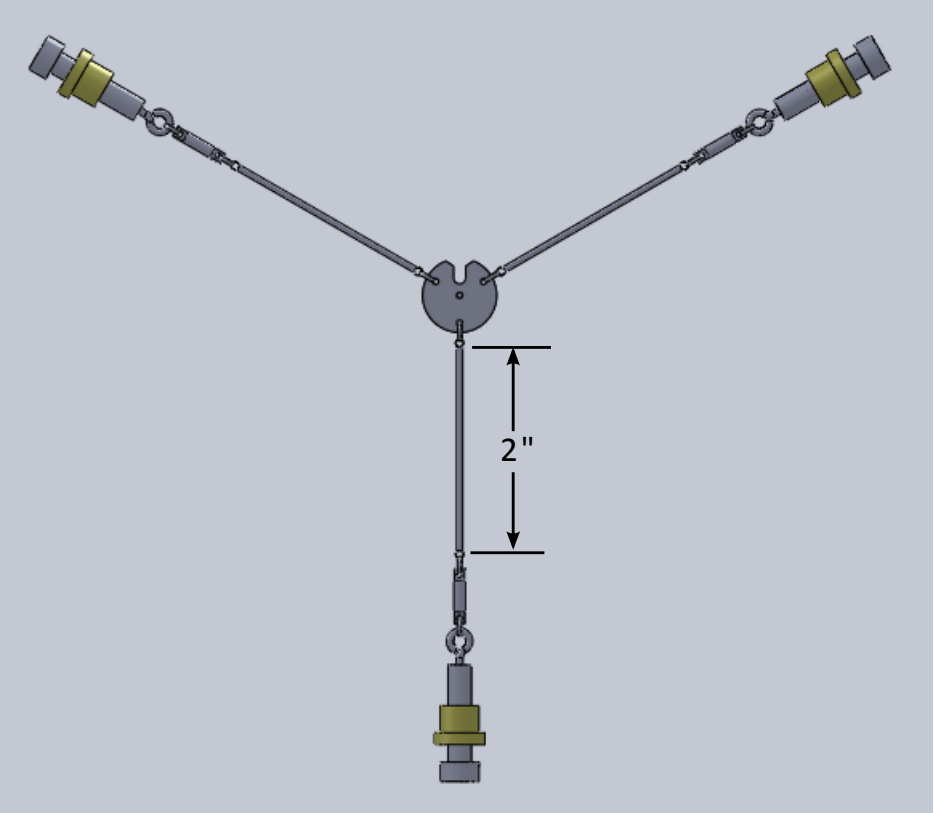

Figure 4.5. Final design of the spring assembly. Three extension springs are attached to the center hub at one end and a swivel with ultra-fine adjustment screw at the other. Drawn to scale.

4.1.4 Viscous Damping

The magnitude of the viscous damping force depends on the height and viscosity of the liquid used to support the disk. As discussed in section 3.2.2, the height of the liquid was chosen to be 2 mm. The base plate, shown in Figure 4.6, was designed with this dimension in mind. A small liquid reservoir connected to the side of the base plate allows a convenient means to adjust the liquid level in the base plate. Liquid in the reservoir is routed through tubing underneath the base plate to a filler hole in the bottom of the base plate.

When liquid is added or removed from the reservoir, the liquid level in the base plate adjusts accordingly, since both are exposed to atmospheric pressure. Also,

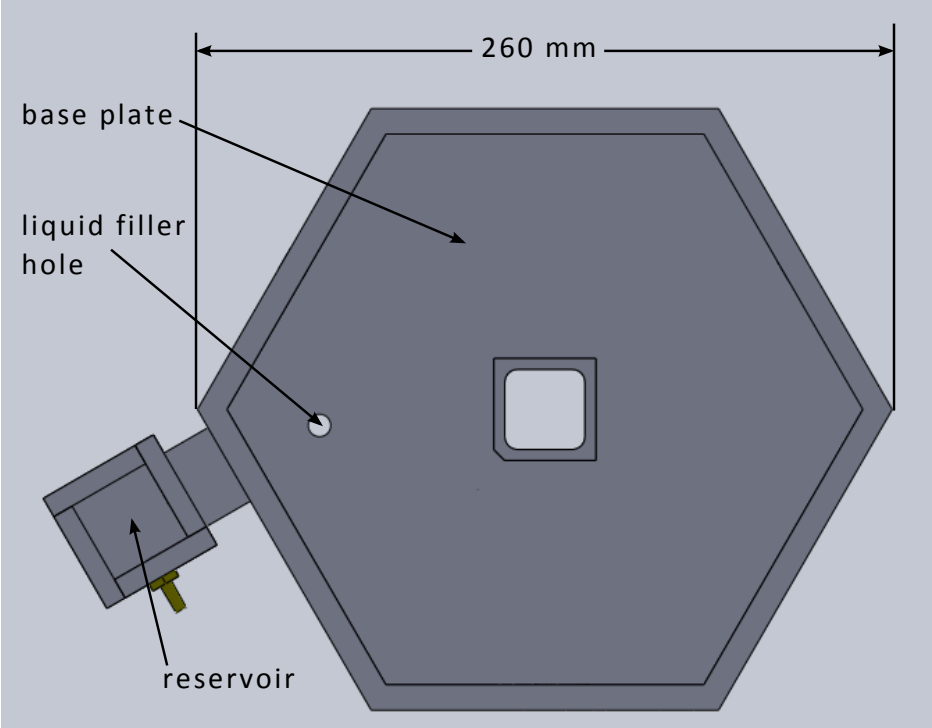

Figure 4.6. Base unit with liquid reservoir attached. Tubing underneath the base plate connects the fluid in the reservoir to the base plate through the liquid filler hole indicated. Drawn to scale.

since the surface area of the base plate is much greater than the reservoir surface area, the liquid level in the base plate rises slowly while the reservoir is being filled, thus allowing for a fine adjustment of the liquid height. In the current design, a syringe is used to manually control the liquid level in the reservoir. The liquid was chosen to be an 85% glycerin to water solution, measured by volume. According to the viscous damping model of section 3.2.2, this should yield a damping coefficient of 0.707, giving the desired response.

4.1.5 PSD Platform Mechanism

With the VCSEL attached to the center of the disk, and the liquid level set to the proper height, a seperate mechanism was needed to vertically move the PSD into alignment with the VCSEL. This mechanism also allowed the PSD to be lowered

during transport and while filling the base plate to avoid potential damage to the active area. The maximum gap between the VCSEL and PSD was determined to be L=1.2 mm, as shown in Figure 4.7. The main criterion for selecting L is that the spot size from the VCSEL must not be larger than the active area of the PSD, in order for the PSD to accurately track the centroid of the light beam. Given the manufacturer specified divergence angle of 6°, and an initial output beam diameter of 0.75 mm, the maximum gap height is L=1.2 mm. This generates an incident spot size of 1 mm diameter, ensuring that the light does not pass the active area of the PSD. The PSD platform mechanism, shown in Figure 4.8, was developed to convert the rotating movement of a horizontal shaft, which protrudes from the side of the housing, into vertical movement, using a finely threaded rod. A bevel gear combination, with a 2:1 gear ratio, provides the transmission. The pinion shaft is supported on two bearings, and held in place using e-clips. The pinion gear is held onto the shaft with a tension pin to form a rigid mechanical connection between the gear and shaft.

The bevel gear is attached to a gear mount block that holds all of the parts necessary for the vertical traverse. The bevel gear slides into a bronze bushing, which acts as a bearing and allows the gear to spin. The entire assembly is held in place

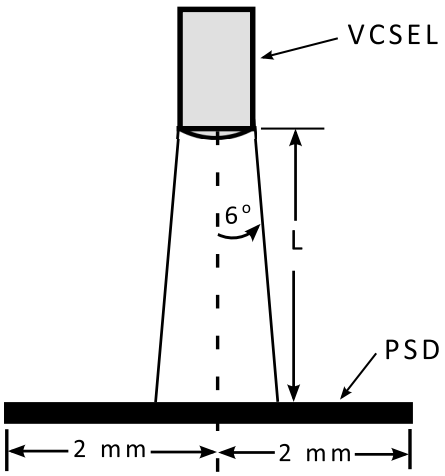

Figure 4.7. Diagram of beam divergence as the laser light impinges on the PSD.

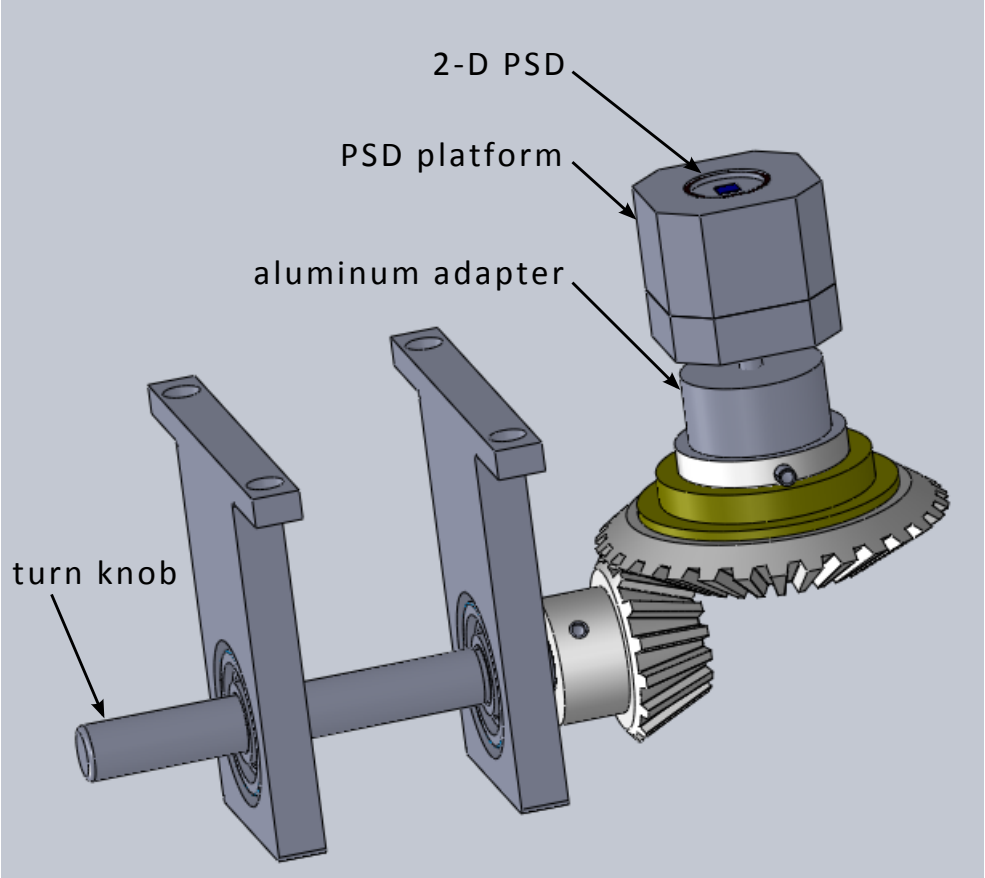

Figure 4.8. Final design of the PSD platform mechanism to vertically raise and lower the PSD platform via a turn knob.

with a tension pin that supports and stops the gear from exiting the bushing.

A cylindrical aluminum adapter was designed with threads at one end to accomodate a finely threaded screw rigidly attached to the PSD platform. The adapter slides through a clearance hole in the bevel gear and is rigidly attached to the bevel gear using a tension pin. As the bevel gear spins, the screw moves up and down with the PSD platform. This generates the vertical movement for the PSD, since the platform housing the PSD is constrained to move only in the vertical direction. One full revolution of the pinion shaft generates a vertical PSD displacement of 0.35 mm.

4.1.6 Electronics

The electronic circuitry needed to operate the sensor is relatively simple. The main components consist of a power supply for the laser and a power supply/signal processing board for the PSD. A circuit board was purchased with the 2-D PSD to ensure compatibility. The power supply for the VCSEL requires the same circuitry as a light emitting diode (LED) and was custom built. The LED power circuit consists of a voltage source, a resistor and the LED (or in this case, the VCSEL). A schematic of a simple LED circuit is given in Figure 4.9.

To calculate the needed resistor value, the following equation was used

$$R = \frac{V_s - V_{led}}{I} \ , \tag{4.2}$$

where R is the value of the resistor, V_s is the source voltage, V_{led} is the voltage drop across the led as given by the manufacturer and I is the current passing through the circuit. Given the values of $V_s = 3$ V, $V_{led} = 2.2$ V and $I = 5$ mV (as specified on the VCSEL data sheet), the value of R is calculated to be 160 Ω.

The most difficult part of the electronic circuit in the present design is connecting the leads of the power supply, located outside the housing, to the VCSEL located at the center of the floating disk. Several methods were explored before a solution

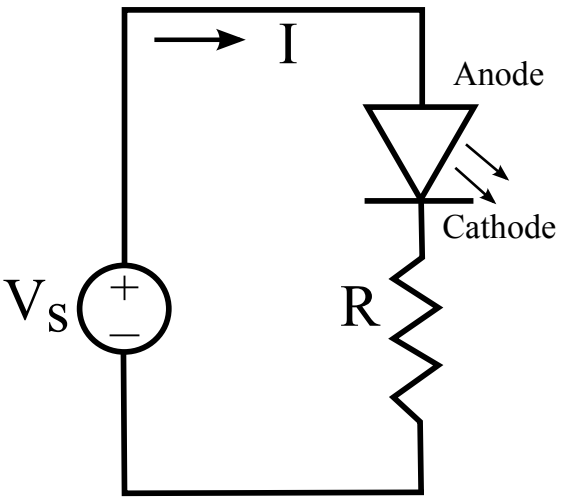

Figure 4.9. Schematic of LED power circuit.

was found. The first idea was to use two of the springs to transmit the power to the VCSEL. It became evident, however, that this would not work, since the spring coils were so close together. If two spring coils touched while the light source was powered, the system could short.

Another method was to use conductive rubber to replace the springs. The conductive rubber would serve two purposes: (i) to power the VCSEL and (ii) produce the necessary spring constant for the restoring force. The equation for the stiffness of rubber, using Hooke's law, is given by

$$k_{rubber} = \frac{E\,A}{L} \quad , \tag{4.3}$$

where k_{rubber} is the stiffness of the rubber, E is the modulus of elasticity, A is the cross sectional area of the rubber piece and L is the initial starting length of the rubber. Note, rubber only follows a linear relationship for small displacements; beyond the linear regime, (4.3) no longer remains valid. Based on (4.3), using a representative experimentally determined modulus of gum rubber (rubber bands) $E = 1.5$ MPa, cross sectional area $A = 8e^{-7}$ m^2 and $k_{rubber} = 0.3351$ N/m, the initial length would have to be over 3.5 m to achieve the necessary spring constant of the system. This lies well outside the constraints of the physical domain.

The final method investigated (and the one adopted) was to use a 0.003 inch diameter enamel wire from a relay to transmit the power between the external supply and the VCSEL. The enamel wire has several benefits. First, the thin enamel coating provides electrical insulation. Second, it does not add excessive stiffness to the overall system. Third, the wire has the capacity to carry the needed current (i.e., the relay was rated at 1 A, while the VCSEL only requires current in the mA range). Two banana jacks were added to the base unit to provide plug-in access to power the VCSEL. Also, a DB9 connector was added to the housing,to provide a convenient means of connecting the output from the PSD to the signal processing board. This makes the sensor a self contained unit.

4.1.7 Overall Assembly

As construction of the physical prototype progressed, several lessons were learned along the way. The main lesson involved communication with the manufacturing facility that was paid to machine the individual parts. To ensure that all features are represented accurately, the solid model needs to have each part called out exactly as desired, including, tapped holes, screw clearance holes, slotted holes, pipe thread taps and dowel pin press and slip fit holes.

It is also important to have the solid models finalized prior to contacting the machine shop for a quote. Confusion arose in the present project because modifications were made to the drawings after the initial quote was generated. The machine shop ended up using the first set of drawings, which posed some challenges during assembly. Therefore, communication between the machine shop and engineer is crucial prior to requesting a quote to ensure that the parts are actually machinable and that the tolerances specified are attainable. A preliminary visit to the machine shop is useful to check beforehand if the machinist can foresee any problems. This also helps build a good rapport with the machinist and the facility.

Another important lesson learned was designing for manufacturabilty and assembly. Throughout the design process, each part was subject to an assembly check. If the part could not be physically assembled, it was redesigned. Even still, some components can only be assembled one way. For complete assembly instructions, see Appendix D.

4.2 Calibration Results

With all of the parts and assemblies installed, the shear stress sensor is now ready for testing and calibration. A static calibration test is performed on the sensor to determine the accuracy of the effective spring constant model as outlined in section 3.2.1. The purpose of this test is to see how closely the physical system behaves when compared to the mathematical predictions.

The setup for the static calibration test consists of a 100 mm cardstock disk with

rays drawn on the surface, each starting at the centroid and pointing radially outward toward the edge in 15° increments. Note, the calibration was performed using 30° increments rather than every 15°. This captures the major points of interest according to the model, which are the points along the centerline, as well as the highest and lowest expected values. A tack was used to attach the cardstock disk to the centroid of the floating foam disk. The tack served as an attachment point to the floating disk centroid for a 12 μm diameter tungsten wire connected to an aluminum foil mass that hung from a 0.023 in diameter ground rod. An illustration of the calibration setup can be found in Figure 4.10.

The procedure to perform the static calibration test starts with recording the equilibrium voltage output from the 2-D PSD, then hanging a mass from the ground rod. The displaced voltage is then recorded and the mass is lifted from the free-hang position and moved to the next desired incremental angle. The process then repeats itself until all the angles have been recorded. Since the PSD outputs both an x and y voltage, an angle from equilibrium is calculated along with the corresponding magnitude. This is done using the specifications for the PSD given from the manufacturer to convert the output voltage to displacement. The specifications state that if the sum voltage output, V_{sum}, is between $1 < V_{sum} < 5$ volts, the full-scale PSD

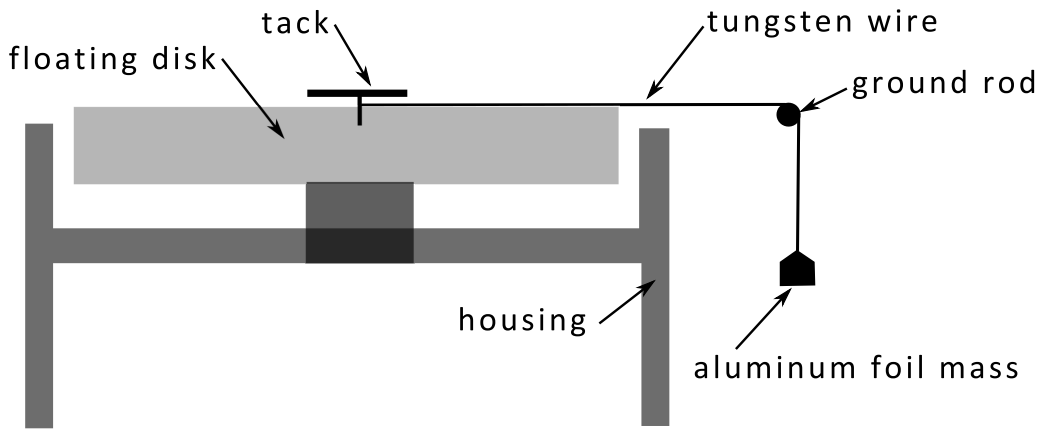

Figure 4.10. Illustration of the static calibration setup used with the floating disk.

voltage, V_{fs}, will be linear and range from $\pm 10 < V_{fs} < \pm 10.5$ volts. Taking the value of $V_{fs} = \pm 10$ volts, the displacement magnitudes at each angle were calculated. This data is presented in Figure 4.11, where two different masses were used, with the heavier yielding a force of 7.35e-4 N, and the lighter 6.47e-4 N. The aluminum foil masses were measrured using a mass-balance with a readability of 0.001 g.

To compare the effective spring constant model with the data obtained from Figure 4.11, the measured data need be of the form, k_{eff}/k. This is accomplished using the definition for the effective spring constant, $F = r_0\, k_{eff}$, then dividing both sides by the individual spring constant k. Solving for the spring constant ratio, k_{eff}/k, results in

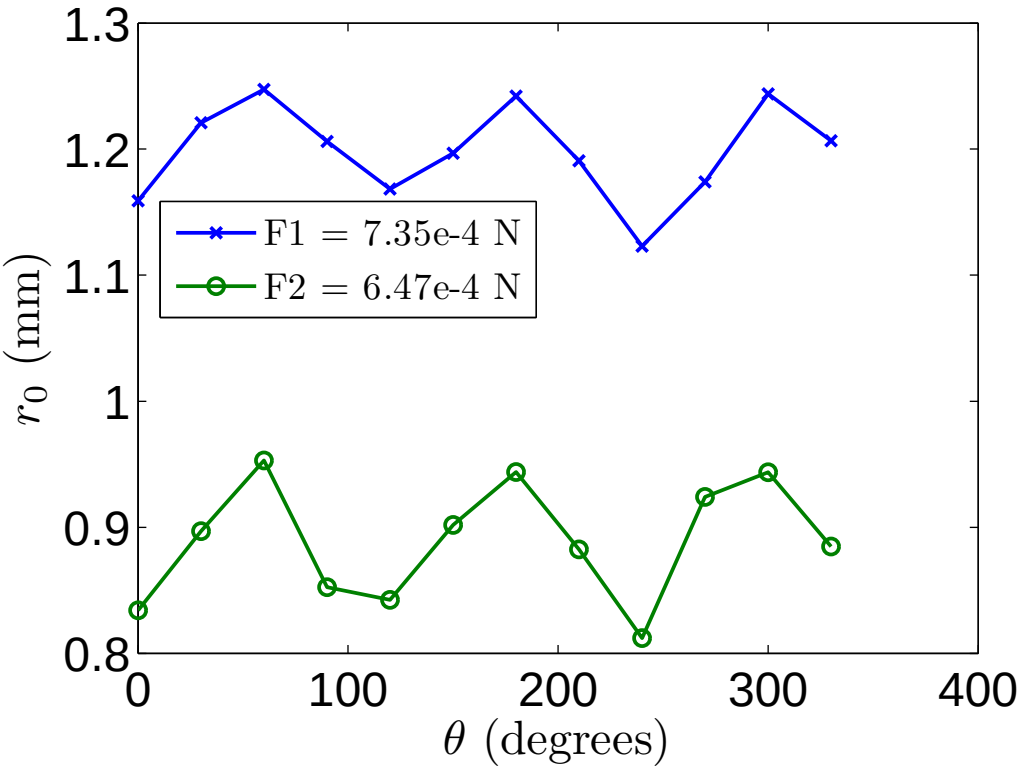

Figure 4.11. Disk centroid displacement magnitude, r_0, as determined from the static calibration test for two different weights, F1 = 7.35e-4 N, F2 = 6.47e-4 N.

$$\frac{k_{eff}}{k} = \frac{F}{r_0\, k} \ , \tag{4.4}$$

where F in this case is the known force generated by the aluminum foil mass, and r_0 is the measured displacement magnitude. Using the before mentioned values, the calculated k_{eff}/k for both masses is found in Figure 4.12, with the predicted curves from the model, for average r_0 values of 1.2 and 0.9 mm corresponding to the average measured values, included for reference. The average value of k_{eff}/k for a force of 7.35e-4 N was calculated to be 1.832. Whereas, the average value predicted by the model is 1.803. This gives a difference of 1.5%. Also, the maximum variation in the measured values is 5.3%. However, the average value of k_{eff}/k for a force of 6.47e-4

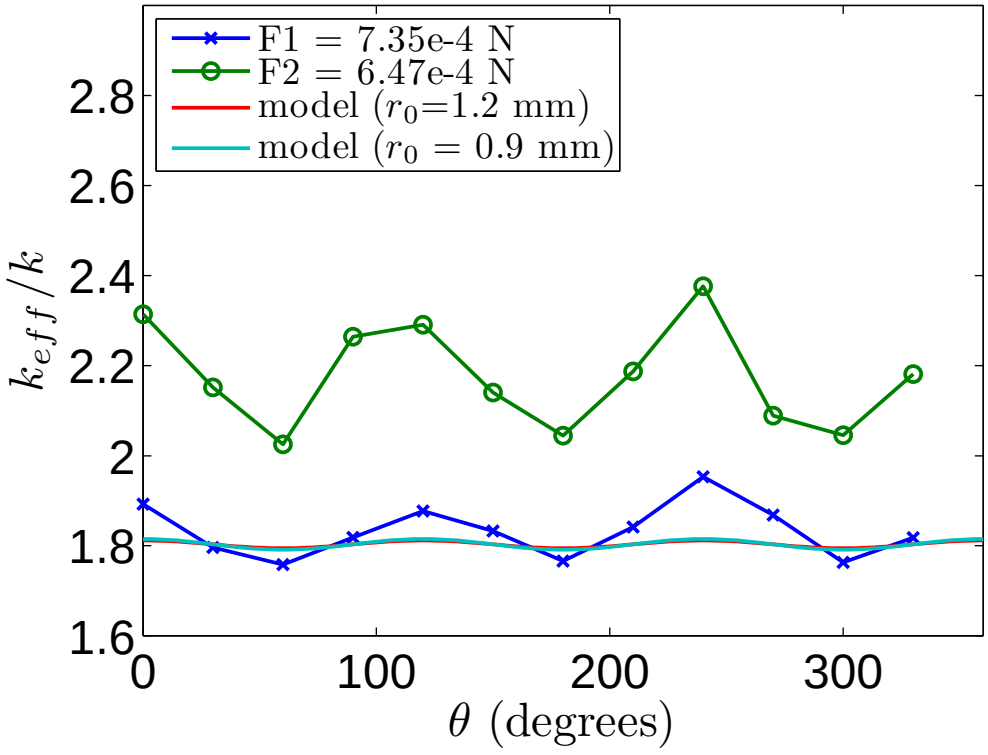

Figure 4.12. Spring constant ratio, k_{eff}/k, as determined from the static calibration test for two different weights, F1 = 7.35e-4 N, F2 = 6.47e-4 N. For comparison, the curves from the mathematical model are included for $r_0 = 1.2$ mm and $r_0 = 0.9$ mm.

N was calculated to be 2.181, with a maximum variation of 9.1%. The average value predicted by the model for a force of 6.47e-4 N is 1.803, this gives a difference of 20.8% when compared with the measured value. A possible explanation for this large difference is that for smaller forces, not all of the force transfers to move the disk centroid. This was noted during the calibration, despite the efforts to minimize friction with the ground rod and the use of a very small diameter wire.

CHAPTER 5

SUMMARY

The main basis for this current study comes from Sadr and Klewicki (2000), who used a floating element device for use in boundary layer flow over a salt playa. The device uses the direct measurement approach, since it is placed flush with the surface to be measured. The direct measurement device was chosen by Sadr and Klewicki for several reasons over the current indirect methods. The challenges for their design stem from the harsh environmental conditions that exist in the salt playa. Some expected conditions include solar radiation, humidity variations, airborne contaminants and a wind speed and direction, which are uncontrolled.

Based on these extreme conditions, a delicate measurement device such as MEMS would be inaccurate. Also, the expected shear stress to be measured is very small, $\tau_w \cong 3\text{x}10^{-3}Pa$ (Klewicki *et al.*, 1995). Their unit was around 2.1 m in diameter and included an aluminum base that was welded together. The overall design was cumbersome to transport and install due to its size. Also, since their device was so large it could only provide an average value of surface shear stress.

This project involves using the previous idea of a floating disk plate to directly measure the shear stress on a surface and make it smaller, while still maintaining accurate results. There are many advantages to having a smaller design. Some of these include: ease of implementation, reduced cost, portability, a higher expected frequency response, and the ability to deploy large arrays of these units to achieve spatial distribution and capture heterogenous effects.

The shear stress sensor consists of a 5 inch circular expanded polystyrene (EPS) foam disk, which is attached to a housing using three springs each at 120^o from each

other. The springs are pre-stretched so they will always apply a net tension force on the disk. Also, the disk floats on a pool of liquid, which provides the system damping. As the disk moves, it causes the springs to displace from equilibrium. This sets the oscillation in motion, which is damped out by the viscous force that is present between the disk and the liquid. A position sensitve detector (PSD) is placed in a platform under the disk, which is used to record the position of the disk. A vertical cavity surface emitting laser is placed in the centroid of the disk, which shines onto the PSD below. The output is given as a voltage that is based on the relative position of the light source. With the position of the disk centroid known, the spring displacement is calculated, which for a linear system directly correlates to the shear stress on the disk.

The shear stress sensor was developed with the use of several individual mathematical models, which were then combined to create the overall equation of motion for the disk. There were three individual parts used to model the entire system. The first was the determination of an effective spring constant, which was resolved along the direction of motion. The second was the viscous damping model, which was used to find the needed damping shear force. The third is the forcing that is applied to the disk by the moving air. With all of these individual models determined, the assembly and solving of the entire equation of motion was presented.

The spring constant model, is used to take the individual spring constants k, and combine them in such a way that they act as an effective spring constant in the direction of the displacement vector r_0. This was done using a vector summation approach. The ratio of effective spring constant to individual spring constant k_{eff}/k was determined to have an average value of 1.575. The value for k_{eff} was determined from the maximum expected force ($7.917 \times 10^{-4}\ N$) and the maximum desired displacement of the disk ($1.5\ mm$), which yields a value of $0.5278\ N/m$. This value was then used to calculate the needed individual spring constants, which were $0.3351\ N/m$. Also, the assumption was made that the spring force acts through the pinned connection on the housing. Since the springs are pre-tensioned, the force always acts

in the direction away from the center of the disk. However, the displacement vector always points toward the equilibrium position.

The viscous damping model that was developed is based on Couette flow. This type of flow occurs between two parallel plates that are both infinite, with a finite gap distance between them. In this Couette flow model the lower plate is stationary, while the upper is oscillating with a sinusoidal input. This makes the problem unsteady, since the velocity of the upper disk changes with time. The purpose for developing this model was to determine the function for the damping shear force and the needed approximate glycerin content, which gives the system a damping ratio of 0.707. An equation for the damping shear force was determined and the approximate value of glycerin content, which yields the necessary damping coefficient was found to be around 85%. The corresponding values for viscosity are dynamic $\mu = 0.058\ Ns/m^2$, and kinematic $\nu = 4.77 \times 10^{-5}\ m^2/s$. These values were then used in the overall equation of motion for the disk.

The actual forcing function from the air blowing across the top of the disk has completely random frequencies and amplitudes, which may be modeled as an infinite series of sines and cosines. The solution of which, for a linear model, would simply be the sum of the individual solutions. For this reason, the model focused on a single sinousoidal forcing function, with a given forcing frequency and amplitude. To ensure the system would behave linearly, a low forcing frequency was chosen, which was 1 rad/s, along with the forcing amplitude of $7.917 \times 10^{-4}\ N$. Also, the response of the system to a step input was shown, which gave the basic parameters of the system, including settling time, rise time, and percent overshoot.

All of the individual models were incorporated into the overall equation of motion, by taking the general form for a mass-spring-damper system with forcing, and then substituting in the equivalent terms. The transfer function and the phase shift of the equation of motion was solved, by taking the sine and cosine terms seperately. These functions were then used to determine the behavior of the system with increasing forcing frequencies. All of the parameters of the mathematical model that have been

discussed in this summary are found in Table 5.1 for easy reference, which is located at the end of this section.

Before the main construction of the physical prototype, the entire sensor unit was modeled using SolidWorks. When any changes needed to be made, they were first performed on the solid model, which made the design process easier. After any physical parts were added to the prototype, they were subsequently modeled and placed on the solid unit, thus making the solid model as complete as possible. The prototype consists of several subassemblies, which are connected to a base housing to make up the entire sensor unit. These subassemblies are the center post vertical adjustment, the disk and springs, the reservoir, and the electronics.

The center post vertical adjustment uses a bevel and pinion gear to convert the rotation of a horizontal shaft into vertical movement. This is done through the use of a screw that is rigidly attached to a center post, as the bevel gear rotates it extends or shortens the screw, thus creating vertical movement. The disk and springs are connected together with a center connector hub, which also incorporates a vertcal cavity surface emitting laser (VCSEL) diode at the center. The disk is machined from a single piece of 1 lb EPS foam, and has lowered side walls, which allow the disk

Table 5.1. Summary of model parameters

Parameter	Value	Unit
m (total mass)	0.0075	kg
k_{eff} (effective spring constant)	0.5278	N/m
k (individual spring constant	0.3351	N/m
x_{max} (maximum disk displacement)	1.5	mm
ζ (damping ratio)	0.707	-
c (damping coefficient)	0.0889	kg/s
g_c (glycerin content)	85	%
μ (dynamic viscosity)	0.058	Ns/m^2
ν (kinematic viscosity)	4.77e-5	m^2/s
ω_n (natural frequency)	8.38	rad/s
ω (forcing frequency)	1	rad/s
f_0 (forcing amplitude)	7.917e-4	N

to float on the liquid pool while keeping the electronics and springs dry. The springs are connected to the base housing on ultra-fine adjustment screws, which allow fine tuning of the pre-tension for each spring. The reservoir is attached to the side of the housing, and is connected to the pool of liquid via a tube. This allows for easy filling of the liquid level. The electronics for this sensor are quite simple. They consist of a PSD with an amplifier board, and a VCSEL with power supply circuitry. The PSD that is used for this sensor is an On-Trak Photonics 2-D doulateral type #2L4SP, with an active area of $4mm \times 4mm$. This PSD is placed in the center post, which provides vertical adjustment. Also, a compatible PSD amplifier was purchased at the same time. The VCSEL is powered through tiny wires, which are connected to a simple diode circuit using bananna jacks mounted to the outside of the housing.

5.1 Future Work

Although a succesful prototype of a direct shear stress measuremnet device was completed, all of the desired target conditions were not met. This leads to some improvements that can be made to the device. A few suggestions are given here.

The main improvement that can be made to this device is increasing the natural frequency. With a higher natural frequency, more turbelent fluctuations can be measured. There are two ways to increase the overall natural frequency of the system. The first is to decrease the the total mass of the system. It is difficult to decrease the total mass of the system, since the mass is dependent on many components; however, each component could be reviewed to minimize the mass contribution.

The second way to increase the natural frequency, is to increase the effective spring constant. This can be accomplished by continuing the optical advantage work, which has been presented in Chapter 2. With an optical advantage, the disk only moves a small amount, while the output beam on the position sensitive detector (PSD) moves farther. This allows the spring stiffness to be increased, since the needed disk movement is decreased.

The current sensor design incorporates a light source at the centroid of the disk,

which is powered by two tiny wires that are connected to the housing. This connection slightly impedes the free oscillation of the disk. If the spherical mirror was implemented, the need for a light source on the disk would be eliminated. This would allow the disk to be disconnected from any rigid attachment to the housing, thus creating a totally free environment for disk oscillations.

A closer look at the optics for the light source is necessary, which would help make the light well-behaved. A mechanical fixture could be implemented for the lenses to achieve proper alignment. Also, a different light source with a smaller initial beam output diameter, would allow the lenses to capture all of the incoming light. Another useful feature would be to have the light output in the visible spectrum, thus helping easily visualize the beam path.

In retrospect, some changes could be made to the physical prototype. All of the electrical connectors should be placed on the same outside panel, which would allow easier access for plug in. Also, a bronze bushing could be fabricated for the center post adjustment, which would eliminate the need for any type of lube as the center post slides vertically. The overall housing dimensions could be increased to allow for more pre-stretch of the springs. Finally, some other useful features could include a heat dissipation system to maintain the liquid level at a constant temperature, a syringe pump for liquid level height control and the design of an outer housing for use in placing the device flush with the surface.

APPENDIX A

DERIVATION OF OPTICAL ADVANTAGE EQUATIONS

The derivation for the optical gain that is produced when a light source is reflected off a spherical mirror is presented in this section. The present model assumes that the centroid of the mirror only moves in the x-direction and that the light beam has an infinitesimally small diameter, i.e. the divergence angle is zero. A schematic is illustrated in Figure A.1. Also, a brief description of each parameter is given in Table A.1.

The equilibrium position is defined such that the centroid of the light beam lies at $x = L_d$ when the centroid of the disc is located at $x = x_c$. The optical gain g is defined as the ratio of the displacement of the light beam on the PSD over the actual displacement of the mirror centroid, i.e., The equation is given by the following

$$g = \frac{|x_d - L_d|}{|x_c - L_c|} \ . \tag{A.1}$$

The goal of this model is to determine the maximum achievable gain as a function of the following input parameters: $y_c, \theta, r, L_c, L_d, L_s$. This will be achieved using geometric principles and ray tracing.

The equation line 1 describing the ray of light incident on the PSD is

$$line\,1: \quad y = m_1 x + b_1, \quad 0 \leq x \leq x_0 \tag{A.2}$$

where $m_1 = \tan\beta$. The value of b_1 is determined from the fact that the line must pass through $(x, y) = (x_0, y_0)$. The coordinates (x_0, y_0) represent the location at which the emitted light reflects off the circular mirror.This yields $b_1 = y_0 - x_0 \tan(\beta)$; thus,

$$line\,1: \quad y = y_0 + \tan(\beta)(x - x_0), \quad 0 \leq x \leq x_0. \tag{A.3}$$

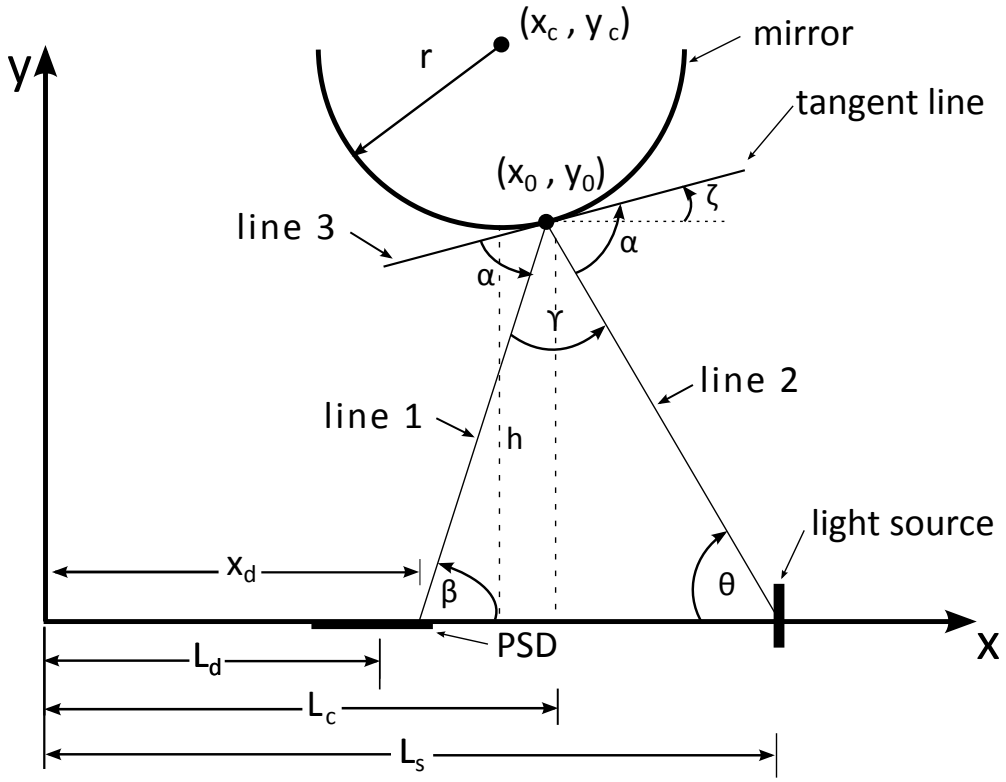

Figure A.1. Diagram of the optical gain system, side view through the center of the spherical mirror. The drawing illustrates the path of a single ray emitted from a light source at $x = L_s$, which subsequently reflects off the mirror at (x_0, y_0) and impinges on the detector at $x = x_d$.

The location of the incident light on the detector occurs at $x = x_d$ and $y = 0$. Plugging these conditions into (A.3) gives

$$x_d = x_0 - y_0 / \tan(\beta) \ . \tag{A.4}$$

The equation of line 2 describing the ray of light emitted from the light source is

$$line\,2: \quad y = m_2 x + b_2, \quad x_0 \le x \le L_s \ , \tag{A.5}$$

where $m_2 = -\tan(\theta)$. The value of b_2 is determined by the fact that the line must pass through the point $(x, y) = (L_s, 0)$. This yields $b_2 = L_s \tan(\theta)$. Thus,

$$line\,2: \quad y = \tan(\theta)(L_s - x), \quad x_0 \le x \le L_s \, . \tag{A.6}$$

Table A.1. Nomenclature for the optical gain model

Parameter	Description
L_c	x-location of the mirror centroid at equilibrium
L_d	x-location of the center of the detector
L_s	x-location of the light source
h	vertical distance between the x-axis and the bottom of the circular mirror ($h = y_c - r$)
r	radius of the mirror
x_c	horizontal coordinate of the mirror centroid
y_c	vertical coordinate of the mirror centroid
θ	angle of the emitted ray relative to the horizontal
x_d	horizontal coordinate of the light beam incident on the detector
x_0	horizontal coordinate where the emitted light intersects the periphery of the circular mirror
y_0	vertical coordinate where the emitted light intersects the periphery of the circular mirror

The equation describing the periphery of the mirror is

$$r^2 = (x - x_c)^2 + (y - y_c)^2 \ . \tag{A.7}$$

Plugging (x_0, y_0) into (A.6) and (A.7) gives a coupled set of equations for x_0 and y_0, which are

$$y_0 = \tan(\theta)(L_s - x_0) \ , \tag{A.8}$$

and

$$r^2 = (x_0 - x_c)^2 + (y_0 - y_c)^2. \tag{A.9}$$

Substituting (A.8) into (A.9) and solving for x_0 gives

$$x_0 = \frac{-(2\tan\theta(y_c - L_s\tan\theta) - 2x_c)}{2(1+\tan^2\theta)} \pm \frac{\sqrt{(2\tan\theta(y_c - L_s\tan\theta) - 2x_c)^2 - 4(1+\tan^2\theta)(x_c^2 + (y_c - L_s\tan\theta)^2 - r^2)}}{2(1+\tan^2\theta)}. \tag{A.10}$$

Similarly an expression for y_0 can be obtained by solving (A.6) for x_0 and substituting into (A.8) giving

$$y_0 = \frac{-(\frac{2(x_c-L_s)}{\tan\theta} - 2y_c) \pm \sqrt{(\frac{2(x_c-L_s)}{\tan\theta} - 2y_c)^2 - 4(1+\frac{1}{\tan^2\theta})(y_c^2 + (x_c-L_s)^2 - r^2)}}{2(1+\frac{1}{\tan^2\theta})} \tag{A.11}$$

The expressions in (A.10) and (A.11) give x_0 and y_0 as a function of x_c with input parameters: L_s, θ, y_c, and r.

To complete the analysis, an expression for β as a function of x_c is required. This relies on the use of Snell's law, which states that the angle of the reflected light with respect to the tangent line must equal the angle of the incident light. Therefore

$$\gamma = 180 - 2\alpha, \tag{A.12}$$

and subsequently

$$\beta = 180 - \gamma - \theta = 180 - (180 - 2\alpha) - \theta = 2\alpha - \theta \ . \tag{A.13}$$

Note,

$$\alpha = \theta + \zeta \ , \tag{A.14}$$

where $\tan\zeta$ represents the slope of the tangent line at (x_0, y_0), i.e.

$$line\ 3: \quad \tan\zeta = \left.\frac{dy}{dx}\right|_{(x_0,y_0)} . \tag{A.15}$$

From (A.7),

$$y = y_c - \sqrt{r^2 - (x-x_c)^2}, \quad y \le y_c \ , \tag{A.16}$$

for the lower half of the circle. The derivative with respect to x is

$$\frac{dy}{dx} = \frac{2x - 2x_c}{\sqrt{2(r^2 - (x-x_c)^2)}}. \tag{A.17}$$

Evaluting (A.17) at $x = x_0$ and substituting into (A.15) gives

$$\zeta = \arctan\left(\frac{2(x_0 - x_c)}{\sqrt{2(r^2 - (x_0 - x_c)^2)}}\right). \tag{A.18}$$

Therefore,

$$\beta = \theta + 2\arctan\left(\frac{2(x_0 - x_c)}{\sqrt{2(r^2 - (x_0 - x_c)^2)}}\right). \tag{A.19}$$

Using equations (A.1), (A.4), (A.10), (A.11), and (A.19), one can directly evaluate the optical gain as a function of disk displacement x_c, given specified values for the following design parameters: L_d, L_s, L_c, θ, r, and y_c.

If the origin of the coordinate system is moved to the centroid of the circular mirror, the number of design parameters can be reduced. In the new coordinate system $L_c = 0, L_s = d$, and $L_d = -d$, where d is the distance from the centroid of the mirror to the light source and the PSD while in equilibrium. Additionally, specifying h, the minimum height of the mirror surface above the horizontal plane containing the light source and PSD, sets the emitted angle

$$\theta = \arctan\left(h/d\right) . \tag{A.20}$$

The optical gain now becomes

$$g = \frac{|\tilde{x}_d|}{|x_c|} \ , \tag{A.21}$$

where $\tilde{x}_d = |x_d| - d$ and denotes the displacement of the light beam relative to the center of the PSD. Using this simplification the relevant design parameters are: h_c, r and θ, where $h_c = y_c$ the vertical height of the mirror center. Therefore, the functional relationship for the optical gain can be expressed as

$$g = f(h_c, r, \theta) \ . \tag{A.22}$$

Figure A.2 illustrates the system in the equilibrium position.

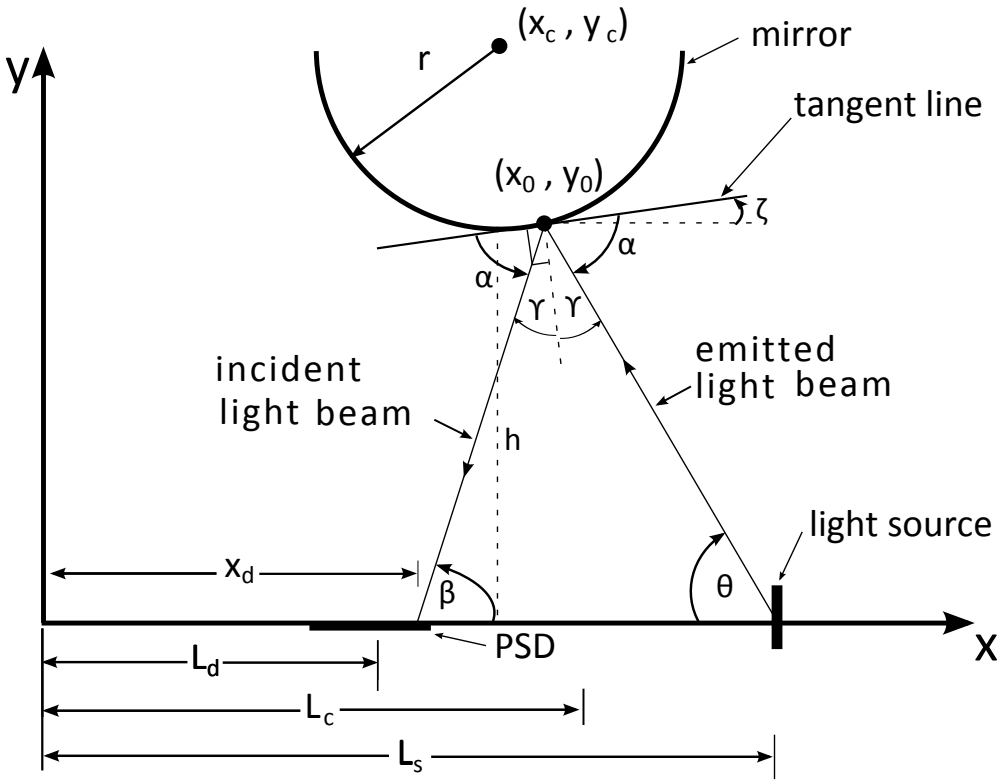

Figure A.2. Diagram of the optical gain setup in the equilibrium position with the new coordinate system imposed.

APPENDIX B

DERIVATION OF DAMPING MODEL

The purpose of this derivation is to obtain an equation for the shear stress acting on the lower portion of a floating disk in contact with the liquid. This is referred to as the damping shear stress. The model is based on Couette flow. This model assumes that the lower plate is stationary, while the upper moves in a sinusoidal fashion. An illustration of this concept can be found in Figure B.1.

The equation for the shear stress is

$$\tau_d = \mu \frac{du}{dy}\bigg|_{y=h} , \tag{B.1}$$

where τ_w is the dampingl shear stress, μ is the absolute viscosity of the liquid, h is the height of the gap between the disk and the base, y is the vertical distance within the gap and the function u is the velecity profile of the fluid film. To calculate the shear

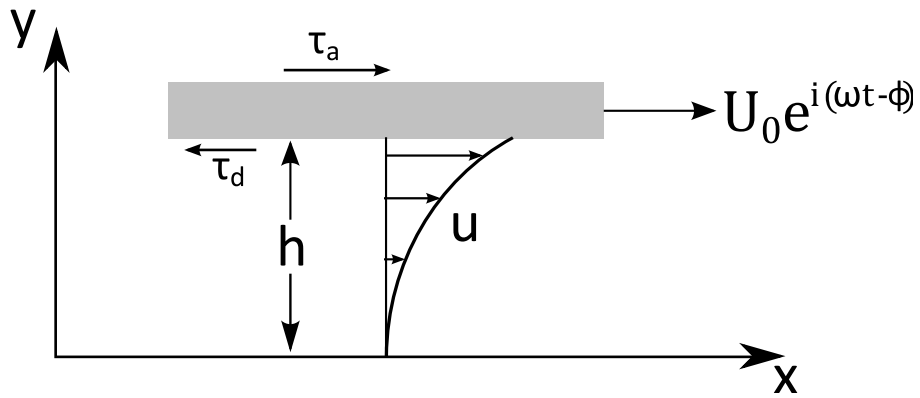

Figure B.1. Diagram of the unsteady Couette flow problem, where the upper boundary moves sinusoidally as given by Eulers equation.

stress, the function u must be obtained. This is done by simplifying the Navier-Stokes equation for a fluid between two infinite parallel plates. The simplified equation is

$$\frac{\partial u}{\partial t} = \nu \frac{\partial^2 u}{\partial y^2} \ , \tag{B.2}$$

where ν is the kinematic viscosity and t is time. The boundary conditions that are necessary to solve the equation are given as

$$u(0,t) = 0 \ , \tag{B.3}$$

and

$$u(h,t) = U_0 e^{i(\omega t - \phi)} \ , \tag{B.4}$$

where U_0 is the magnitude of the disk velocity, i is the imaginary unit, ω is the frequency of disk oscillation and ϕ is a constant phase shift of the disk. The method used to solve (B.2) is a sepaeration of variables technique, which assumes that u takes the form

$$u(y,t) = U_0 e^{i(\omega t - \phi)} \, F(y) \ , \tag{B.5}$$

where $F(y)$ is a function of y only. Using (B.5) and taking the necessary derivatives, then substituting into (B.2), the Navier-Stokes equation takes on the form

$$U_0 i\omega e^{i(\omega t - \phi)} F(y) - \nu U_0 e^{i(\omega t - \phi)} F''(y) = 0 \ . \tag{B.6}$$

From (B.6), one finds that $F(y)$ must satisfy the ODE: $F''(y) - i\omega/\nu F(y) = 0$. The expected solution is $F(y) = e^{ry}$, with r as the unknown characteristic coefficient, this results in

$$r^2 e^{ry} - \frac{i\omega}{\nu} e^{ry} = 0 \ . \tag{B.7}$$

Solving (B.7) for the characteristic coefficient gives

$$r = \pm \sqrt{\frac{i\omega}{\nu}} \ , \tag{B.8}$$

which is then substituted back into the solution $F(y) = e^{ry}$. The function F now becomes

$$F(y) = A e^{\sqrt{\frac{i\omega}{\nu}} y} + B e^{-\sqrt{\frac{i\omega}{\nu}} y} \ , \tag{B.9}$$

where A and B are unknown constants, which need to be solved for using the boundary conditions. The boundary conditions of F are

$$F(0) = 0 \ , \tag{B.10}$$

and

$$F(h) = 1. \tag{B.11}$$

After applying (B.10) and (B.11) and performing the necessary algebraic manipulations the function F is given by

$$F(y) = \frac{e^{\sqrt{\frac{i\omega}{\nu}}y} - e^{-\sqrt{\frac{i\omega}{\nu}}y}}{e^{\sqrt{\frac{i\omega}{\nu}}h} - e^{-\sqrt{\frac{i\omega}{\nu}}h}} \ . \tag{B.12}$$

Plugging (B.12) into (B.5) gives the equation for the velocity profile whithin the gap, which is given by

$$u(y,t) = U_0 e^{i(\omega t - \phi)} \frac{(e^{\sqrt{\frac{i\omega}{\nu}}y} - e^{-\sqrt{\frac{i\omega}{\nu}}y})}{(e^{\sqrt{\frac{i\omega}{\nu}}h} - e^{-\sqrt{\frac{i\omega}{\nu}}h})} \ . \tag{B.13}$$

The velocity profile described by (B.13) needs to be transformed into an equation with seperate real and imaginary parts. This is done by expanding the exponential terms in both the numerator and denominator. Using the rules for imaginary numbers and exponentials, the exponentials can be written as

$$e^{\sqrt{\frac{i\omega}{\nu}}} = e^{\sqrt{i}\sqrt{\frac{\omega}{\nu}}} = e^{\sqrt{\frac{\omega}{\nu}}(\frac{\sqrt{2}}{2} + i\frac{\sqrt{2}}{2})} = e^{\sqrt{\frac{\omega}{2\nu}}} e^{i\sqrt{\frac{\omega}{2\nu}}} \ . \tag{B.14}$$

Plugging (B.14) into (B.13) and letting $\lambda = \sqrt{\omega/2\nu}$, the velocity profile becomes

$$u(y,t) = U_0 e^{i(\omega t - \phi)} \frac{(e^{\lambda y} e^{i\lambda y} - e^{-\lambda y} e^{-i\lambda y})}{(e^{\lambda h} e^{i\lambda h} - e^{-\lambda h} e^{-i\lambda h})} \ . \tag{B.15}$$

The velocity profile is converted into sine and cosine form by applying Euler's equation which states

$$e^{i\lambda y} = \cos(\lambda y) + i \sin(\lambda y) \ . \tag{B.16}$$

Using (B.16) and after some algebraic manipulation $u(y,t)$ takes on the form

$$u(y,t) = U_0 e^{i(\omega t - \phi)} \frac{(\cos(\lambda y)(e^{\lambda y} - e^{-\lambda y}) + i \sin(\lambda y)(e^{\lambda y} + e^{-\lambda y}))}{(\cos(\lambda h)(e^{\lambda h} - e^{-\lambda h}) + i \sin(\lambda h)(e^{\lambda h} + e^{-\lambda h}))} \ . \tag{B.17}$$

Equation (B.17) can be simplified further, if the definition for hyperbolic sine and cosine are used. The definitions are given by the following

$$e^{\lambda y} - e^{-\lambda y} = 2\sinh(\lambda y) \tag{B.18}$$

and

$$e^{\lambda y} + e^{\lambda y} = 2\cosh(\lambda y)\ . \tag{B.19}$$

Substituting (B.18) and (B.19) into (B.17) yields

$$u(y,t) = U_0 e^{i(\omega t-\phi)} \frac{(2\cos(\lambda y)\sinh(\lambda y) + i2\sin(\lambda y)\cosh(\lambda y))}{(2\cos(\lambda h)\sinh(\lambda h) + i2\sin(\lambda h)\cosh(\lambda h))}\ . \tag{B.20}$$

It is desired that (B.20) be put into a standard form with a real denominator. To accomplish this, both the numerator and denominator of (B.20) are multiplied by the complex conjugate of the denominator. After some algebraic manipulations and seperating into real and imaginary parts the equation for $u(y,t)$ becomes

$$\begin{aligned} u(y,t) = {} & U_0 e^{i(\omega t-\phi)} \frac{(\cos(\lambda y)\sinh(\lambda y)\cos(\lambda h)\sinh(\lambda h))}{(\cos^2(\lambda h)\sinh^2(\lambda h) + \sin^2(\lambda h)\cosh^2(\lambda h))} \\ & + U_0 e^{i(\omega t-\phi)} \frac{(\sin(\lambda y)\cosh(\lambda y)\sin(\lambda h)\cosh(\lambda h))}{(\cos^2(\lambda h)\sinh^2(\lambda h) + \sin^2(\lambda h)\cosh^2(\lambda h))} \\ & - U_0 e^{i(\omega t-\phi)} \frac{i(\sin(\lambda y)\cosh(\lambda y)\cos(\lambda h)\sinh(\lambda h))}{(\cos^2(\lambda h)\sinh^2(\lambda h) + \sin^2(\lambda h)\cosh^2(\lambda h))} \\ & + U_0 e^{i(\omega t-\phi)} \frac{i(\cos(\lambda y)\sinh(\lambda y)\sin(\lambda h)\cosh(\lambda h))}{(\cos^2(\lambda h)\sinh^2(\lambda h) + \sin^2(\lambda h)\cosh^2(\lambda h))}\ . \end{aligned} \tag{B.21}$$

The next step in this derivation involves applying Euler's equation one more time, only this time it is used to expand the time varying term $e^{i(\omega t-\phi)}$. Note, a nondimensional substitution can be made using $\tilde{y} \equiv (y/h)$, this allows the function $u(y,t)$ to be written using the Womersley number, $\beta = \sqrt{\omega/2\nu}h$. After applying Euler's equation, and writing in terms of the Womersley number, the final form of the velocity profile function is

$$u(\tilde{y},t) = U_0\cos(\omega t-\phi)\frac{(\cos(\beta\tilde{y})\sinh(\beta\tilde{y})\cos(\beta)\sinh(\beta))}{(\cos^2(\beta)\sinh^2(\beta)+\sin^2(\beta)\cosh^2(\beta))} + U_0\cos(\omega t-\phi)\frac{(\sin(\beta\tilde{y})\cosh(\beta\tilde{y})\sin(\beta)\cosh(\beta))}{(\cos^2(\beta)\sinh^2(\beta)+\sin^2(\beta)\cosh^2(\beta))} - U_0\sin(\omega t-\phi)\frac{(\sin(\beta\tilde{y})\cosh(\beta\tilde{y})\cos(\beta)\sinh(\beta))}{(\cos^2(\beta)\sinh^2(\beta)+\sin^2(\beta)\cosh^2(\beta))} + U_0\sin(\omega t-\phi)\frac{(\cos(\beta\tilde{y})\sinh(\beta\tilde{y})\sin(\beta)\cosh(\beta))}{(\cos^2(\beta)\sinh^2(\beta)+\sin^2(\beta)\cosh^2(\beta))} \ . \quad \text{(B.22)}$$

With the equation for the velocity profile known, the shear stress is calculated by taking a derivitve of u with respect to $\tilde{y}$, then evaluting the result at $\tilde{y}=1$ as given in (B.1). The final form for the shear stress on the lower surface of the disk is

$$\tau_d = U_0\mu\sqrt{\omega/2\nu}\cos(\omega t-\phi)\frac{(\sinh(\beta)\cosh(\beta)+\sin(\beta)\cos(\beta))}{(\cos^2(\beta)\sinh^2(\beta)+\sin^2(\beta)\cosh^2(\beta))} - U_0\mu\sqrt{\omega/2\nu}\sin(\omega t-\phi)\frac{(\sinh(\beta)\cosh(\beta)-\sin(\beta)\cos(\beta))}{(\cos^2(\beta)\sinh^2(\beta)+\sin^2(\beta)\cosh^2(\beta))} \ . \quad \text{(B.23)}$$

Equation (B.23) has both a sine and cosine term indicating the presence of a phase shift. Therefore, one can rewrite (B.23) as

$$\tau_d = \tilde{c}\,U_0\cos(\omega t-\phi+\gamma). \quad \text{(B.24)}$$

To determine $\tilde{c}$ and γ in (B.24), the following variables are defined:

$$A = \frac{\mu/h\,\beta}{(\cos^2(\beta)\sinh^2(\beta)+\sin^2(\beta)\cosh^2(\beta))} \ , \quad \text{(B.25)}$$

$$B = (\sinh(\beta)\cosh(\beta)+\sin(\beta)\cos(\beta)) \ , \quad \text{(B.26)}$$

$$D = (\sinh(\beta)\cosh(\beta)-\sin(\beta)\cos(\beta)) \ , \quad \text{(B.27)}$$

$$\alpha = (\omega t-\phi) \ . \quad \text{(B.28)}$$

The shear stress in (B.23) may be expressed as

$$\tau_d = A\,U_0(B\cos(\alpha)-D\sin(\alpha)) \ . \quad \text{(B.29)}$$

Equating (B.24) and (B.29) and dividing through by U_0

$$\tilde{c}\cos(\alpha+\gamma) = A\,B\cos(\alpha)-A\,D\sin(\alpha) \ . \quad \text{(B.30)}$$

To find the phase angle, a trigonometric identity is needed to expand the left hand side of (B.30),

$$\cos(\alpha+\gamma) = \cos(\gamma)\cos(\alpha) - \sin(\gamma)\cos(\alpha) \ . \tag{B.31}$$

After applying (B.31) to (B.30), the result is

$$\tilde{c}\cos(\gamma)\cos(\alpha) - \tilde{c}\sin(\gamma)\sin(\alpha) = A\,B\cos(\alpha) - A\,D\sin(\alpha) \ . \tag{B.32}$$

The phase angle is found by taking the sine and cosine terms seperately. The sine terms become

$$\tilde{c}\sin(\gamma) = A\,D \ ; \tag{B.33}$$

and, the cosine terms become

$$\tilde{c}\cos(\gamma) = A\,B \ . \tag{B.34}$$

Dividing (B.33) by (B.34) gives

$$\frac{\tilde{c}\sin(\gamma)}{\tilde{c}\cos(\gamma)} = \frac{A\,D}{A\,B} \ . \tag{B.35}$$

Simplifying and solving (B.35) for γ, yields the equation of the phase shift,

$$\gamma = \arctan\left(\frac{D}{B}\right) \ , \tag{B.36}$$

or, substituting back in for D and B,

$$\gamma = \arctan\left(\frac{\sinh(\beta)\cosh(\beta) - \sin(\beta)\cos(\beta)}{\sinh(\beta)\cosh(\beta) + \sin(\beta)\cos(\beta)}\right) \ . \tag{B.37}$$

The magnitude, $\tilde{c}$, is found by squaring (B.33) and (B.34), then adding the two resultant equations, the result of which is

$$\tilde{c}^2\left(\sin^2(\gamma) + \cos^2(\gamma)\right) = A^2\,D^2 + A^2\,B^2 \ . \tag{B.38}$$

To simplify, another trigonometric identity is used,

$$\sin^2(\gamma) + \cos^2(\gamma) = 1 \ . \tag{B.39}$$

After applying (B.39) to (B.38), then taking the square root, the equation for $\tilde{c}$ becomes,

$$\tilde{c} = \sqrt{A^2\,D^2 + A^2\,B^2}\ , \tag{B.40}$$

or, substituting back in for A, D, and B,

$$\tilde{c} = \frac{\mu\,/h\,\beta[(\sinh\beta\cosh\beta - \sin\beta\cos\beta)^2 + (\sinh\beta\cosh\beta + \sin\beta\cos\beta)^2]^{1/2}}{(\cos^2\beta\sinh^2\beta + \sin^2\beta\cosh^2\beta)}\ . \tag{B.41}$$

Simplifying the above expression gives

$$\tilde{c} = \sqrt{2}\,\beta\,\frac{\mu}{h}\frac{[\sinh^2\beta\cosh^2\beta + \sin^2\beta\cos^2\beta]^{1/2}}{(\cos^2\beta\sinh^2\beta + \sin^2\beta\cosh^2\beta)}\ . \tag{B.42}$$

B.1 Steady Couette Flow

For the case of constant disk velocity, $U_0 = \text{constant}$, the velocity profile is linear as shown in Figure B.2. The derivation becomes simpler than the oscillating disk velocity case because of the linear velocity profile. The damping shear stress, τ_d, is given as

$$\tau_d = \mu\,\left.\frac{du}{dy}\right|_{y=h}\ . \tag{B.43}$$

The velocity profile function, u, is determined by the equation of the line

$$u = \frac{U_0}{h}\,y\ , \tag{B.44}$$

where h is the gap height from the baseplate to the underside of the floating disk, and y is the vertical distance within the liquid layer. The derivitive of (B.44) with respect to y is given by

$$\frac{du}{dy} = \frac{U_0}{h}\ . \tag{B.45}$$

Substituting (B.45) into (B.43) gives

$$\tau_d = \frac{\mu\,U_0}{h}\ . \tag{B.46}$$

To find the damping force, F_d, acting on the underside of the disk (B.46) is multiplied by the surface area that is in contact with the liquid layer, A_s, giving the force

$$F_d = \frac{\mu\,A_s}{h}U_0 = c\,U_0\ . \tag{B.47}$$

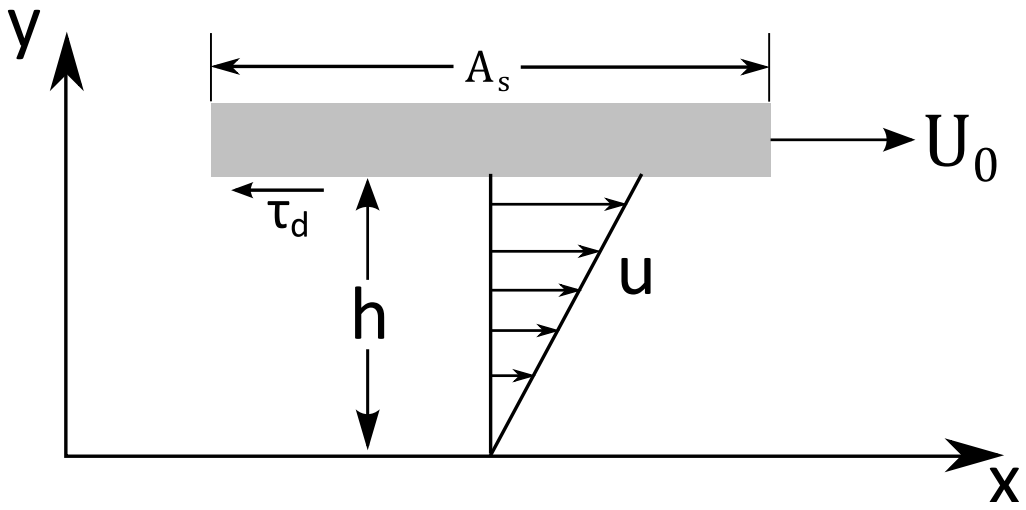

Figure B.2. Steady Couette flow illustration with outlined damping force derivation shown.

Note, this is the form of the damping force that is expected for steady Couette flow, i.e. $F_d = c\,U_0$.

APPENDIX C

OVERALL EQUATION OF MOTION DERIVATION

To begin the derivation of the overall equation of motion for the floating disk, the free body diagram is depicted in Figure C.1. When Newton's second law of motion $F = ma$ is applied,

$$m\ddot{x} = f_0 \sin \omega t - \tau_d A_s - k_{eff} x \ . \tag{C.1}$$

Displaying (C.1) in standard form the overall equation of motion for this case is given by

$$m\ddot{x} + \tau_d \, A_s + k_{eff} x = f_0 \sin \omega t \ , \tag{C.2}$$

where A_s is the surface area of the underside of the disk in contact with the liquid. To solve (C.2), a function for the position is assumed to be sinusoidal, and is given by

$$x = X \ \sin \left(\omega t - \phi \right) \ , \tag{C.3}$$

where X is the amplitude of the position, and ϕ is the phase shift. The derivitives of (C.3) with respect to time are

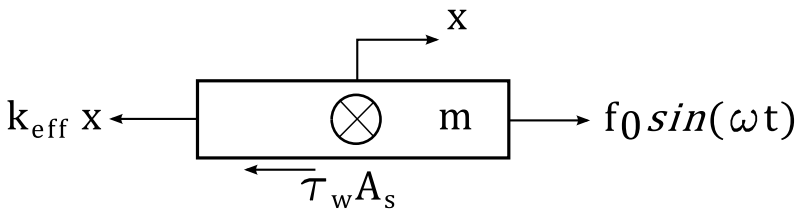

Figure C.1. Free body diagram of the mass-spring-damper system used for the vibration model.

$$\dot{x} = \omega\, X \cos\left(\omega t - \phi\right) \tag{C.4}$$

and

$$\ddot{x} = -\omega^2\, X \sin\left(\omega t - \phi\right). \tag{C.5}$$

Substituting in for τ_d using (B.24) from appendix B and the fact that $U_0 = \omega\, X$

$$\tau_d = \tilde{c}\,\omega\, X \cos\left(\omega t - \phi + \gamma\right) \ , \tag{C.6}$$

where

$$\gamma = \arctan\left(\frac{\sinh\left(\beta\right)\cosh\left(\beta\right) - \sin\left(\beta\right)\cos\left(\beta\right)}{\sinh\left(\beta\right)\cosh\left(\beta\right) + \sin\left(\beta\right)\cos\left(\beta\right)}\right) \ , \tag{C.7}$$

$$\tilde{c} = \sqrt{2}\beta\frac{\mu}{h}\frac{\left[\sinh^2\left(\beta\right)\cosh^2\left(\beta\right) + \sin^2\left(\beta\right)\cos^2\left(\beta\right)\right]^{1/2}}{\left[\cos^2\left(\beta\right)\sinh^2\left(\beta\right) + \sin^2\left(\beta\right)\cosh^2\left(\beta\right)\right]} \ , \tag{C.8}$$

$$\beta = \sqrt{\frac{\omega}{2\nu}}h \ . \tag{C.9}$$

Substitute the above equations into (C.2), with $c = \tilde{c}A_s$, then dividing by m gives

$$-\omega^2 X \sin\left(\omega t - \phi\right) + \frac{c}{m}\omega X \cos\left(\omega t - \phi + \gamma\right) + \omega_n^2 X \sin\left(\omega t - \phi\right) = \frac{f_0}{m}\sin\left(\omega t\right). \tag{C.10}$$

The phase shifts γ and ϕ need to be separated from (C.10). This is done by applying the following trigonometric identities

$$\begin{aligned}
\cos\left(\omega t - \phi + \gamma\right) &= \cos\left(\omega t - \phi\right)\cos\left(\gamma\right) - \sin\left(\omega t - \phi\right)\sin\left(\gamma\right), \\
\cos\left(\omega t - \phi\right) &= \cos\left(\omega t\right)\cos\left(\phi\right) + \sin\left(\omega t\right)\sin\left(\phi\right), \\
\sin\left(\omega t - \phi\right) &= \sin\left(\omega t\right)\cos\left(\phi\right) - \cos\left(\omega t\right)\sin\left(\phi\right).
\end{aligned} \tag{C.11}$$

Further simplification is made by introducing the damping ratio ζ, let $2\zeta\omega_n = c/m$, this yields

$$\begin{aligned}
-\,\omega^2 X[&\sin\left(\omega t\right)\cos\left(\phi\right) - \cos\left(\omega t\right)\sin\left(\phi\right)] \\
&+ 2\zeta\omega_n\omega X\cos\left(\gamma\right)[\cos\left(\omega t\right)\cos\left(\phi\right) + \sin\left(\omega t\right)\sin\left(\phi\right)] \\
&- 2\zeta\omega_n\omega X\sin\left(\gamma\right)[\sin\left(\omega t\right)\cos\left(\phi\right) - \cos\left(\omega t\right)\sin\left(\phi\right)] \\
&+ \omega_n^2 X[\sin\left(\omega t\right)\cos\left(\phi\right) - \cos\left(\omega t\right)\sin\left(\phi\right)] - \frac{f_0}{m}\sin\left(\omega t\right) = 0\,.
\end{aligned} \tag{C.12}$$

Separating the sine and cosine terms:

$$[-\omega^2 X\cos(\phi) + 2\zeta\omega_n\omega X\cos(\gamma)\sin(\phi) - 2\zeta\omega_n\omega X\sin(\gamma)\cos(\phi) + \omega_n^2 X\cos(\phi) - f_0/m]\sin(\omega t) = 0 \ , \tag{C.13}$$

$$[\omega^2 X\sin(\phi) + 2\zeta\omega_n\omega X\cos(\gamma)\cos(\phi) + 2\zeta\omega_n\omega X\sin(\gamma)\sin(\phi) - \omega_n^2 X\sin(\phi)]\cos(\omega t) = 0 \ . \tag{C.14}$$

The phase shift, ϕ, is found by starting with (C.14) and dividing by $cos(\omega t)\cos(\phi)$, simplifying gives

$$[(\omega^2 - \omega_n^2) + 2\zeta\omega_n\omega\sin(\gamma)]\tan(\phi) + 2\zeta\omega_n\omega\cos(\gamma) = 0 \ . \tag{C.15}$$

Dividing (C.15) by ω_n^2 yields

$$\left[-\left(1 - \left(\frac{\omega}{\omega_n}\right)^2\right) + 2\zeta\left(\frac{\omega}{\omega_n}\right)\sin(\gamma)\right]\tan(\phi) + 2\zeta\left(\frac{\omega}{\omega_n}\right)\cos(\gamma) = 0 \ . \tag{C.16}$$

Solving for $\tan(\phi)$ gives

$$\tan(\phi) = \frac{2\zeta(\omega/\omega_n)\cos(\gamma)}{(1-(\omega/\omega_n)^2) - 2\zeta(\omega/\omega_n)\sin(\gamma)} \ . \tag{C.17}$$

The angle, ϕ, is found by taking the arctan of both sides. This gives

$$\phi = \arctan\left(\frac{2\zeta(\omega/\omega_n)\cos(\gamma)}{(1-(\omega/\omega_n)^2) - 2\zeta(\omega/\omega_n)\sin(\gamma)}\right) \ . \tag{C.18}$$

This is the final form of the phase shift ϕ, where

$$\gamma = \arctan\left(\frac{\sinh(\beta)\cosh(\beta) - \sin(\beta)\cos(\beta)}{\sinh(\beta)\cosh(\beta) + \sin(\beta)\cos(\beta)}\right) \ , \tag{C.19}$$

$$\omega_n^2 = \frac{k_{eff}}{m} \ , \tag{C.20}$$

$$\beta = \sqrt{\frac{\omega}{2\,\nu}} \ , \tag{C.21}$$

$$\zeta = \frac{c}{2m\omega_n} = \zeta_0\sqrt{2}\beta\frac{[\sinh^2(\beta)\cosh^2(\beta) + \sin^2(\beta)\cos^2(\beta)]^{1/2}}{[\cos^2(\beta)\sinh^2(\beta) + \sin^2(\beta)\cosh^2(\beta)]} \ . \tag{C.22}$$

Note, both $\gamma = \gamma(\beta)$ and $\zeta = \zeta(\beta)$ and $\zeta_0 = \mu A_s/2mh\omega_n$ is a nondimensional number that characterizes the strength of the damping coefficient.

To find the transfer function (TF), (C.13) is used. Dividing by $\sin(\omega t)$ and bringing f_0/m to the right hand side (RHS)

$$-\omega^2 X\cos(\phi) + 2\zeta\omega_n\omega X\cos(\gamma)\sin(\phi) - 2\zeta\omega_n\omega X\sin(\gamma)\cos(\phi) + \omega_n^2 X\cos(\phi) = \frac{f_0}{m}\ . \quad \text{(C.23)}$$

Factoring out X from the LHS and multypling the RHS by (k_{eff}/k_{eff}), a form of 1

$$X[-\omega^2 + \omega_n^2 - 2\zeta\omega_n\omega\sin(\gamma) + 2\zeta\omega_n\cos(\gamma)\tan(\phi)] = \frac{f_0}{m\cos(\phi)}\left(\frac{k_{eff}}{k_{eff}}\right)\ . \quad \text{(C.24)}$$

Now, solving for $X/(f_0/k_{eff})$ and substituting in $\omega_n^2 = k_{eff}/m$ yields

$$\frac{X}{f_0/k_{eff}} = \frac{\omega_n^2}{\cos(\phi)}\left[2\zeta\omega_n\omega\cos(\gamma)\tan(\phi) + (\omega_n^2 - \omega^2) - 2\zeta\omega_n\omega\sin(\gamma)\right]^{-1}\ . \quad \text{(C.25)}$$

Equation (C.25) can be simplified by bringing ω_n^2 into the brackets

$$\frac{X}{f_0/k_{eff}} = \frac{1}{\cos(\phi)}\left[2\zeta\left(\frac{\omega}{\omega_n}\right)\cos(\gamma)\tan(\phi) + 1 - \left(\frac{\omega}{\omega_n}\right)^2 - 2\zeta\left(\frac{\omega}{\omega_n}\right)\sin(\gamma)\right]^{-1}\ . \quad \text{(C.26)}$$

Substituting in for $\tan(\phi)$ from (C.17):

$$\frac{X}{f_0/k_{eff}} = \frac{1}{\cos(\phi)}\left[\frac{1 - (\omega/\omega_n)^2 - 2\zeta(\omega/\omega_n)\sin(\gamma)}{(2\zeta(\omega/\omega_n)\cos(\gamma))^2 + (1 - (\omega/\omega_n)^2 - 2\zeta(\omega/\omega_n)\sin(\gamma))^2}\right]\ . \quad \text{(C.27)}$$

The equation for $\cos(\phi)$ is found using the $\tan(\phi)$ relationship as follows

$$\cos(\phi) = \frac{1 - (\omega/\omega_n)^2 - 2\zeta(\omega/\omega_n)\sin(\gamma)}{\sqrt{(2\zeta(\omega/\omega_n)\cos(\gamma))^2 + (1 - (\omega/\omega_n)^2 - 2\zeta(\omega/\omega_n)\sin(\gamma))^2}}\ . \quad \text{(C.28)}$$

Substituting (C.28) in for $\cos(\phi)$:

$$\frac{X}{f_0/k_{eff}} = \frac{1}{[(2\zeta(\omega/\omega_n)\cos(\gamma))^2 + (1 - (\omega/\omega_n)^2 - 2\zeta(\omega/\omega_n)\sin(\gamma))^2]^{1/2}}\ . \quad \text{(C.29)}$$

This is the final form of the transfer function used in the analysis.

It is instructive to ask the question of whether (C.18) and (C.29) reduce to the case for a damping force with a constant coefficient of the form $F_d = c\dot{x}$ for small β.

For this case the equation for phase shift and transfer function assuming a sinusoidal forcing function and constant damping coefficient c are given by

$$\phi = \arctan\left(\frac{2\zeta(\omega/\omega_n)}{1-(\omega/\omega_n)^2}\right) , \tag{C.30}$$

$$\frac{X}{f_0/m} = \frac{1}{\left[\left(1-\left(\frac{\omega}{\omega_n}\right)^2\right)^2 + \left(2\zeta\left(\frac{\omega}{\omega_n}\right)\right)^2\right]^{1/2}} , \tag{C.31}$$

respectively (Inman, 2008).

For $\beta << 1$, the following approximations may be made:

$$\cos(\beta) \approx 1 \ ,$$
$$\cosh(\beta) \approx 1 \ ,$$
$$\sin(\beta) \approx \beta \ ,$$
$$\sinh(\beta) \approx \beta \ .$$

Therefore, for $\beta << 1$,

$$\gamma = \arctan\left(\frac{(\beta)(1)-(\beta)(1)}{(\beta)(1)+(\beta)(1)}\right) = 0 \ , \tag{C.32}$$

$$\zeta = \frac{\sqrt{2}}{2}\left(\frac{\mu A_s}{mh\omega_n}\right)\beta\frac{[\beta^2(1)+\beta^2(1)]^{1/2}}{[(1)\beta^2+\beta^2(1)]} = \frac{\sqrt{2}}{2}\left(\frac{\mu A_s}{mh\omega_n}\right)\beta\frac{\sqrt{2}\beta}{2\beta^2} \ , \tag{C.33}$$

$$\zeta = \frac{\mu A_s}{2mh\omega_n} \quad \text{or} \quad c = \frac{\mu A_s}{h} \ . \tag{C.34}$$

Note, this is the damping coefficient that would be expected for steady Couette flow, as shown in Appendix B.

Therefore, for $\beta << 1$, $\gamma = 0$ and ζ = constant, and, $\cos(\gamma) = 1$, $\sin(\gamma) = 0$. This yields

$$\phi = \arctan\left(\frac{2\zeta(\omega/\omega_n)}{1-(\omega/\omega_n)^2}\right), \tag{C.35}$$

$$\frac{X}{f_0/k_{eff}} = \frac{1}{\left[\left(2\zeta\left(\frac{\omega}{\omega_n}\right)\right)^2 + \left(1-\left(\frac{\omega}{\omega_n}\right)^2\right)^2\right]^{1/2}}, \tag{C.36}$$

which agrees with the result for a constant damping coefficient as given by (C.30) and (C.31).

APPENDIX D

ASSEMBLY INSTRUCTIONS

Assembly Instructions

Introduction

Before you get started with the assembly of this unit, please make sure that you have all of the necessary parts, which can be found from the parts list. The assembly procedure is divided into five categories. These are as follows: 1) The preparation of all needed parts. This includes all of the necessary secondary operations, which must be performed on the parts as they come from the manufacturer. 2) The assembly of all components that are attached directly to the base unit. 3) The assembly of the gear mount and pinion shaft. 4) The assembly of the floating disk and springs. 5) The overall assembly of the entire unit. These assembly instructions do not cover the attachment of any peripheral device to the unit itself.

Section 1: Preparation of Needed Parts

In this section you will need to prepare 8 different parts before they can be assembled onto the complete unit. Each part will have a series of steps, which need to be completed before the part is ready for assembly.

Part 1: Bronze Bushing

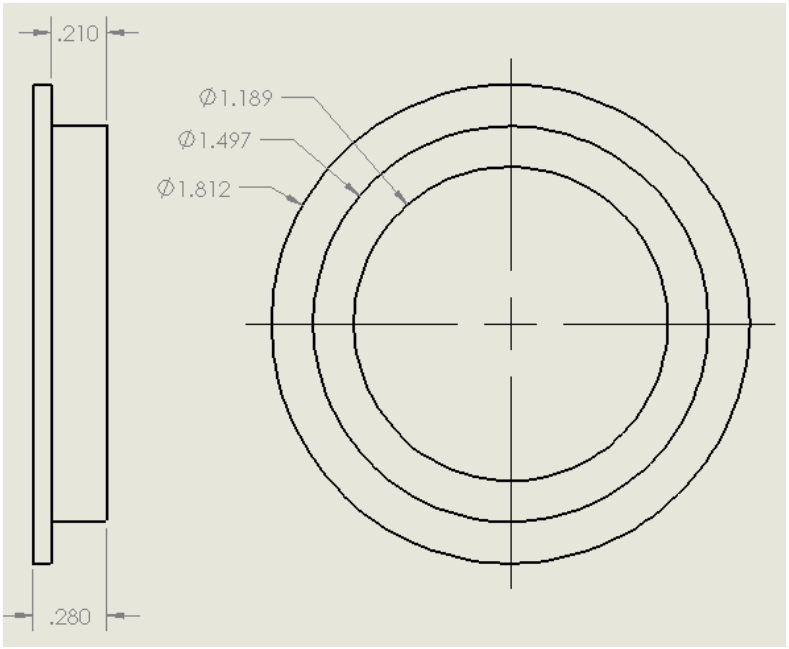

Step 1:
Use the lathe to turn down the narrow portion of the bushing until it reaches 0.210'', as measured from the back of the flange.

Step 2:
Remove work piece and rotate in the lathe to expose the front of the flange. Use the lathe to turn down the flange, until the flange thickness reaches 0.070''.

Step 3:
Make sure and clean the machined edges using a de-burring tool, such as a hand held rout-a-burr. The part is now ready for install.

Part 2: Ultra-Fine Adjustment Screws

Step 1
Remove the outer brass housing from one of the ultra-fine adjustment screws. Then install it backwards onto another screw to lock it in place.

Step 2
Install each of the metric m10 x 1.0 nuts onto the brass housings. This allows the ultra-fine screws to be placed in a vice for machining.

Step 3
Install some pipe thread tape around the fine threads that are closest to the flat end of the screws. This helps to prevent the metal chips from embedding in the fine threads, while the screws are machined.

Step 4
With a mill, machine a hole using a #44 solid carbide drill that is approx ¼ in deep into the center of the flat end of the screw. Once the hole is complete, remove any chips from the screw. Also, remove the pipe thread tape along with both of the nuts and the extra brass housing. Repeat each step until all of the ultra-fine adjustment screws have been drilled.

Part 3: Pinion Shaft

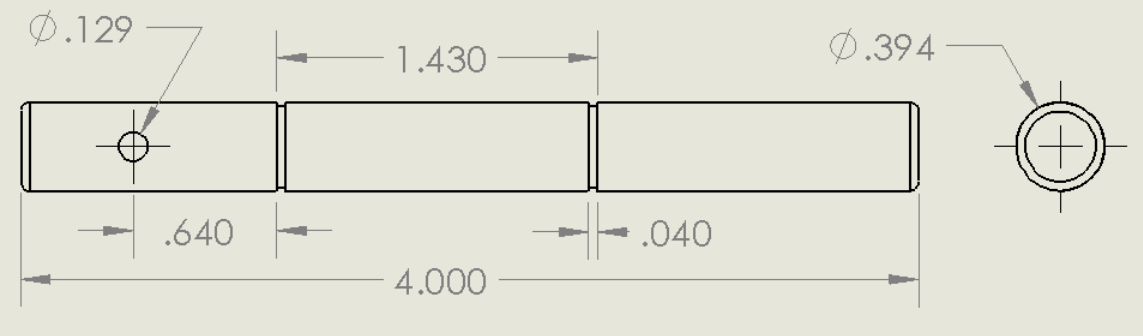

Step 1
Set up the 10 mm aluminum shaft stock in a lathe using a live center. Make sure you have at least 5 inches of material available to work with. Then, use an extremely fine sandpaper (approx 1500 grit), or emery cloth to polish the shaft until it fits through the bearings.

Step 2
Make the necessary e-clip grooves using a grooving tool or equivalent. Remove the work piece from the lathe.

Step 3
Cut the pinion shaft to the proper length using a band saw or equivalent method. Set up the shaft in a mill and drill a 1/8 inch through-hole centered at 0.640'' from the edge of the first groove.

Step 4
Be sure and use a de-burring tool to remove all rough edges from the through-hole and parted surfaces. The pinion shaft is now ready for install.

Part 4: Tension Pin Holes in Gears

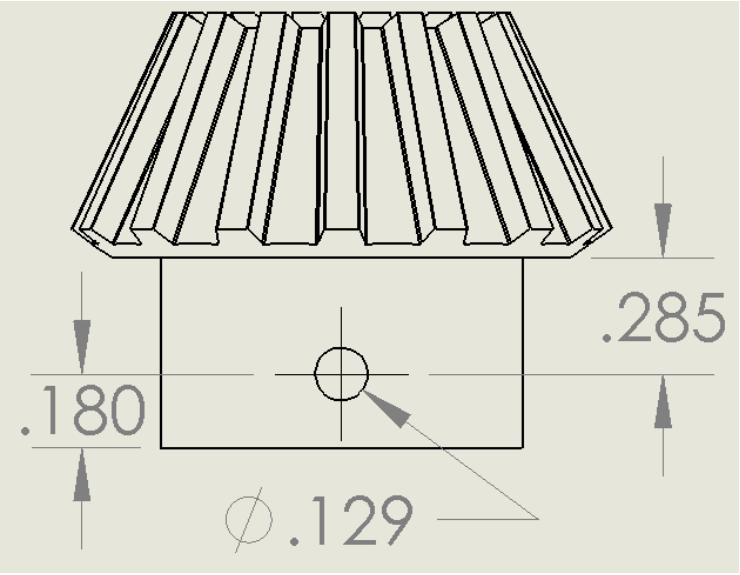

Step 1
Set up the pinion gear (the smaller one) in a mill, so a through-hole can be drilled.

Step 2

Through the center of the gear, drill a through-hole using a #30 drill bit that is 0.180” from the flat end of the gear. Remove the gear from the mill vice. Clean up any burs using sandpaper and a de-burring tool. The pinion gear is now ready for install.

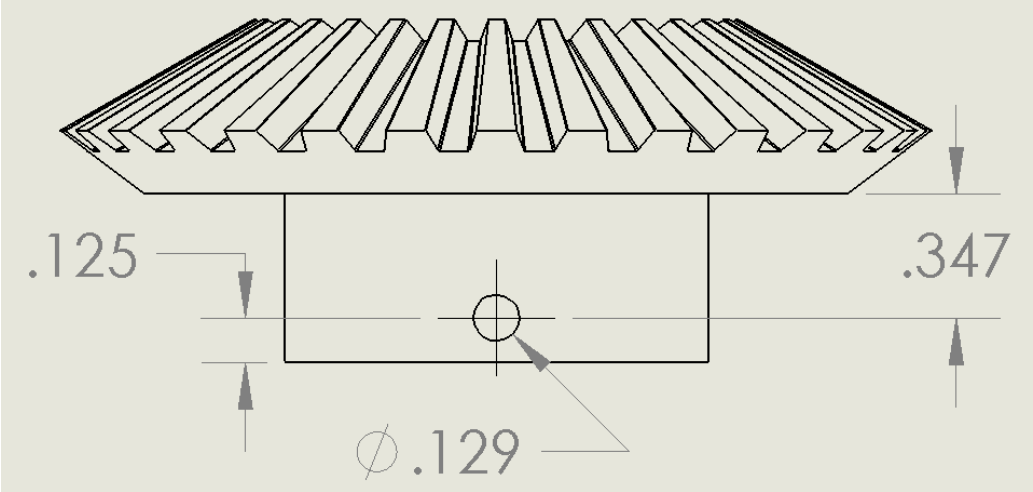

Step 3

Set up the bevel gear (the larger one) in a mill, so that a through hole can be drilled. This hole is used to accept a tension pin.

Step 4

Through the center of the gear, drill a through hole using a #30 drill bit. This hole should be placed 0.125” from the flat end of the gear. Remove the gear from the vice and clean any rough edges using sandpaper and/or a de-burring tool. The bevel gear is now ready for install.

Part 5: Sensor Holder Plug

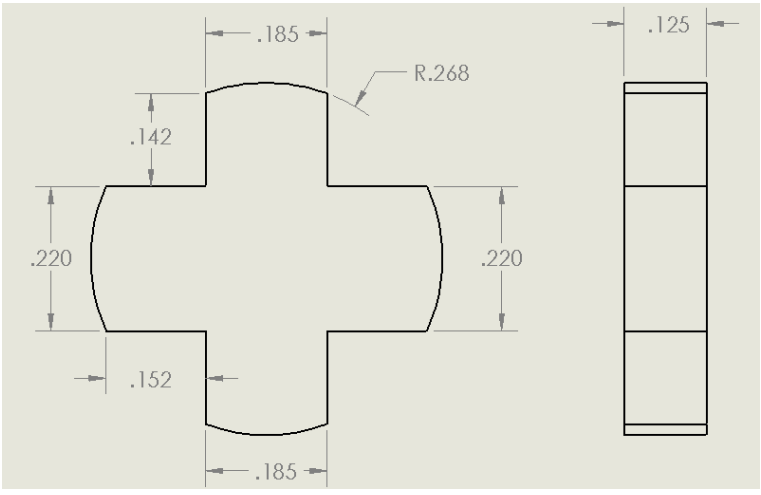

Step 1
Take a 2 ½ inch piece of the Delrin stock and set it up in the lathe. Turn down ½ inch of the end to a diameter of 0.536". Remove from the lathe.

Step 2
Set up the Delrin work piece in a mill, and using a 1/16 inch end mill notch a cross into the top surface as shown in the figure below. Make sure to cut as deep as the tool will allow.

Step 3
Remove the work piece from the mill and secure it in the lathe. Now part the end of the cross piece to a thickness of 0.125". Retrieve the part and clean up any needed surfaces. The part is now ready for install.

Part 6: Aluminum Plug

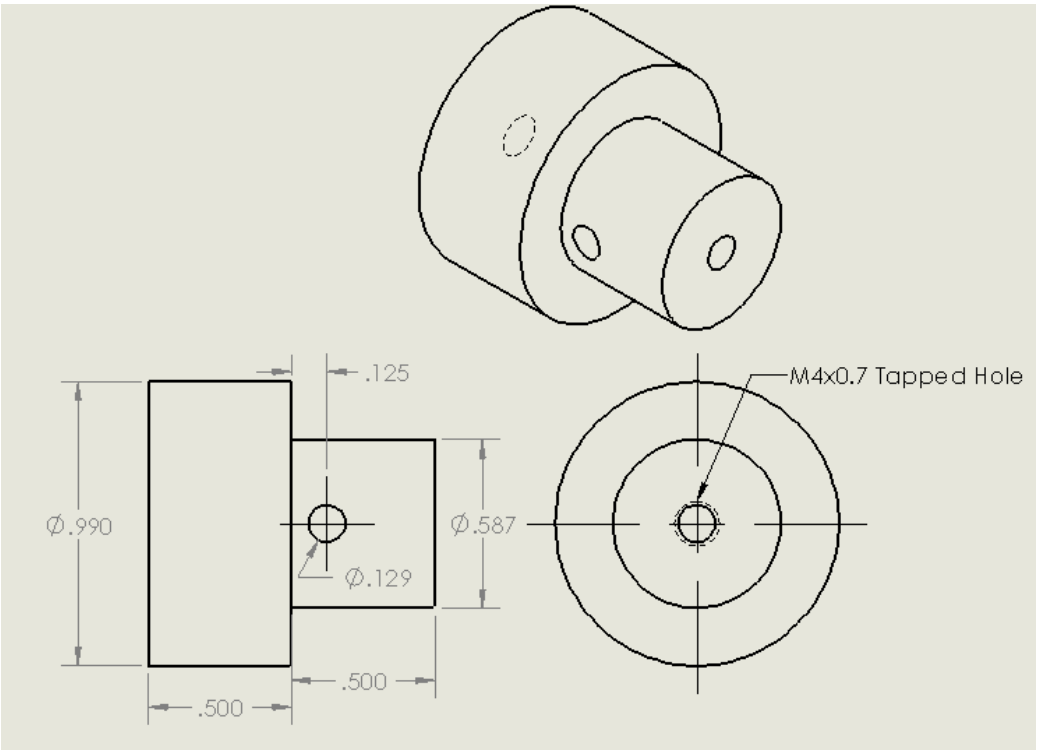

Step 1
Set up the 1" aluminum rod stock in the lathe, and then turn down 0.5" of the end to a diameter of 0.587". Drill a blind hole in the center of the stock to a depth greater than 1". Remove the work piece from the lathe.

Step 2
Set up the work piece in the mill, and drill a through hole using a #44 drill bit located 0.125” from the flange. Remove the work piece from the mill.

Step 3
Finish off the work piece by tapping an m4 x 0.7 metric thread into the larger diameter side of the work piece. Be sure and clean up any rough edges using sandpaper or a de-burring tool. The part is now ready for install.

Part 7: Disk Center Hub

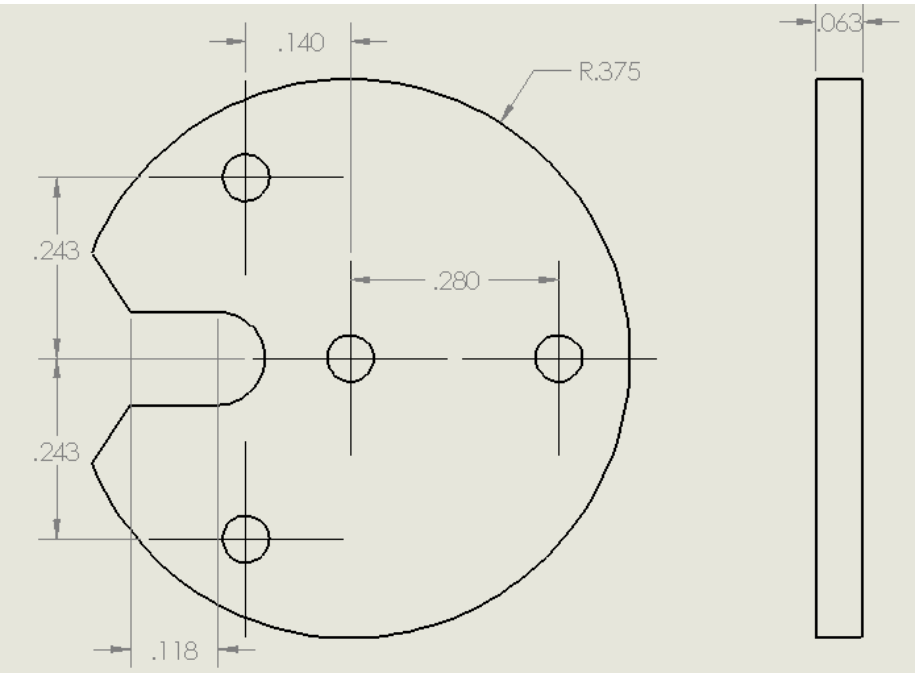

Step 1
Set up a 3” piece of the 0.75” Delrin stock in the lathe, and then face the end of the work piece. Remove from the lathe.

Step 2
Set up the work piece in a mill with the faced end flush with the vice. Remove some material from the rough end to make it parallel with the smooth faced end.

Step 3
Change tools to a 0.0625” end mill, and then center the tool in the work piece. Mill the center hole as deep as the tool will allow, approx. 0.125”. Proceed to mill the other three holes in their respective positions.

Step 4
Change tools to a 0.125” end mill, and then mill the slot for the index tab of the foam disk. Remove the work piece from the mill. NOTE: It is acceptable to adjust the work piece to create the angle for the tab.

Step 5
Set up the work piece in the lathe and part off to a thickness of 0.0625”. Retrieve and clean the work piece. The part is now ready for install.

Part 8: 2-56 Eyelets

Step 1
Locate the 2-56 eyelets, and then using dikes clip a small amount of material from the hook to allow easy access of the spring connection. Repeat for all three eyelets. The parts are now ready for install.

Section 2: Assembly of the base components

Now that all of the needed parts have been prepped, we can proceed with the actual assembly of the base unit. This will consist of installing all the components, which are attached to the base unit itself.

Step 1
Locate the ultra-fine adjustment screws and the 2-56 threaded eyelets. Thread three of the 2-56 nuts onto the eyelets, making sure to thread them all the way to the top. Next, put a drop of super glue adhesive into the drilled hole on the ultra-fine adjustment screws, and then insert the eyelet nut combination into the hole with the glue. Allow to dry for a few seconds before letting go. Set aside to allow the adhesive to cure, usually about one minute. Repeat until all three ultra-fine adjustment screws have been glued.

Step 2
Install each of the three ultra-fine adjustment screws into their respective threaded holes on the top of the base unit.

Step 3
Locate the red and black banana jacks from the parts. Install the banana jacks into their slots on the base unit, which are located on either side of one of the ultra-fine adjustment screws. Install the red on the left and the black on the right, by pushing the jack through the slot with the terminal pins in the horizontal direction. Tighten the nuts on the reverse side.

Step 4
Turn the base unit over, and install one of the brass pipe barbs into the pipe thread hole located near the edge of the unit. Make sure to wrap about a 3” piece of pipe thread seal tape

in the counter clockwise direction around the threads before install. Tighten with a wrench until snug. NOTE: Be careful not to over tighten as this could crack the plastic base unit.

Step 5

Prepare the reservoir for install. Locate all of the needed pieces for the plastic reservoir. Assemble dry to ensure proper placement of each piece. With the base unit in the upright position, one barb should face into the unit, while the other should face toward the banana jacks. Use the weld-on glue and be sure to follow proper adhesion techniques to glue each reservoir piece together. Allow the glue to set for approx. 10 minutes. Install both of the brass barbs into their respective slots by following the instructions laid out in Step 4. Now, attach a piece of tubing to the barb located inside the base unit, and
cut to length. Attach the other end of the tube to the barb on the reservoir. Position the reservoir against the base unit using the spacers, glue in place.

Section 3: Gear Mount and Pinion Shaft

Step 1

Locate the 10 mm bearings and the bearing block plastic pieces. Press the bearings into the plastic using a suitable method. The plastic will be tight, because this is a press fit. NOTE: The gear may not press flush with both sides of the plastic block.

Step 2

Locate the pinion gear and the pinion shaft. Position the pinion gear so that the tension pin holes are aligned with the shaft. Now, press a 1/8 inch diameter 1 inch length tension pin through both the gear and the shaft. NOTE: The pin may protrude from the gear; this will not cause any interference.

Step 3

Slide the pinion shaft assembly through the bearings. Make sure that the flush sides of the bearings are both facing the middle of the shaft. Then attach the e-clips into their grooves. Set the pinion bearing assembly aside for now.

Step 4

Locate the 8-pin op amp socket, which will be used as the sensor connector. Remove the four middle pins of the op amp socket. Next, use a small drop of super glue to adhere the sensor plug to the back of the op amp socket. Make sure and center the plug on the socket.

Step 5

Solder one wire that is approx. 1 ft in length to each of the four pins. Be sure and mark each wire with a number one through 4 starting with the pin that is located above the notch on the socket, then move counter clockwise. A small piece of masking tape works well to number the wires.

Step 6

Insert the sensor wire socket into the upper post plastic piece. Align the sensor socket so that the pin above the notch is closest to the post wire slot. Set aside for now.

Step 7
Locate the lower post plastic piece, and press in the 0.125" dowel pins in their slots. The dowel pins do not need to be pressed in all the way, just enough to ensure that they will stay aligned. Next, install an m4 x 0.7 x 25mm machine screw into the slot provided. Use a drop of blue thread locker on the threads then tighten the m4 nut so that it is snug. Now, connect the upper post assembly from step 6 to the lower post using m4 x 0.7 button head screws. Make sure to align the slot for the wires in both the upper and lower pieces. NOTE: The plastic pieces of the center post may need to be sanded smooth using a very fine sandpaper (1500 grit) to ensure proper alignment. The center post assembly is now ready. Set aside for now.

Step 8
Locate the bevel gear and the bronze bushing. Insert the bronze bushing onto the bevel gear so that the flange is against the flat side of the gear. Now, install the center aluminum plug into the gear align the holes and press in a 1/8 inch diameter by 1.5 inch length tension pin through the gear and the aluminum plug. Make sure that the pin protrudes evenly on both sides of the gear. Verify that the gear is able to spin freely in the bushing.

Step 9
Press the bronze bushing assembly into the gear mount block, by using a vice or other appropriate method. Now, install the center post assembly from step 7 onto the gear mount assembly, by threading the m4 x 0.7 screw into the center of the aluminum plug. This completes the assembly of the center post drive mechanism.

Section 4: Disk and Springs

Step 1
Locate the disk center plastic piece, and install the size 1 split rings into the three outer holes. Next, install the LED into the center hole. Make sure that it is straight and flush with the surface.

Step 2
Cut off two 5 inch lengths of the 0.003" diameter enamel wire from the relay spool. Insert one end into the electrical terminal, and pull through about I inch of wire. Wrap the wire around the terminal several times to take up this slack. Crimp the wire terminal, then solder to make a good connection. Verify the connection using an ohm meter. Install a small ¼ inch piece of black shrink wrap to the connection. Repeat this process for the second piece of wire, only use red shrink wrap instead of black.

Step 3
Take the black shrink wrap terminal, and carefully solder the free end onto the back of the LED while it is in the plastic center piece. This will keep the LED in place. Now, take the red shrink wrap terminal, and solder it to one of the tabs on the front of the LED. Be extra careful not to get solder on the dome of the LED or to heat it up too much while soldering. Verify all connections using an ohm meter.

Step 4

Locate the size 1 ball bearing swivels, and clip off the welded rings that are on the stationary side. Next, install a size 1 split ring in their place. Now, carefully install one end of the spring onto each split ring. Once this process has been completed for all three springs, install the other end of each spring onto the split ring that is found on the center disk.

Step 5

Install the complete spring assembly from step 4 onto the foam disk, by applying a small bead of hold the foam adhesive to the center of the disk. Then, place the spring assembly into position with the dome of the LED facing out. Make sure that the enamel wires exit the disk along the spring channel that is in line with the notch. The red should be on the upper and the black on the lower as you look down on the underside of the disk. Finally apply a small amount of the adhesive to the LED wires to keep them rigidly attached to the disk. The disk and spring assembly is now ready for overall assembly

Section 5: Overall Assembly

Step 1

Install the center post mechanism, by applying a light coat of silicone spray to the outside of the post. Also, be sure and apply the silicone spray to the inside of the base unit where the post will raise and lower.

Step 2

Slide in the center post from the back of the base unit. Make sure to properly align the post before inserting. The flat spot on the sensor slot should be between the two cut off corners as seen from the top of the base unit. Once the center post is inserted, align the gear mount dowel pins with the holes on the base unit. Install and tighten the m8 x 1.25 screws until snug. NOTE: Watch out for the sensor wires during install, they should exit the center post on the side away from the reservoir.

Step 3

Install the pinion shaft assembly onto the back of the base unit using m6 x 1.0 button head cap screws. It is easiest to insert the free end of the shaft through the access hole first, and then position the bearing blocks in place.

Step 4

Locate the electrical female DB9 connector. Run the sensor wires through the slot for the connector, and then solder each wire in the appropriate terminal. Next, attach the DB9 connector using the m2.5 screws.

Step 5

Install the PSD sensor in the top of the base unit. Make sure and align the sensor correctly using the flat spot as a guide. Once the sensor is installed, lower the center post so that the sensor is not damaged during disk installation.

Step 6

Install the disk and spring assembly, by attaching the terminal wires red to red and black to black on the banana jacks. Next, loop each swivel ring onto the corresponding adjustment screw eyelet.

Step 7

Install the foam lid if desired. The unit is now ready for use.

APPENDIX E

PARTS LIST

Parts List

Qty	description	Part number	Source	Contact Name	email or website	phone	Cost each	Total
1	Styrofoam disk		Foamlinx	Tal Bernea	foamlinx.com		$145.00	$145.00
1	Styrofoam Lid		Foamlinx	Tal Bernea	foamlinx.com		$145.00	$145.00
3	Ultra fine adjustment screws	9SH127BM-25	Altos Photonics	Emily Bates	emily@altosphotonics.com	406-570-7472	$41.00	$123.00
3	Micro Springs k = 0.335 N/m custom	AE 00480-438-MW-1.90	Axcess Spring	Ashley Hughes	ashley@axcesspring.com	951-276-2777	$27.78	$83.33
1	2-D PSD 4 x 4 mm active area	2L4SP	On-Trak	Dave Hunnicut	www.on-trak.com	949-587-0769	$370.00	$370.00
1	Sensor amplifier for 2-D PSD	OT-301DL	On-Trak	Dave Hunnicut	www.on-trak.com	949-587-0769	$795.00	$795.00
1	Vertical cavity in pill LED		Hamamatsu				$30.00	$30.00
2	Bearing 10mm ID	A 7C55MP3010	SDP-SI	online	www.sdp-si.com		$4.55	$9.10
1	Bevel gear	A 1M 3MYZ2030B	SDP-SI	online	www.sdp-si.com		$5.88	$5.88
1	Pinion gear	A 1M 3MYZ2015	SDP-SI	online	www.sdp-si.com		$2.99	$2.99
1	Delrin 3/4 in round stock 12 in length		Laird Plastics	Local		801-972-5911	$3.00	$3.00
1	Aluminum round stock 10 mm Dia 12 in long	Special Order	Metal supermarket	Local		801-972-5911	$35.00	$35.00
1	Aluminum round stock 1 in Dia 12 in long		Metal supermarket	Local		801-972-5911	$10.00	$10.00
3	Size 1 swivels		Fish Tech	Local		801-272-8808	$1.00	$3.00
6	Size 1 split rings		Fish Tech	Local		801-272-8809	$0.10	$0.60
3	2-56 Threaded Eyebolt	sullivan is the brand	Amazon	online	www.amazon.com		$2.00	$6.00
3	1/8 NPT to male hose barb		Evco	Local			$1.00	$3.00
1	1/8 inch clear vinyl tubing 12 in length		Evco	Local			$2.00	$2.00
1	1/8 inch NPT brass plug		Evco	Local			$1.00	$1.00
1	30 mm ID bronze bushing		Motion Industries	Local			$35.00	$35.00
1	red banana jack plug		U of U ECE stockroom	Local			$1.50	$1.50
1	black banana jack plug		U of U ECE stockroom	Local			$1.50	$1.50
1	Female DB9 connector		U of U ECE stockroom	Local			$3.00	$3.00
1	8 pin op-amp socket		U of U ECE stockroom	Local			$0.50	$0.50
1	26 guage stranded wire 10 ft		U of U ECE stockroom	Local			$2.00	$2.00
2	terminal connector for banna plugs		U of U ECE stockroom	Local			$0.50	$1.00
1	1 amp micro relay		U of U ECE stockroom	Local			$5.00	$5.00
1	11 oz. can Sprayway 945 silicone spray		Regional Supply	Local			$15.00	$15.00
1	pint weld-on glue for acrylic		Regional Supply	Local			$15.00	$15.00
1	Hypo for applying glue		Regional Supply	Local			$7.00	$7.00
1	4 oz. bottle Hold the foam	Beacon	Hobby Lobby	Local			$5.00	$5.00
1	Plastic base housing		Plastic Fabricating	Local			$750.00	$750.00
1	Plastic Post upper		Plastic Fabricating	Local				
1	Plastic post lower		Plastic Fabricating	Local				
1	Plastic gear mont block		Plastic Fabricating	Local				
2	Plastic bearing blocks		Plastic Fabricating	Local				
2	Plastic resevoir sides 1/8 NPT tapped		Plastic Fabricating	Local				
2	Plastic resevoir sides no holes		Plastic Fabricating	Local				
1	Plastic resevoir base		Plastic Fabricating	Local		**Grand Total**		$2,614.40

Hardware and Supplies

Qty	description	Source	Contact Name	email or website	phone	Cost each	Total
1	Hex bolt m4 x 0.7 x 25 mm length	Bolt Center	Local		801-486-0088	$10.00	$10.00
4	Button head cap m6 x 1.0 x 10 mm length	Bolt Center	Local				$0.00
2	Button head cap m4 x 0.7 x 15 mm length	Bolt Center	Local				$0.00
1	Hex nut m4 x 0.7	Bolt Center	Local				$0.00
2	Pan head m2.5 x 0.45 x 15 mm	Bolt Center	Local				$0.00
2	Hex nuts m2.5 x 0.45	Bolt Center	Local				$0.00
2	Socket head cap m8 x 1.25 x 35 mm length	Bolt Center	Local				$0.00
2	E-clips for 10 mm shaft	Bolt Center	Local				$0.00
4	dowel pins 1/8 in Dia x 0.25 in length	Bolt Center	Local				$0.00
1	Tension Pin 1/8 in Dia 1 1/2 in length	Bolt Center	Local				$0.00
1	Tension Pin 1/8 in Dia 1 in length	Bolt Center	Local				$0.00
1	Sheet 1500 grit sandpaper	Hardware	Local			3	$3.00
1	Tube super glue	Hardware	Local			3	$3.00
1	Roll PTFE thread seal tape	Hardware	Local			2	$2.00
1	2.5 ml bottle blue threadlocker	Hardware	Local			5	$5.00
1	solder for electrical	Electrical	Local			1	$1.00
					Total		$24.00

REFERENCES

Allen, J. M. 1977 Experimental study of error sources in skin friction balance measurements. *Journal of Fluids Engineering* **99**, 197–204.

Bradley, E. F. 1968 A micrometeorological study of velocity profiles and surface drag in the region modified by a change in surface rougness. *Quarterly Journal of the Royal Meteorological Society* **94**, 361–379.

Clauser, F. H. 1954 Turbulent boundary layers in adverse pressure gradients. *Journal of the Aeronautical Sciences* **21**, 91–105.

Drazin, P. & Riley, N. 2006 The navier-stokes equations: A classification of flows and exact solutions. In *London Mathematical Society Lecture Note Series 334* (ed. N. J. Hitchin), pp. 90–91. Cambridge University Press.

Fernholz, H. H., Janke, G., Schober, M., Wagner, P. M. & Warnack, D. 1996 New developments and applications of skin-friction measuring techniques. *Measurement Science Technology* **7**, 1396–1409.

Haritonidis, J. H. 1989 The measurement of wall shear stress. In *Lecture in Engineering, Advances in Fluid Mechics Measurements* (ed. M. Gad-el-Hak), pp. 229–261. Berlin and New York, Springer-Verlag.

Haugen, D. A., Kaimal, J. C. & Bradley, E. F. 1971 An experimental study of reynolds stress and heat flux in the atmospheric surface layer. *Quarterly Journal of the Royal Meteorological Society* **97**, 168–180.

Hecht, E. 1987 *Optics*, 3rd edn. Reading, Massachusetts: Addison-Wesley Publishing Comapny.

Heuer, W. D. C. & Marusic, I. 2005 Turbulence wall shear stress sensor for the atmospheric surface layer. *Measurement Science Technology* **16**, 1644–1649.

Hinze, J. O. 1975 *Turbulence*, 2nd edn. New York: McGraw-Hill.

Ingard, K. & Akay, A. 1987 On the vibration damping of a plate by means of a viscous fluid layer. *Journal of Vibration, Acoustics, Stress, and Reliability in Design* **109**, 178–184.

Inman, D. J. 2008 *Engineering Vibration*, 3rd edn. Upper Sadle River, New Jersey: Pearson Prentice Hall.

Klewicki, J. C., Metzger, M. M., Klener, E. & Thurlow, E. M. 1995 Viscous sublayer flow visualization at $Re_\theta = 1500000$. *Physics of Fluids* **7**, 857–861.

Kundu, P. K. & Cohen, I. M. 2008 *Fluid Mechanics*, 4th edn. Burlington, MA: Elsevier Academic Press Inc.

Magill, S. A. 1999 Study of direct measuring skin friction gage with rubber compounds for damping. Master's thesis, Virginia Polythechnic Institute and State University, Blacksburg, VA.

Marusic, I., Kunkel, G. & Porte-Agel, F. 2001 Experimental study of wall boundary conditions for large eddy simulations. *Journal of Fluid Mechanics* **446**, 309–320.

Metzger, M. 2002 Scalar dispersion in high Reynolds number turbulent boundary layers. PhD thesis, University of Utah, Salt Lake City, Utah.

Metzger, M. 2006 Length and time scales of the near-surface axial velocity in a high reynolds number turbulent boundary layer. *International Journal of Heat and Fluid Flow* **27**, 534–541.

Modest, M. F. 2003 *Radiative Heat Transfer*, 2nd edn. San Diego, California: Academic Press.

Morsy, M. 1974 An instrument for the direct measurement of local wall shear stress. *Journal of Physics E: Scientific Instrumentation* **7**, 83–86.

Nitsche, W., Haberland, C. & Thuenker, R. 1984 Comparitive investigation on friction drag measuring techniques in experimental aerodynamics. In *ICAS-84-2.4.1, 14th ICAS Congress*, pp. 391–403.

Paros, J. M. 1970 Application of the force-balance principle to pressure and skin friction sensors. *16th Annual Technical Meeting, Proc. Inst. Environmental Sciences* pp. 363–368.

Piomelli, U. & Balaras, E. 2002 Wall-layer models for large eddy simulations. *Annual Review of Fluid Mechanics* **34**, 349–374.

Pradeep, A. M. & Sullery, R. K. 2003 A displacement based wall shear stress sensor. *IE (I) Journal* **84**, 27–31.

Ruede, J. D., Nagib, J. O. & Monkewitz, P. A. 2002 Evaluation of three techniques for wall-shear measurements in three dimensional flows. *Experiments in Fluids* **35**, 389–396.

Sadr, R. & Klewicki, J. C. 2000 Surface shear stress measurement system for boundary layer flow over a salt playa. *Measurement Science Technology* **11**, 1403–1413.

Smith, T. B. 2001 Development and ground testing of direct measurement skin friction gages for high enthalpy supersonic flight. PhD thesis, Virginia Polythechnic Institute and State University, Blacksburg, VA.

Winter, K. G. 1977 An outline of the techniques available for the measurement of skin friction in turbulent boundary layers. *Progress in Aerospace Science* **18**, 1–57.